Master Thesis, Department of Geosciences

The Vp/Vs relationship of the basement under the Trøndelag Platform, mid-Norway

By

Muhammad Assad

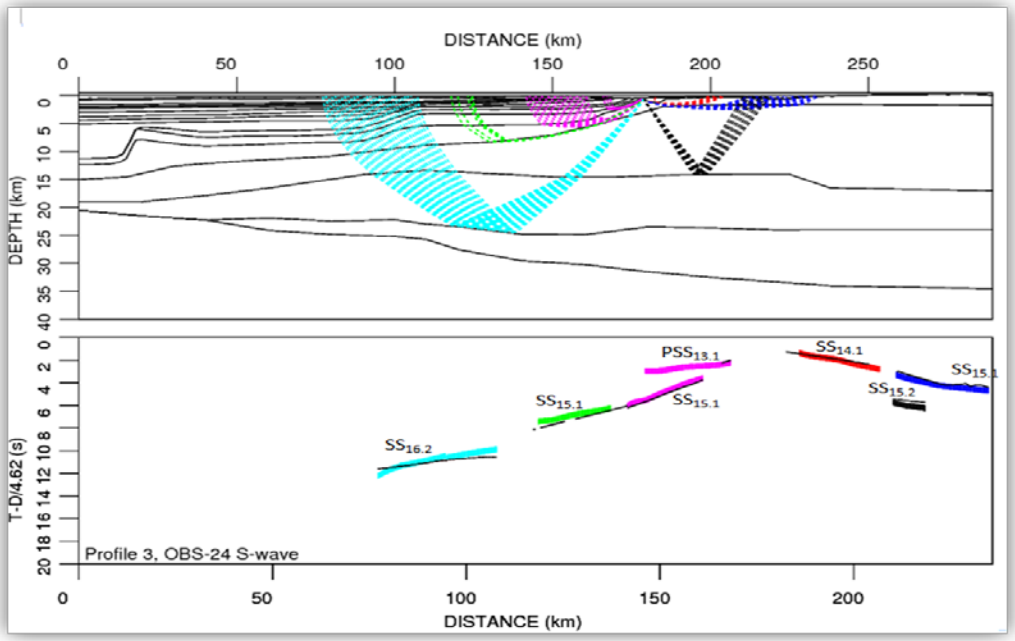

UNIVERSITY OF OSLO

FACULTY OF MATHEMATICS AND NATURAL SCIENCES

The Vp/Vs relationship of the basement under the Trøndelag Platform, mid-Norway

By

Muhammad Assad

Master Thesis in Geosciences

Discipline: Geophysics

Department of Geosciences

Faculty of Mathematics and Natural Sciences

University of Oslo

(June 2013)

Tutors(s): Asbjørn Breivik, Jan Inge Faleide and Abhishek Kumar Rai

This work is published digitally through DUO – Digitale Utgivelser ved UiO

http://www.duo.uio.no

It is also catalogued in BIBSYS (http://www.bibsys.no/english)

Acknowledgement

I would like to express my gratitude to my supervisors Asbjørn Breivik (UiO), Jan Inge Faleide (UiO) and Abhishek Kumar Rai (UiO) for their support and encouragement throughout my thesis work. I am very grateful to them for their advices and feedbacks on my work.

I also thankful to University of Oslo and Bergen University for providing me the data and resources necessary to carry on this work.

Finally, my special thanks to my family for their support and patience, not only during this work, but also during the last years.

TABLE OF CONTENTS Page No

Abstract

Two wide angle 3-Compnent Ocean Bottom Seismometer (OBS) profiles along with associated Land-Stations acquired during 2003 under the EUROMARGINS Program were analyzed during this M.Sc. Thesis. These profiles are named as PROFILE -3-03 & 4-03 & were aimed at studying the crustal structure beneath the Trøndelag Platform & adjacent areas, mid-Norway. Shear waves recorded on the horizontal components of the seismometers have been modeled using 2-D kinematic ray-tracing software RAYINVR, utilizing already generated p-wave velocity models. For shallower sediments (1-6 km depths) average Vp/Vs ratios are relatively high as expected i.e. 2.0-2.6 which indicate the presence of low consolidated sediments in the upper layers. The deeper sedimentary layers (6-11 km depth) present along NW side of both profiles exhibit lower Vp/Vs ratios i.e. 1.8-2.0 which represent further compacted sediments because of increased burial. The upper crust has an average Vp/Vs ratio in the range 1.75-1.78 which suggests that the crust under the Trøndelag Platform is felsic. Vp/Vs ratio increases to 1.80-1.85 in the lower crust which suggests the presence of mafic to ultra-mafic lower crust.

1) Introduction

The sedimentary cover underneath Trøndelag Platform and Halten Terrace is well-known because of detailed coverage of commercial seismic reflection surveys and subsequent well data carried out for HC exploration. However, less information is available about the deeper structures in this area. Therefore, in order to map deeper crust two Ocean Bottom Seismic (OBS) profiles (Profile 3-03 and Profile 4-03) were acquired in 2003 by Håkon Mosby under the Euro Margins Program. These included OBS stations and associated land stations. The study area is shown in figure 1.1 (Breivik et al, 2011).

Profile 3-03 has data from twelve OBS's (ocean bottom seismometers) and five land stations and has a length of 285 km continuing in the NW-SE direction. Whereas Profile 4-03 extends up to 356 km's and includes data from eleven OBS's and six land stations, having nearly the same orientation as Profile 3-03. Expect few OBH stations (Ocean Bottom Hydrophones), which record seismic signal in vertical direction only, all the other instruments were capable of recording seismic signal in vertical and two horizontal directions as well.

The p-wave velocity modeling has already been carried out using the vertical component of 3-C Geophones and wide angle OBS Stations data for both profiles. P-wave modeling shows continental crust deep under both the profiles. It reveals that basement is composed of distinctive velocity layers and its thickness increases from NW to SE as shown in figure 1.2 and 1.3 (Breivik et al, 2011).

The purpose of this thesis is to obtain the s-wave velocity values for different parts of the already generated p-wave models using the information from arrivals at the horizontal components of the OBS and Land Stations. It will enable mapping of Vp/Vs ratios along the profiles. The Vp/Vs ratios will be used to discuss velocity differences i.e. possible lithology indications and basement rock composition for the different parts of the models.

In order to achieve the above objective first the wide angle OBS data will be processed using Seismic Unix software. It will be followed by interpretation of different s-wave arrivals on horizontal components of OBS's on both profiles. Third step will be the modeling of s-wave arrivals using RAYINVR software. It will be carried out using already generated p-wave velocity models as basis for s-wave velocity modeling.

Finally, the modeling results will provide ratios for p and s-wave velocities i.e. Vp/Vs ratios for different parts of the p-wave velocity models which will be discussed in the last section.

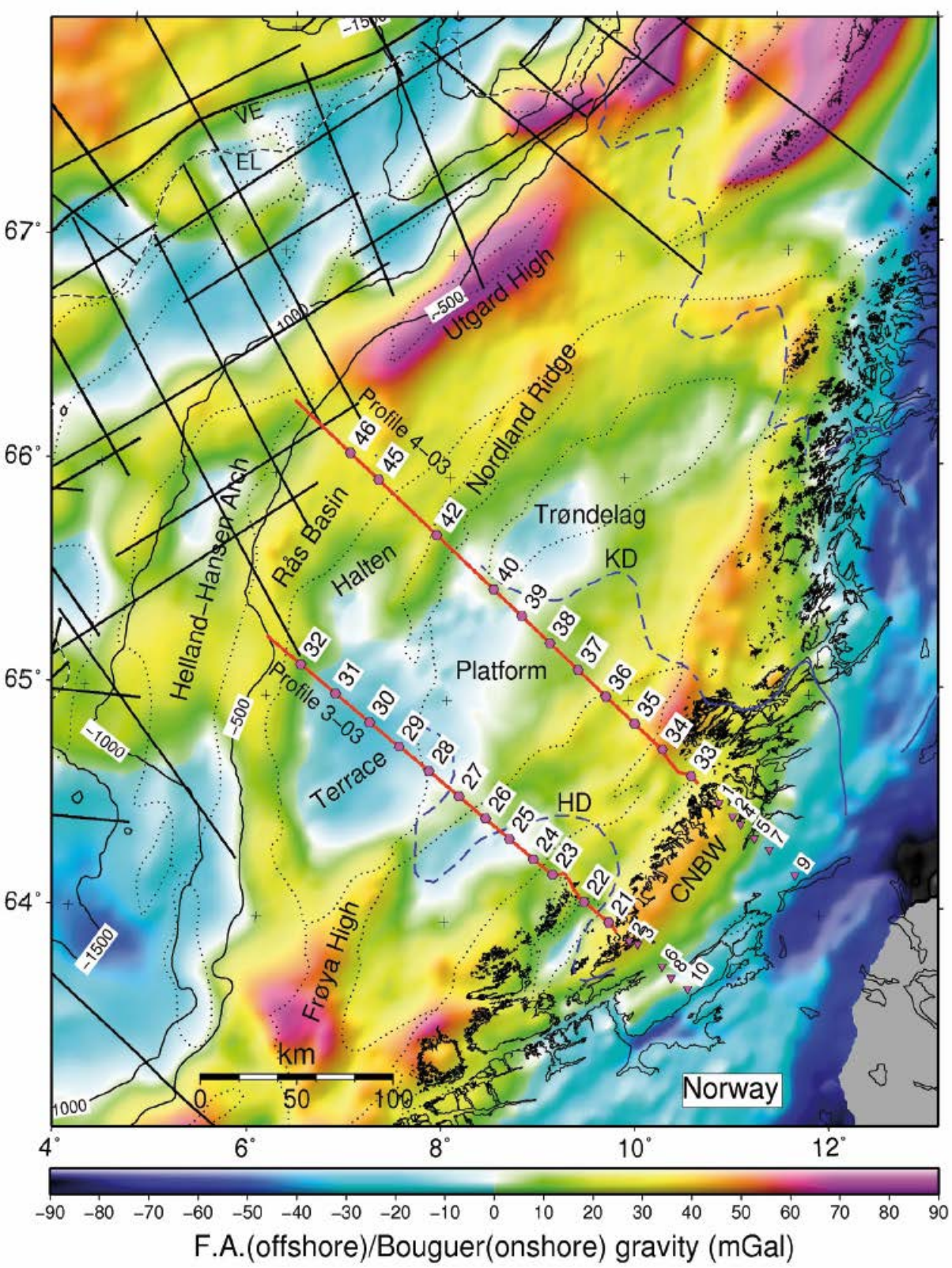

Figure 1.1*; Gravity map showing the position of Profile 3-03 and Profile 4-03 (Breivik et al, 2011).*

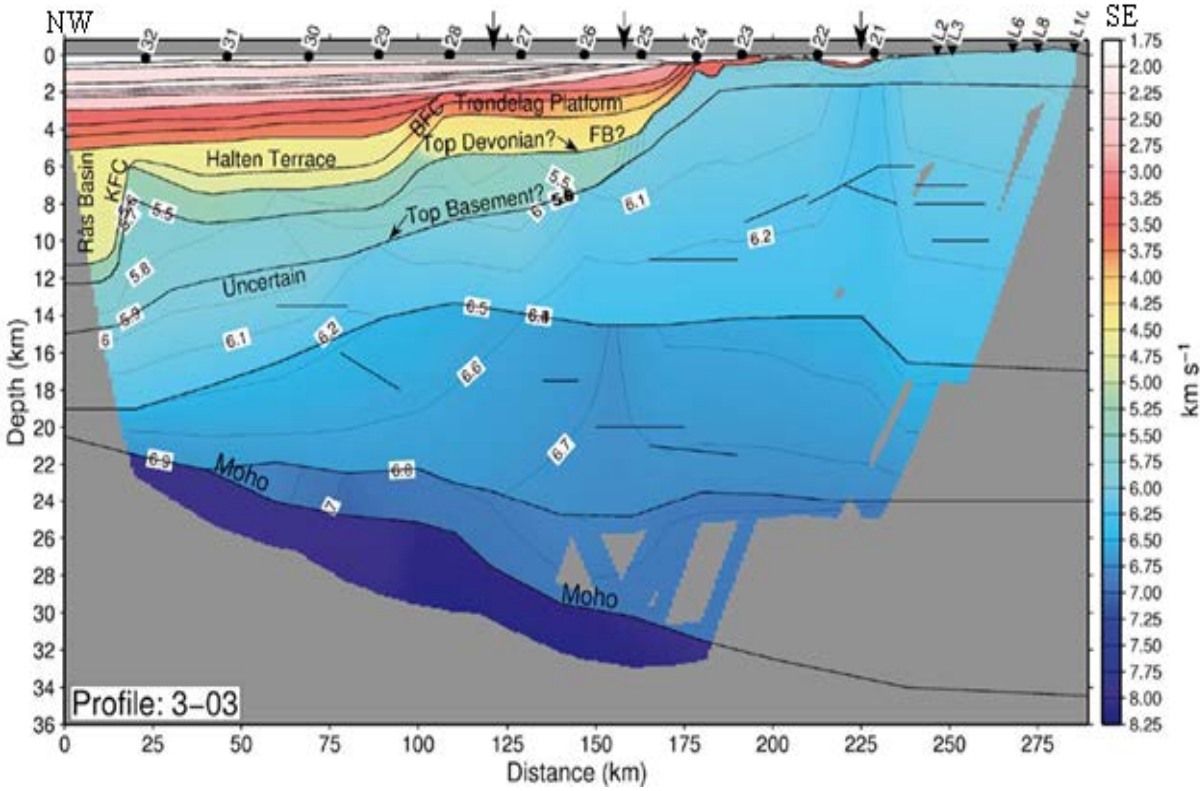

Figure 1.2*; Crustal p-wave velocity model along Profile 3-03. BFC: Bremstein Fault Complex, FB: Froan Basin, KFC: Klakk Fault Complex. (Figure modified from (Breivik et al, 2011).*

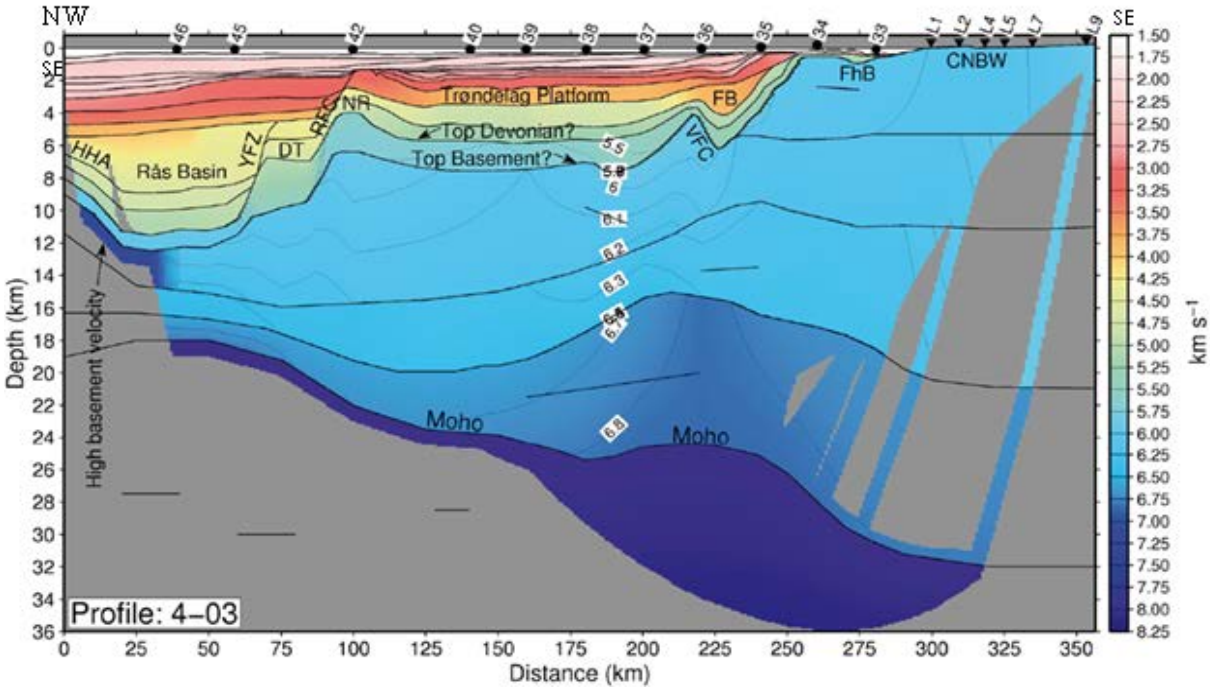

Figure 1.3*; Crustal p-wave velocity model along Profile 4-03. CNBW: Central Norway BasementWindow, DT: Dønna Terrace, FB: Froan Basin, FhB: Frohavet Basin, HHA: Helland-Hansen Arch, RFC: Revfallet Fault Complex,VFC: Vingleia Fault Complex, YFZ: Ytreholmen Fault Zone. (Figure modified from Breivik et al, 2011).*

2.1) Development of Mid-Norway Continental Margin

Mid-Norway continental margin evolved differently as compared to other Passive continental margins as it experienced prolonged rifting episode and significant tectonic activity continued even after crustal separation (Bukovics and Ziegler, 1984, Smelror et al., 2007).

2.1.1) Basinal Development during Palaeozoic;

Caledonian Orogeny was a result of collision between Greenland-Laurentian Plate and Fennoscandian-Russian Plate in Ordovician to Early Devonian Times. From Early Devonian onwards the Caledonides formed during Caledonian Orogeny started to collapse due to the diminishing thrusting activity (Andersen et al, 1991; Milnes et al. 1997; Fossen, 2000; Terry et al. 2000).

Regional crustal extension dominated the evolution of Norwegian-Greenland Sea from Late Carboniferous onwards. Development of rift system resulted in accumulation of Permian carbonates and clastics into the large half-grabens (Haller, 1971). Similarly, a rapid subsidence of the eastern part of Trøndelag Platform was observed during the Late Paleozoic (Blystad et al., 1995, Bukovics and Ziegler, 1984, Smelror et al., 2007).

This extension activity continued until Late Permian times. It resulted in the transgression of Arctic Permian seas into the Northern and Southern Permian basins of the Northwest Europe. This transgression was facilitated by Norwegian-Greenland Sea Rift system (Smelror et al., 2007, Ziegler, 1982).

2.1.2) First rifting stage in Early Mesozoic;

Crustal extension in Norwegian-Greenland sea area paced up during the Early Triassic times. Rifting continued to extend southward to the North Sea area (Ziegler, 1982). Triassic strata deposited on Trøndelag Platform show the evidence of subsidence and rifting as it has developed syn-depositional tensional faulting (Blystad et al., 1995, Bukovics and Ziegler, 1984, Smelror et al., 2007).

Almost entire Mid-Norway shelf was affected by the Triassic-Jurassic rifting stages (Phase 1 as shown in Figure 2.1). Trøndelag Platform is more intensely faulted on the western side than the eastern one. Fault rotation and their geometries suggest that mechanical stretching and associated thinning are the most obvious cause of subsidence of Norwegian-Greenland Sea

during the Late Paleozoic to Mid-Mesozoic times. (McKenzie, 1978; Figure 2.2 (A), Bukovics and Ziegler, 1984, Brekke, 2000, Smelror et al., 2007).

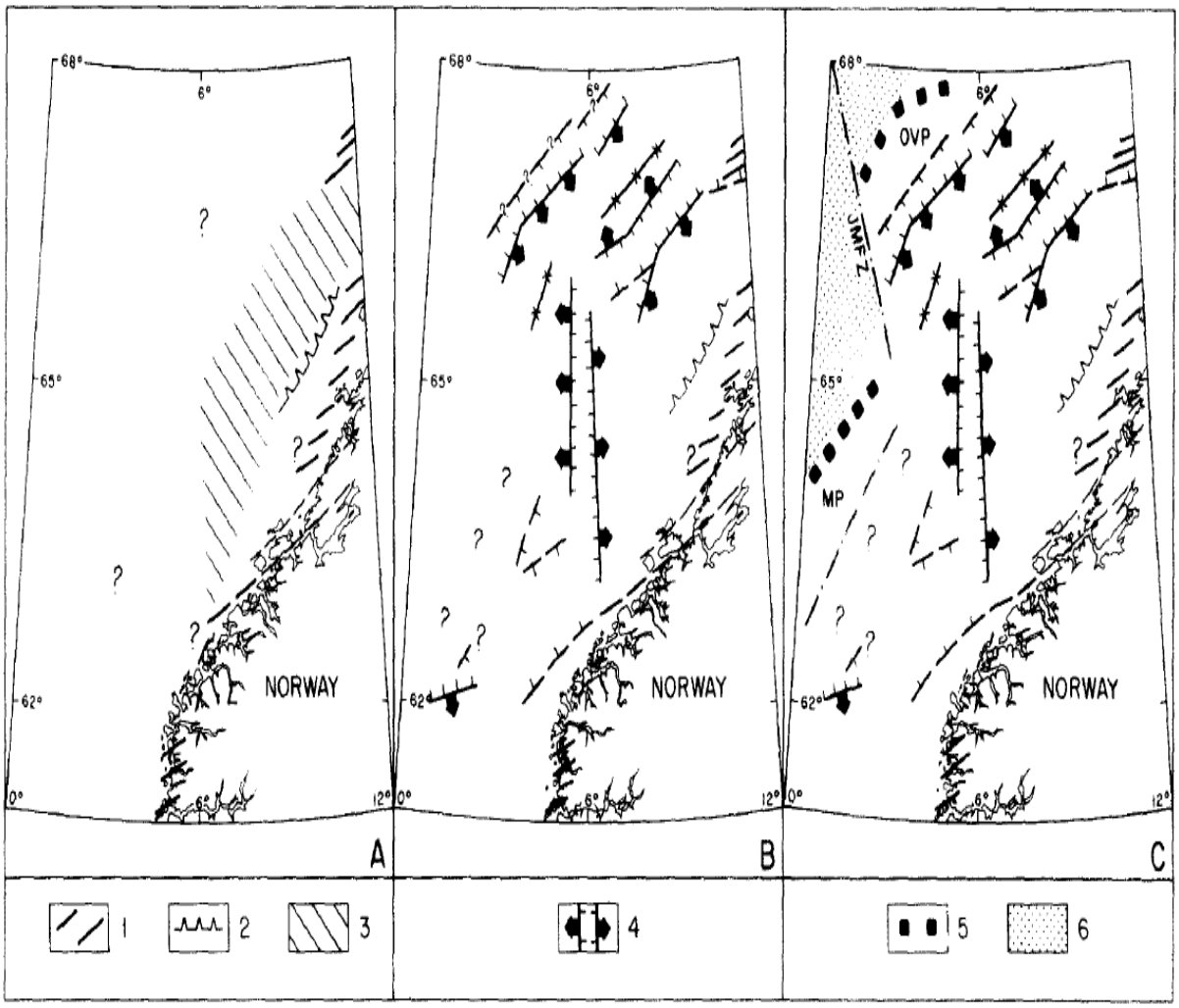

Figure 2. 1 *'Contraction of area as a result of tectonic activity: 1. Devonian and Carboniferous subsidence. (A) First rifting stage, Carboniferous to Jurassic subsidence. 2, Eastern flank of Permo-Triassic basin; 3, Effected region as a result of Triassic and Jurassifaulting. (B) Second rifting stage, Upper Jurassic/Lower Cretaceous rifting. 4, Major Upper Jurassic-Lower Cretaceous graben systems. (C) Third rifting stage. 5, Approximate continent-ocean transition; 6, Ocean crust; MP, Møre Platform; OVP, Outer Vøring Plateau; JFMZ, Jan Mayen Fracture Zone' (Bukovics and Ziegler, 1984).*

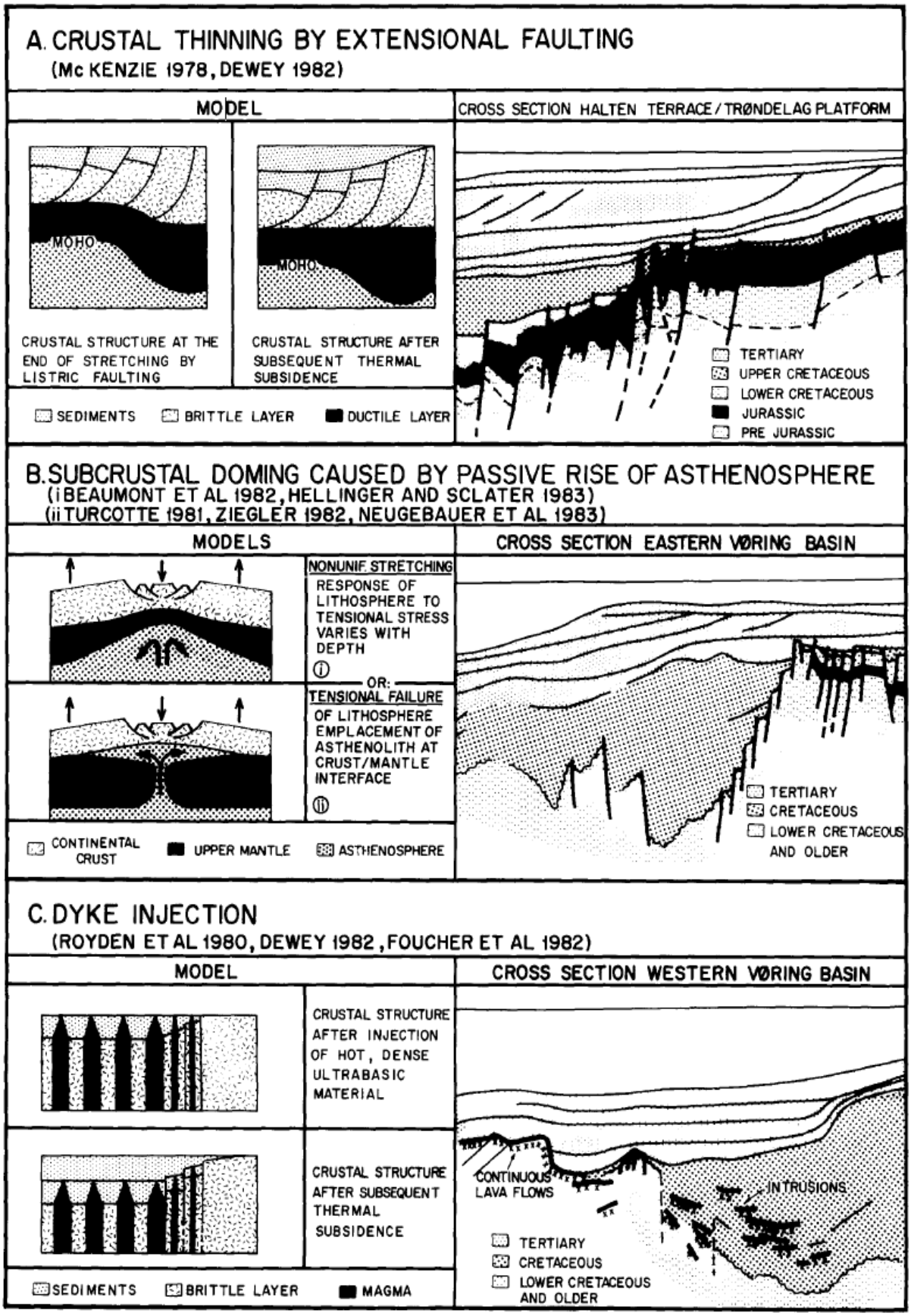

Figure 2.2; *Theoretical crustal subsidence models vs data from Mid-Norway are. Vertical exaggeration is 15:1(Bukovics and Ziegler, 1984).*

2.1.3) Second rifting stage in Late Mesozoic;

It affected the Mid-Norway area strongly. A rapid subsidence was observed in Møre and Vøring Basins whereas flanks of the rift system have been uplifted at the same time. Rapid subsidence and uplift from the flanks could be result of thinning and extension of lithosphere. However, Trøndelag Platform was not much affected by this episode (Late Jurassic and Early Cretaceous) and it caused only little subsidence during the Cretaceous (Bukovics and Ziegler, 1984, Brekke, 2000, Smelror et al., 2007).

Phase two, in Figure 2.1 suggest that from now on-ward most of the rifting activity is focused around axial parts of the East Greenland--Mid-Norway rift area. Several theories can explain the uplift of flanks of the rift system as a result of continued stretching and subsidence as shown in Figure 2.2 (B). The different hypothesis presented in figure 2.2 represents a possible explanation of uplift of the flanks of the rift system. However, lithospheric extension is the principle cause for the all of the above phenomena (Bott, 1981, Bukovics and Ziegler, 1984).

Therefore, during the Cretaceous Times Mid-Norway area evolved as a result of high rate of graben subsidence due to stretching of the crust whereas rifting continued until Late Cretaceous (Bukovics and Ziegler, 1984, Müller et al. 2005, Underhill, 1998, Gabrielsen et al., 2001, Smelror et al., 2007).

2.1.4) Crustal Separation in Palaeogene;

Paleocene was marked by an increased rifting activity between Fennoscandian cratons and Greenland. These areas represented future break-up axis. This new episode of rifting was fuelled and was accompanied by the Paleocene-Early Eocene volcanic upward movement. In Norwegian-Greenland Sea the Early Eocene represents the time when crustal separation was achieved. The frequency of dykes and sills increases to the westward direction. Most of them are present in Jurassic to Eocene sedimentary strata (Smelror et al., 2007, Bukovics and Ziegler, 1984).

Such high amount of volcanic intrusions can be explained by Foucher et al, (1982) model as shown in figure 2.2 (C). This model suggests that during the last stages of rifting activity crust extends as a result of rifting. When it exceeds to a factor of 3 compared to original un-extended levels, massive amount of dyke activity becomes the principle reason for the start of crustal separation (Bukovics and Ziegler, 1984, Smelror et al., 2007).

2.1.5) Sea-floor spreading in Oligocene;

Crustal separation had been achieved before Oligocene. After this the primary agents for crustal subsidence were lithospheric cooling which was assisted by water and sediments loading. During Oligocene rearrangement of sea-floor spreading axis took place along Norwegian-Greenland Sea. The transform fault movement along Jan Mayen Fracture Zone also occurred at the same time. The relative movement of the spreading axis and along Jan Mayen Fault Zone resulted in local compression events as well. High rates of subsidence due to cooling resulted in higher paleo-water depths. However, ice-unloading during the Pleistocene resulted in erosion of the mainland areas/basin margins (Bukovics and Ziegler, 1984, Smelror et al., 2007).

2.2) Structural and tectonic elements of Norwegian Continental Margin

NE-SW trending Cretaceous basins bounded by paleo-highs and platforms are the main constituents of the present day Norwegian continental margin between 62^{o} and 69^{o}N as shown in Figure 2.3. Møre and Vøring Marginal Highs represent the western boundaries of the continental margin. Faroe-Shetland escarpment represents the boundary between marginal highs and basin area to the south while Vøring Escarpment distinguishes between them to the north (Brekke, 2000).

Trøndelag Platform flanks the continental margin from the central east side while eroded mainland marks the boundaries north and south of Trøndelag Platform to the east. Northern boundary of the main deep Basin area is characterized by NW-SE trending Bivrost Lineament (Brekke, 2000).

Although the main structural grain of Norwegian Continental Margin has NE-SW orientation, two NW-SE trending lineaments (Bivrost and Jan Mayen Fracture Lineaments) divide it into three structural areas i.e. northern, middle and southern provinces (Brekke, 2000).

Below are the main structural and tectonic components of the Norwegian Continental Margin discussed in detail (Brekke, 2000).

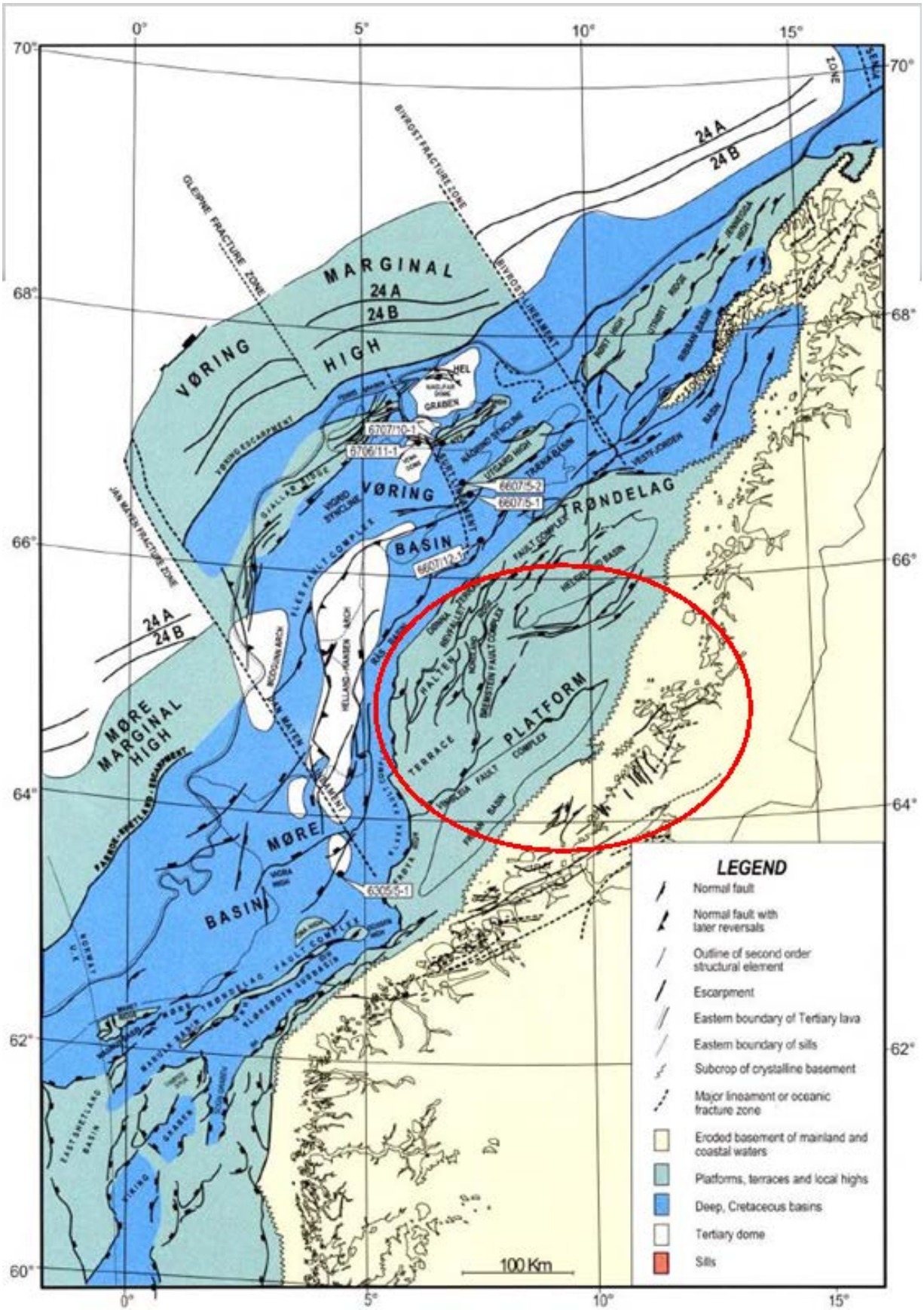

Figure: 2.3 *Structural map of the Norwegian Continental Margin. Study area across Trøndelag Platform and Halten Terrace is shown in red circle (Brekke, 2001).*

2.2.1) Jan Mayen Lineament

It represents the boundary between the Møre Basin to the south and the Vøring Basin to the north. It can be distinguished by counter clockwise shift of basinal flanks and axes. It also marks the boundary of the Trøndelag Platform to the south (Brekke, 2000).

2.2.2) Bivrost Lineament

It distinguishes the Vøring Basin from the uplifted continental margin around Loften to the north. It matches with the Trøndelag Platform termination to the north. It can also be distinguished as a clock wise shift in basinal axes and associated flanked portions (Blystad et al, 1995; Brekke, 2000).

2.2.3) Vøring Basin

It encompasses areas between 64-68°N and 2-10°E and is a large basin having grabens, sub-basins and structural highs as salient features. The distinguishing feature of Vøring Basin is the enormous thickness of Cretaceous sequence. In some parts, the cretaceous base is as much as 9s twt (two way travel time) deep in the seismic section (Bukovics and Ziegler, 1985; Blystad et al, 1995).

Vøring Basin is bordered by the Vøring Escarpment from the west and is bounded by fault complexes around the corners of Trøndelag Platform in the eastward direction. Fles Fault Complex bisects the basin and runs parallel to basin axes from Jan Mayen Lineament to Bivrost Lineament. It also has Paleocene mafic intrusions as sills. Most of the sills are present in the western part and seismic reflections coming from underlying strata below the sills are blurred. Magmatic activity was the result of continental breakup (Bukovics et al, 1984; Blystad et al, 1995; Brekke, 2000, Eldholm and Coffin, 2000; Eldholm and Grue, 1994).

Helland Hansen Arch is the most prominent structural high in the Vøring Basin present in central southern part. It was formed as a result of compressional tectonics in the Cenozoic era by the reverse reactivations of the Fles Fault Complex. Surt Lineament which also includes the Rym Fault Zones separates the northern part of the basin (Brekke, 2000).

2.2.4) Vøring Marginal High and Møre Basin

It is situated between Jan Mayen and Bivrost Lineaments and to the west of Vøring Escarpment. It is composed of Tertiary deposits overlying the continental crust. The

continental crust gets thinner and changes to oceanic crust in the westward direction (Blystad et al., 1995; Brekke, 2000). The boundary of Møre Basin is marked by Faeroe-Shetland Escarpment from the west, Møre-Trøndelag Fault Complex to the southwest and by Jan Mayen Lineament from the north. Its structural elements have NE-SW trend consisting of highs, ridges and smaller basins and it is about 9s twt (two way travel time) thick from the axial part. Its main tectonic episode was in Mid-Jurassito Early-Cretaceous rifting and was formed by the subsidence of its flanks as a result of rifting (Brekke, 2000).

2.2.6) Møre-Trøndelag Fault Complex

It comprises the south eastern margin of Møre Basin and consists of NE-SW trending fault-controlled ridges and smaller scale basins. Its trend follow the dominant orientation of structures formed during Caledonian deformation and has been subject to reactivation various times in geological record. As a result it has affected the Paleozoic, Devonian, Jurassic age rocks and Precambrian basement (Bering 1992; Grønlie et al., 1994; Brekke, 2000; Blystad et al., 1995).

2.2.7) Trøndelag Platform

As shown in the structural map Trøndelag Platform, Vøring Basin and the Vøring Marginal High are the middle structural provinces bounded by Jan Mayen and Bivrost Lineaments.

Trøndelag Platform is present between Vøring Basin and Norwegian mainland and is about 160 km. Wide horst and half-grabens present in the inner portions of Trøndelag Platform are characterized by tectonic activity which took place in Carboniferous to Late Permain times (Brekke, 2000).

However, continued activation of some major extensional faults until the Triassic age resulted in en-echelon NE-SW trending basins like Froan Basin, which were filled by Triassic to early Paleozoic sediments and lies southwards (Brekke, 2000).

Froan Basin is separated from inner parts of Trøndelag Platform in NW direction by Vingelia Fault Complex which shows signs of reactivation in both Jurassic and Cretaceous ages. From NW to SE-direction Froan Basin fill becomes progressively thin/shallower. This thinning is attributed to two factors. First, natural thinning of basin fill to the landward direction coupled with erosion and uplifting during mid to Late Jurassic (Brekke, 2000).

Interior parts of the Trøndelag Platform experienced small scale faulting in mid-Jurassic to Early-Cretaceous partly by faulting along the flanks of Helgeland Basin and reactivations of faults present in Vingleia Fault Complex. The same tectonic phase produced intense faulting in Dønna and Halten Terraces. It also resulted in initiation of subdivision in the deep basin on western side was also started during the same tectonic stage (Brekke, 2000).

However, Halten Terrace and Trøndelag Platform had the same elevation until Early-Cretaceous tectonic activity. Thus Nordland Ridge and Froya high present on the edge of Trøndelag Platform had the same elevation levels as the Sklinna until Early-Cretaceous (Brekke, 2000).

3.1) Seismic Waves;

Seismic waves are a form of energy. These are caused by a sudden disturbance of the rock in earth. The source of disturbance could be natural i.e. earthquakes or man-made i.e. dynamite etc. These travel through the earth and are recorded at recording stations.

There is different kind of seismic waves depending upon the nature of their motion. However two most important categories are surface and body waves. Body waves can penetrate the earth while surface waves can only propagate into the shallow earth i.e. close to the surface. Therefore, body wave's propagation is used to study the earth's interior. As this thesis deals with ray-tracing and modeling of body waves, so only these will be discussed in detail.

There are two types of body waves, P and S-waves.

3.1.1) P-Waves;

P or primary waves are the fastest travelling waves and are first to reach a seismic station. These are also called pressure waves as they travel in the form of compressions and rarefactions. P-waves can travel through both liquids and solids. The wave's propagation direction is in the same direction as the particles motion direction.

Mathematically, the expression for p-wave velocity (Vp) can be written as;

$$Vp = \sqrt{\frac{\kappa + \frac{4}{3}\mu}{\rho}} \qquad (3.1)$$

In the above equation 3.1 the term 'κ' represents the bulk modulus of rocks, shear modulus is denoted by 'μ' while Greek Symbol 'ρ' is used to represent the density of the rocks.

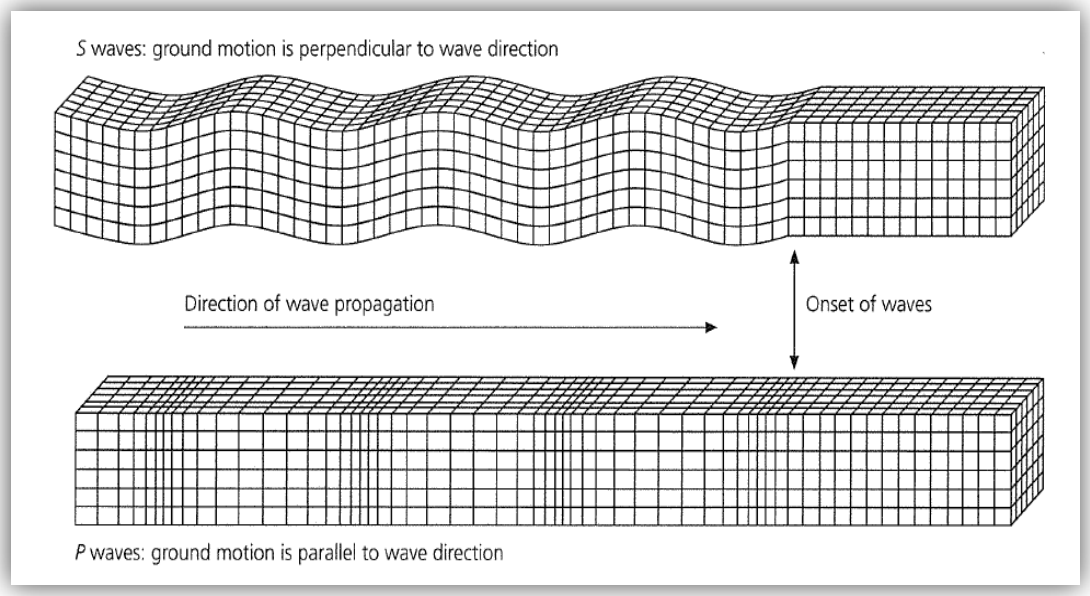

Figure 3.1; *P and S-waves described at any time‘t’ in space. Small cubes represent the particles of the medium. S-wave distorts the material shape without any volume change while p-waves produce a volume change (Stein and M. Wysession, 2009)*

3.1.2) S-Waves;

S-waves (shear waves) are also called secondary waves because of their slower propagation nature as compared to the p-waves. The particle motion is perpendicular to the wave propagation, so s-waves are also called shear waves. These can’t pass through fluids because they have a shear modulus of zero. This property of S-waves led to the conclusion that earth’s outer core is liquid. S-waves are also called as Transverse waves because of perpendicular relation between particle motion and wave propagation.

Mathematically, s-wave velocity ‘Vs’ can be written as;

$$V_s = \sqrt{\frac{\mu}{\rho}} \qquad (3.2)$$

Shear waves can be further classified in to two more categories,

SV-waves; for this both the direction of wave propagation and particle motion is perpendicular but in vertical plane.

SH-waves; the direction of wave propagation and particle motion is in horizontal plane.

3.1.3 S-wave Splitting;

Any material which has the same physical properties in all the directions is called isotropic. While anisotropy is the result of material's different physical properties in different directions, called heterogeneity.

Shear wave's velocity in any material is dependent upon its shear modules. When shear modulus is different in different directions then it can split up into two separate pulses. One in fast direction and other one is slower direction as shown in figure 3.2 below (Wysession, 2002)

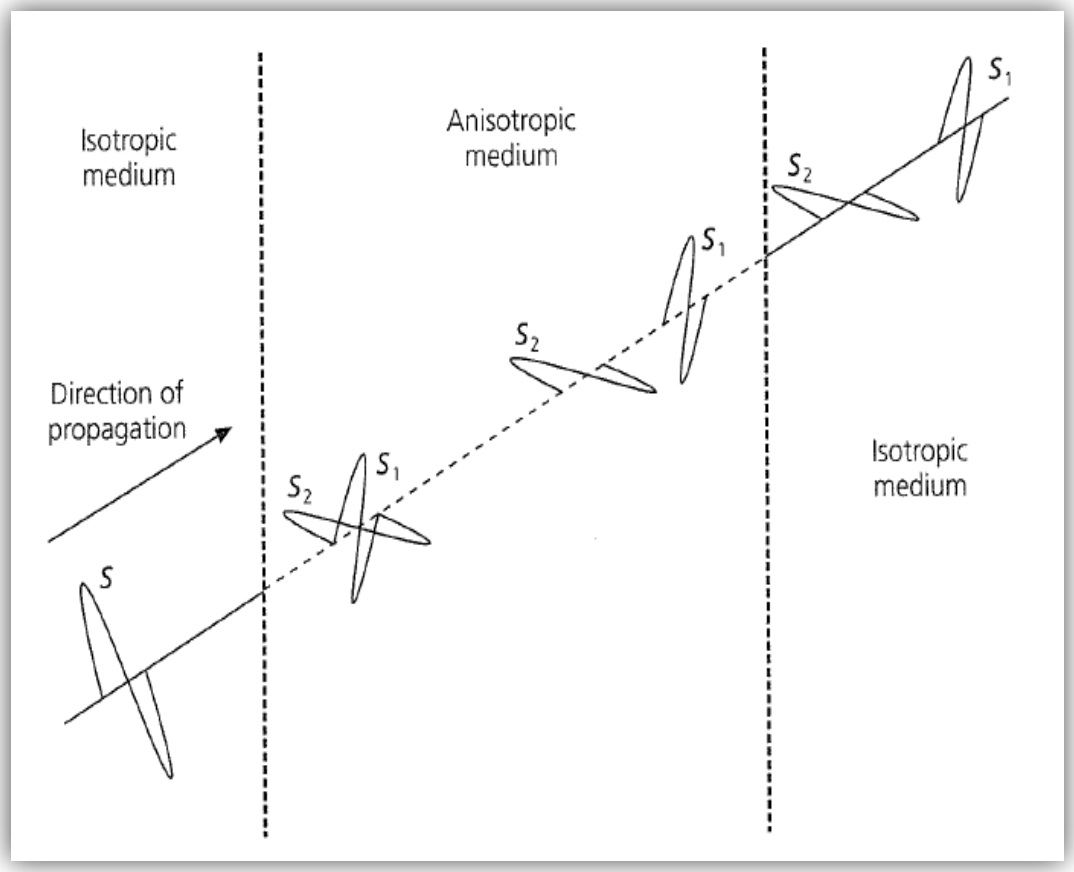

Figure 3.2; *Splitting of an s-wave into two pulses. S1- in fast direction and S2- slow direction (S. Stein and M. Wysession, 2009).*

3.2) Ray Theory;

Rays are defined as normal to a propagating wave front and point in the direction of the propagation of wave field. It is a high frequency approximation of the wave theory. Therefore, for it to hold the change in the medium physical parameters i.e. P and S velocities should not be much as compared the length of the dominant wavelength (Daley and Krebes, 2004).

If above conditions are met, then the propagating wave's travel time T(x) for the source of seismic energy to a subsurface point **x** = (x, y, z) in an isotropic and heterogeneous medium that follows the Eikonal Equation (Daley and Krebes, 2004).

i.e.

$$(\nabla T)^2 = \left[\frac{\partial T}{\partial x}\right]^2 + \left[\frac{\partial T}{\partial y}\right]^2 + \left[\frac{\partial T}{\partial z}\right]^2 = \frac{1}{v^2} \qquad (3.3)$$

Where $v=v(x)$ is the velocity of the seismic wave.

Let us suppose an isotropic and heterogenous medium in which the velocity of the wave 'v' varies smoothly with its location **x**. Then for any wave velocity v(x), its ray path can be calculated with the help of following differential equation and manifested in figure3.3 (Daley and Krebes, 2004).

$$\frac{dx}{ds} = vq \quad and \quad \frac{dq}{ds} = \nabla\left[\frac{1}{v}\right] \qquad (3.4)$$

Where q is the slowness vector q is tangent to the ray path at any point in space and has the same direction as the wave travel path (Daley and Krebes, 2004).

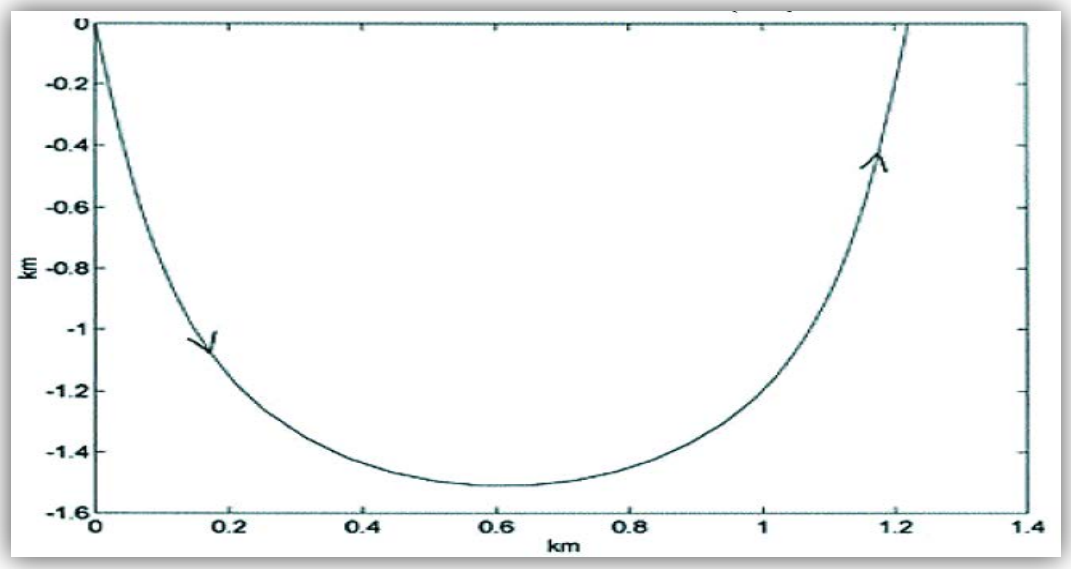

Figure 3.3*: Ray path in a vertically heterogeneous half space in which wave velocity varies with depth z as v=exp (z^2). Ray has a 5.74^o take-off angle with a travel time of 1.79 s (Daley and Krebes, 2004).*

3.2.1) Snell's Law and Wave Conversions;

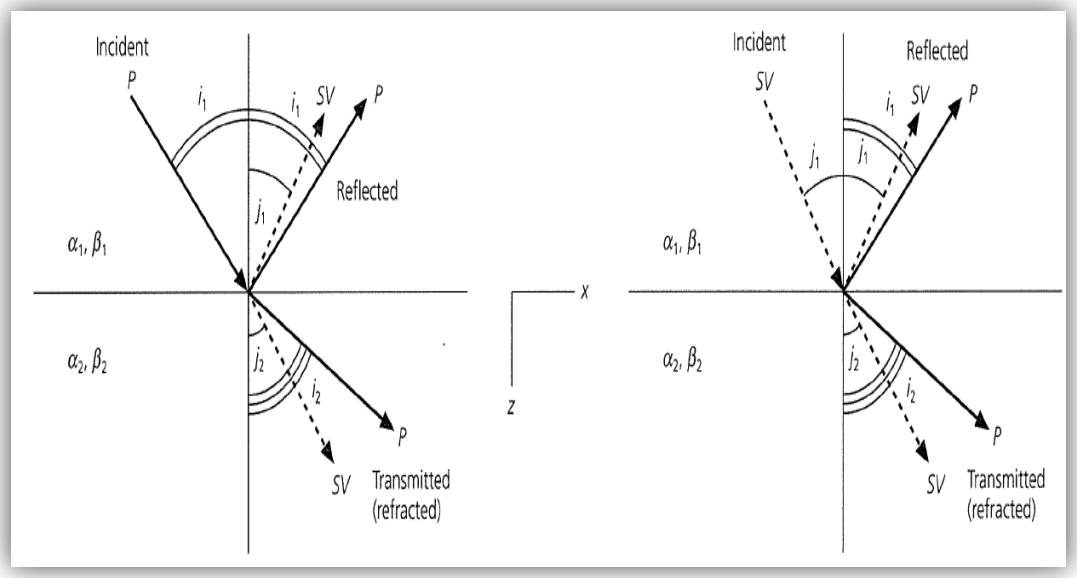

Figure 3.4; *a plane wave travelling from lower to higher velocity medium (both solids). An incident p-wave converts into to two reflected and refracted SV and P waves. 'α_1' velocity of p-wave is first medium, 'α_2' velocity of p-wave in 2nd medium, 'β_1' velocity of s-wave in first layer, 'β_2' velocity of s-wave in second layer. The same case is with SV wave (Stein and M. Wysession, 2009).*

Snell's law represents a mathematical explanation of any physical change in the direction of any wave-front when it impinges upon a lithological layer having some acoustic impedance contrast (z=velocity of wave × density of the material) and the conversion of the p or s-wave at the boundary of the media. Change in the direction of wave-front may include refraction or reflection (E.S. Robinson and C. Çoruh, 1988).

Mathematically, it is written as,

$$c_x = \frac{\alpha_1}{sini_1} = \frac{\beta_1}{sinj_1} = \frac{\alpha_2}{sini_2} = \frac{\beta_2}{sinj_2} \qquad (3.5)$$

Where c_x is the apparent velocity of the wave (S. Stein and M. Wysession, 2009).

As shown in figure; 3.4, the incident p-wave is inclined to the interface. It means it has both longitudinal and transverse sense of particle motion; therefore, both p and s-waves are generated. The change in direction of the refracted p and s-waves is related to the acoustic contrast between the two media. The greater the contrast more will be the deviation of refracted rays from the normal (S. Stein and M. Wysession, 2009).

Since as the Snell's law requires that apparent velocity 'c_x' of all generated waves at an interface to be the same, S-waves are closer to the normal than the p-waves, because they travel at lesser speeds in any medium as compared to p-waves. In case of more interfaces, since all the generated waves satisfy Snell's law and have same ray parameter 'p', so a ray can be traced (S. Stein and M. Wysession, 2009).

3.2.2) Theoretical Partitioning of Seismic Energy at crust-Mohorovicic interface;

As it has been shown in figure 3.4 above that when an inclined p-wave ray is incident on an acoustic interface, it gets converted into reflected and refracted P and SV-waves. At a boundary the tangential and normal components of the displacement must be continuous (S. Stein and M. Wysession, 2009).

The figures 3.5 show various theoretical cases of p and s-waves incident upon Mohorovicic discontinuity (S. Stein and M. Wysession, 2009).

At this discontinuity four different waves are generated and according to law of conservation of energy, the sum of all of their energies must be equal to 1.

For an incident p-wave most of the energy (97%) is transmitted as p-wave for angles of incidence less than the critical angle i.e. 58° as shown in the figure 3.5. After the critical angle, the ratio of reflected p-wave energy increases to about 90%, however, this time the ratio of converted s-waves (both reflected and refracted) increases up to 10%. For a p-wave incident from below the equation remains almost the same except there is no critical angle as the wave enters from higher to lower velocity layer. It should be noted that at zero incidence angle, whole of the p-wave is transmitted (S. Stein and M. Wysession, 2009).

Similarly, for an SV-wave almost 99% of the energy is transmitted as s-wave at the zero angle of incidence while about 1% is reflected as sv-wave and no p-wave is generated. After 20^{o} of incidence, the pattern starts to change slowly, and the strength of reflected SV-wave energy increases on the strength of transmitted energy until the critical angle (58^{o}) reaches. After it, SV-wave energy vanishes (S. Stein and M. Wysession, 2009).

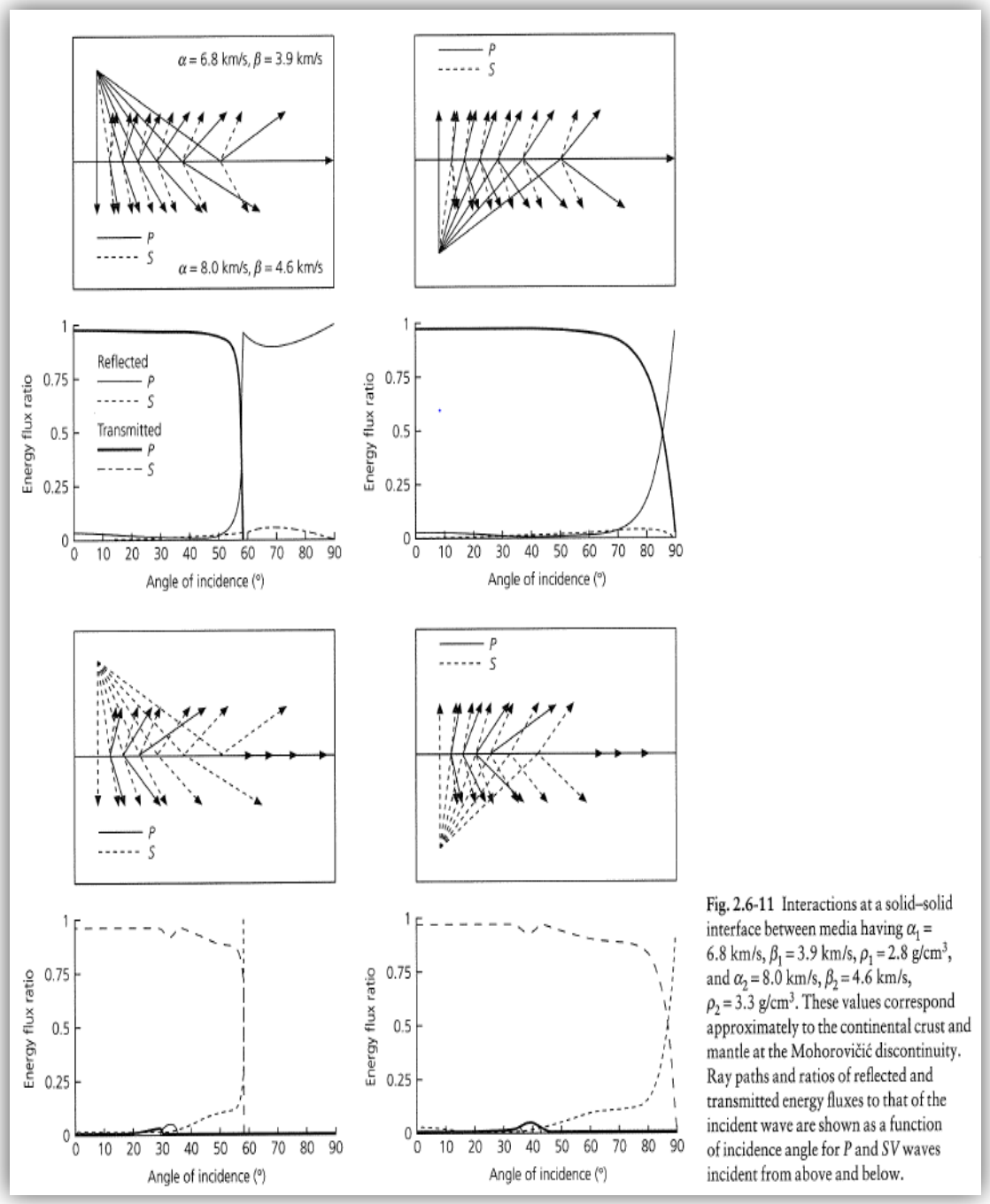

Fig. 2.6-11 Interactions at a solid–solid interface between media having α_1 = 6.8 km/s, β_1 = 3.9 km/s, ρ_1 = 2.8 g/cm^3, and α_2 = 8.0 km/s, β_2 = 4.6 km/s, ρ_2 = 3.3 g/cm^3. These values correspond approximately to the continental crust and mantle at the Mohorovičić discontinuity. Ray paths and ratios of reflected and transmitted energy fluxes to that of the incident wave are shown as a function of incidence angle for *P* and *SV* waves incident from above and below.

Figure 3.5; *Partitioning of P and S-wave energy at Solid- Solid interface (S. Stein and M. Wysession, 2009).*

3.2.3) Theoretical Partitioning of Seismic Energy at ocean bottom interface;

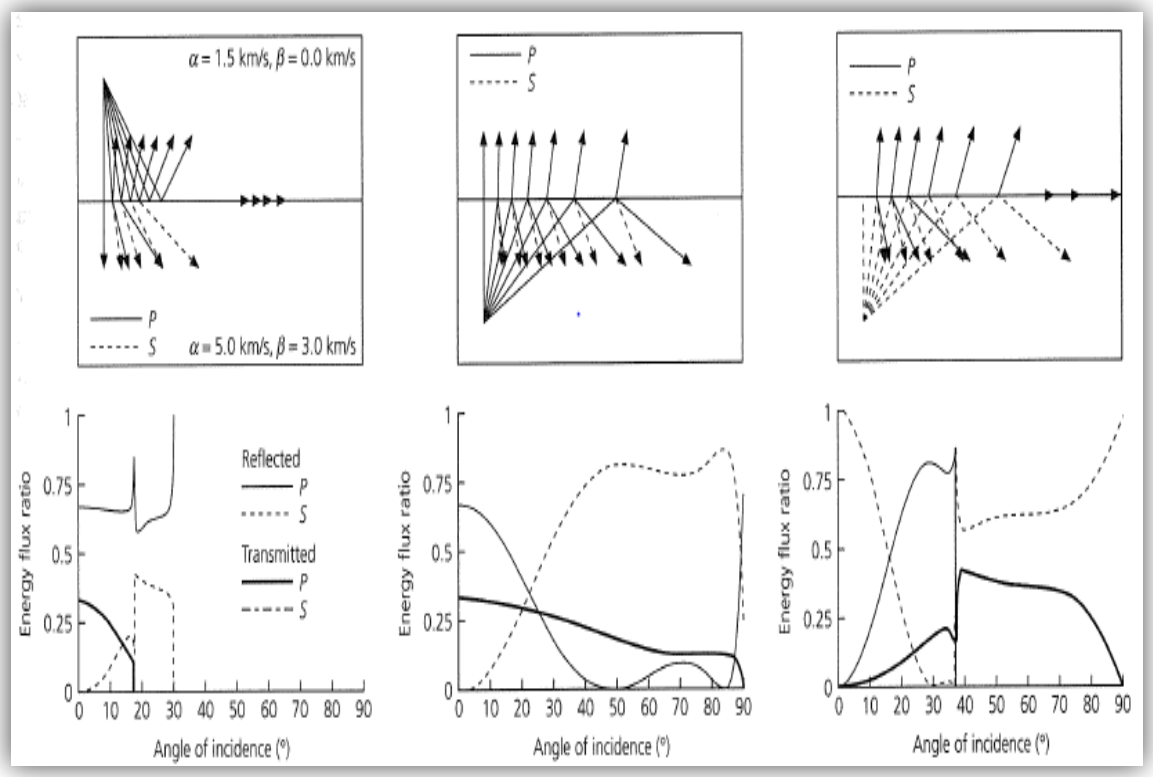

Figure 3.6; *Energy flux ratio and ray paths at ocean bottom interface i.e. overlying water layer and under lying crust are shown. Three cases (left to right), i) incident p-wave from water, ii) incident p-wave from crust and iii) incident s-wave from below (S. Stein and M. Wysession, 2009).*

In this situation for a p-wave incident from above, there is a large difference of energy flux ratio as compared to crust-Mantle boundary. Because the acoustic impendence contrast is much more at sea floor-crust interface. Higher values of the AI contrast are due to the greater velocity and density contrast between sea floor-crust interface than the crust-mantle interface. At near zero angles of incidence, about two-third of p-wave energy is reflected and only one-third transmits. This is why ocean bottom is called a strong reflector. As the angle of incidence increases, the transmitted S-wave energy increase at the expense of transmitted p-wave energy while reflected p-wave energy remains the same. After p-wave critical angle of 17^{o}, a significant portion of transmitted S-wave exists. For angles of incident greater than the 30^{o} (s-wave critical angle), all the energy is reflected as p-wave (S. Stein and M. Wysession, 2009).

Therefore, above comparison suggest that in case of sea-floor most of the energy is reflected near vertical-incidence angles, while at Moho most of the energy is transmitted for the same

angle ranges. Similarly, in S-wave case, since $\alpha_1 > \beta_2$ in Moho case, so there exists no critical angle of S-wave. At the ocean-bottom interface good amount of p-wave energy is converted to transmit S-wave until S-wave critical angle is reached (S. Stein and M. Wysession, 2009).

Similarly, the results for the two cases are also different for a p-wave incident from below. In this case, most of the p-wave is reflected downward up to the angle of incidence of 20^o. After this angle, most of the reflected energy is in the form of S-wave reflection. However, in Moho case negligible S-wave reflection takes place and most of the energy is transmitted as p-wave until grazing angle, where reflected p-wave dominates (S. Stein and M. Wysession, 2009).

From above example it's clear that a p-wave incident at ocean bottom interface from above give rise to significant amount of S-wave energy and an S-wave incident at ocean bottom interface from below results in substantial amount of transmitted p-wave energy. This fact can be used to study the earth in terms of converted S-waves from incident p-waves at ocean bottom interface. These waves travel down the earth as s-waves and can be recorded at the surface as converted p-waves from s-waves at the ocean bottom interface (S. Stein and M. Wysession, 2009).

The above situation could not be applied to our study area as the acoustic contrast at sea-floor bottom is not so much higher in our case. In above case the p-wave velocity in the crust is 5 km/s while in our case its range is between 1.5-2 km/s. Still most of the s-wave arrivals at OBS's have been interpreted to be converted s-waves at ocean-bottom or very shallow interfaces.

However, in our study area as the Profile-3-03 and Profile-4-03 span from land to sea, therefore two different types of conversion interfaces are observed. For Ocean Bottom Seismometers (OBS) the sea floor or upper shallower interfaces act like a dominant conversion interfaces and majority of the p to s-wave conversions takes place at ocean-bottom or very shallow interfaces. In case of Land-stations the dominant conversion interfaces are represented by the various basement layers. In this case most of the p to s-wave conversions takes place at different basement layers on their way up.

3.3) Poisson Ratio;

Poisson ratio is defined at the ratio of the transverse contracting strain to the longitudinal extensional strain. Usually it is represented by a Greek Symbol sigma, σ.

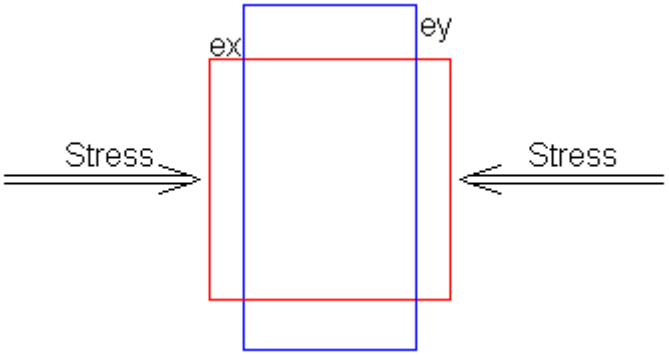

Figure 3.7; *Figure showing concept of Poisson ratio.*

Mathematically,

$$\sigma = {}^{e_y}/_{e_x} \qquad (3.6)$$

Where e_x represents strain in x-direction and e_y denotes strain along y-direction while σ represents Poisson ratio.

The advantage of Poisson ratio is its direct linkage to the material properties which can be measured in the field i.e. P-wave and S-wave velocities (Christensen, 1996).

Mathematically, in terms of p and s-wave velocities it can be written as; (Christensen, 1996)

$$\sigma = \frac{1}{2}\left[1 - \frac{1}{\left({}^{V_P}/_{V_S}\right)^2 - 1}\right] \qquad (3.7)$$

Where *Vp* = P-wave velocity.

And *Vs* = S-wave velocity.

Since in fluids, Vs = 0, so Poisson ratio is 0.5. Average Poisson ratio for continental crust is 0.265 while for oceanic crust is 0.30 (Svetlov et al., 1988).

4) Forward Seismic Modeling Methodology;

4.1.1) Introduction;

Ray Tracing is used to model the complex geological structures both in 2D and 3D domain. Its basic principle is to calculate the path of seismic energy during its propagation from source to receiver and estimating the associated amplitudes and time of travel. It began with the development of ray tracing algorithms, i.e. Cerveny et al. (1977), Spence et al. (1984) and Luetgert (1992).

Because of its simplicity, applicability and easy to understand nature it is widely used for solution of forward and inverse seismological problems. Its application also includes Seismic Tomography and studying the relatively deep geological structures (Julian and Gubbins, 1977).

The travel time forward inversion algorithms developed by Zelt and Smith in 1992 are widely used and are termed as ZS92. These are also the basis of RAYINVR software used for modeling of s-wave in this thesis. It has following distinctions from its counterparts, (modified from Colin A. Zelt, 1999).

- Addition of floating reflectors which don't follow the general velocity field trend.
- Layer interfaces and velocity can be tied.
- Interfaces depths and velocity nodes can be distributed randomly.
- All types of arrivals can be modeled at the same time.

The inclusion of above features allows induction of any previous geological and geophysical information into the velocity model. It also serves to model the sparsely acquired wide angle OBS data to be modeled with better accuracy (Zelt and White 1995).

4.1.2) Identification of Arrivals/Signals;

In order to trace rays and develop a subsurface velocity model first step is the correct identification of seismic signals from seismic stations, in this case ocean-bottom seismometers (OBS). Accuracy and certainty of a model developed by interpretation of wide angle OBS data is directly related to the identification of accurate arrivals. Therefore, the most distinct arrivals, which are the 1st arrivals, are picked first. Then an initial model is developed and is continuously upgraded as more and later arrivals are interpreted. Knowledge of tectonic settings of the area could also be used to make logical predications of the onset of

arrivals. Since the wide angle OBS data is mostly acquired on existing ordinary reflection profiles, so those can also be used to help identify the signals. In sparse and bad quality data, care should be taken not to interpolate the observed events for a smoothed model, as this will result in an inaccurate velocity model. (Colin A. Zelt, 1999).

Automatic picking scheme is seldom used for OBS data because of strong noise, phase changes over larger offsets and weaker signals embedded in large amplitude coda. (Colin A. Zelt, 1999).

Therefore, manual picking scheme was used for the picking of the s-wave signals in this thesis. In this scheme few picks are picked using hand and the intervening signals are picked by the interpolation between the two adjacent hand-picked signals.

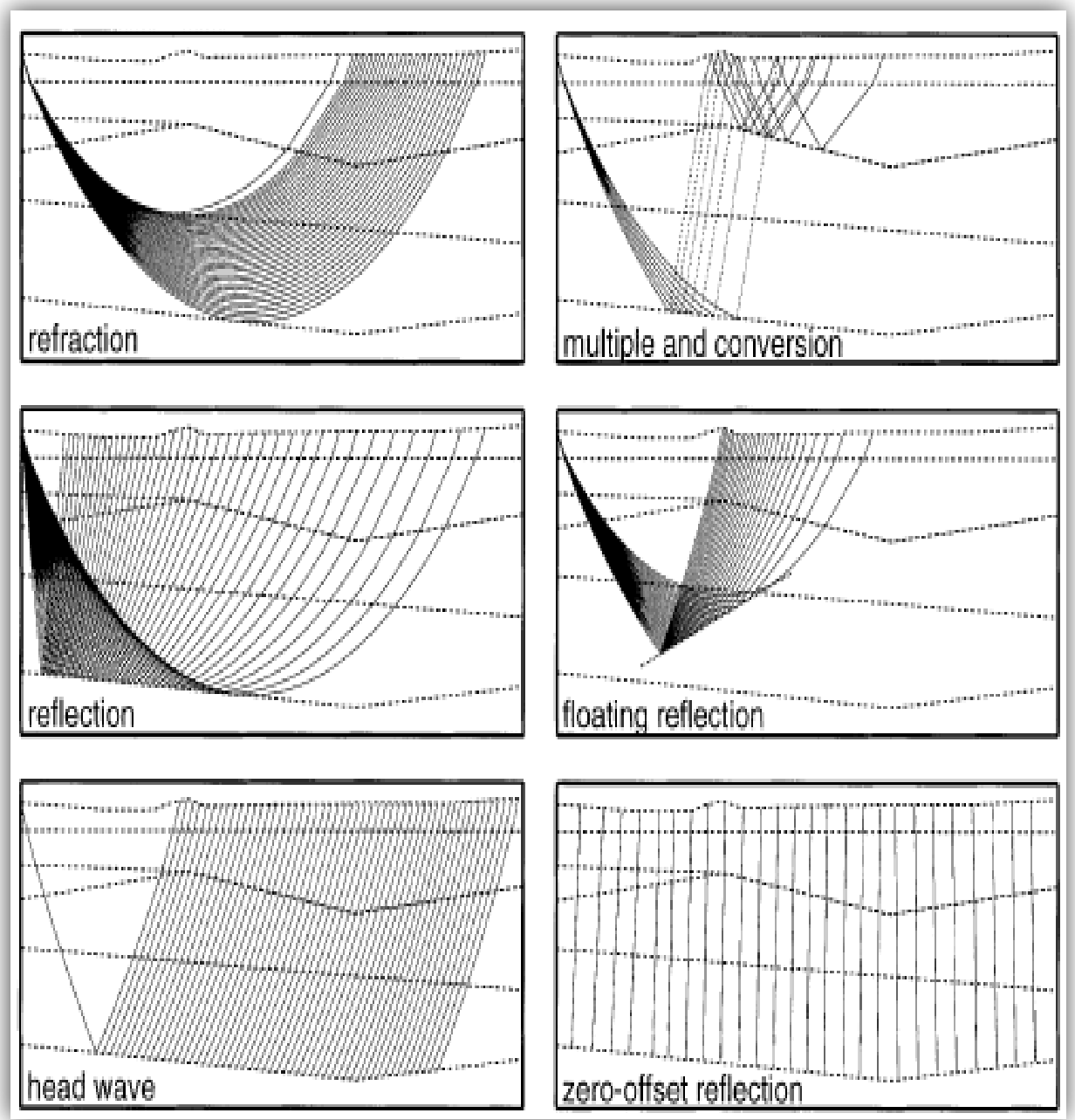

Figure 4.1*; Different types of ray groups used for inversion of wide angle seismic data. Dashed lines represent layer boundaries, while ray paths are represented by solid lines. All the ray-paths could be p or s-wave rays. (Colin A. Zelt, 1999).*

Most of the OBS data contains the following type of seismic arrivals. All the different ray paths shown in above figure are governed by Snell's law and Huygens's Principle. A brief description to the different ray paths is give below.

Refracted Arrivals;

When a ray enters from a lower velocity medium into a higher one, it is refracted away from the normal while it bends towards the normal upon entering from higher to lower velocity medium. In RAYINVR program, the layer in which refracted ray bottoms, should be chosen with caution. It is because that most of the algorithms trace the refracted ray to the travel time that satisfies the earliest arrival at any receiver before comparing this with the observed data. So, due to this refracted phases represent a smooth variation in time with offset and don't exhibit obvious changes in the slope of the arrivals. It should be interpreted as a velocity model with continuous variation with depth rather than a having sharp discontinuities (Colin A. Zelt, 1999).

Multiples;

Any seismic signal/wave that has experienced more than one reflection is called multiple. These can have long or short lag from the primaries and are regarded as noise. In wide angle OBS data mostly only the 1st arrivals are picked so there is usually no need to process the data for multiples removal.

Reflections;

When a seismic wave impinges on a lithological boundary having acoustic impedance contrast, a portion of its energy is reflected back. As in most of the cases, most of the energy is transmitted, so reflection amplitudes are very less and are difficult to observe in wide angle OBS Data. However, in our data, significant amount of reflected waves can be interpreted, originating from sediment-basement and basement-Mantle interface. Both of these interfaces have relatively large acoustic contrasts resulting in detectable reflection strengths.

Floating Reflector;

A floating refection corresponds to an interface that is not necessarily associated with a velocity boundary. It may arise of any localized rock inclusion having different velocity than the general velocity trend resulting in acoustic contrast. In this thesis since signal quality is already poor, so it was not expected to distinguish any such event. Thus, it was omitted from modeling.

Head Wave;

These are generated when there is positive velocity contrast between upper and lower velocity layers. For a wave that impinges on the higher velocity layer at critical angle, head waves are generated.

Zero-offset Reflection,

It is produced when source and receiver are at the same location i.e. no source-receiver separation.

4.1.3) Uncertainty of the Interpretation/Picks;

To avoid over or under-matching of observed and calculated travel times, uncertainty values should be assigned to each pick. A suitable uncertainty value is dependent upon several factors i.e. S/N ratio, amplitude/frequency of the arrivals and overall quality of the data.

Observed and calculated travel time picks are calculated by a mis-fit parameter, called chi-squared denoted by "χ^2" (Bevington, 1969). A value of $\chi^2=1$ corresponds that data has been adjusted according to the specified uncertainties without over or under-fitting. Generally if overall value of $\chi^2<1$ or $\chi^2>1$, it means that model is over or under-fit and it contains details which are not present or vice versa (C. A. Zelt, 1994).

However, this condition is still acceptable if there are very less data points to obtain the suitable chi-values statistically. But, only χ^2 values are not the sole criteria to judge the accuracy of the model. Resolution of the model and ray-coverage density is also very much important. Therefore, in case of poor quality data, the value of uncertainties can be increased logically to make the χ^2 values near to 1 (C. A. Zelt, 1994).

4.1.4) Reciprocity of Travel times;

In order to get consistent interpretation, reciprocal source-receiver pairs must have the same travel times for the same arrivals. Differences of travel times larger than the uncertainty values must be removed before modeling (C. A. Zelt, 1994).

4.2) Modeling Strategy;

Crustal data interpretation is mostly carried out by forward-modeling using a trial and error technique on 2D profile. The theoretical travel time responses of subsurface stratum are compared with observed ones. This trial and error technique results in a velocity model which best matches between theoretical and observed travel times. A number of ray tracing

algorithms has been developed from time to time based on ray theory (Cerveny et al., 1977) i.e. McMechan and Mooney (1980), Cerveny and Psencik (1981), Cassell (1982) and Spence et al. (1984), (C.A. Zelt, 1988).

Velocity parameterization is a distinguishing factor of any algorithm. For any algorithm, the efficiency, accuracy and practicality is directly linked with its velocity parameters (C.A Zelt, 1988).

A sample velocity model is shown in figure 4.2.It is composed of layers and trapezoids. The layers are separated from each other by boundaries, which never cross each other. These boundaries run from left to right and are defined by a specific number of points. Medium present between two boundaries is supposed to be isotropic and homogenous in the direction normal to the model. Vertical boundaries partition the horizontal boundaries into blocks. Vertical boundaries are placed where change in dip or velocity of upper or lower layer line segments takes place. Therefore, vertical boundaries divide each layer into a number of trapezoidal blocks having unique dips and velocities. (C.A Zelt, 1988).

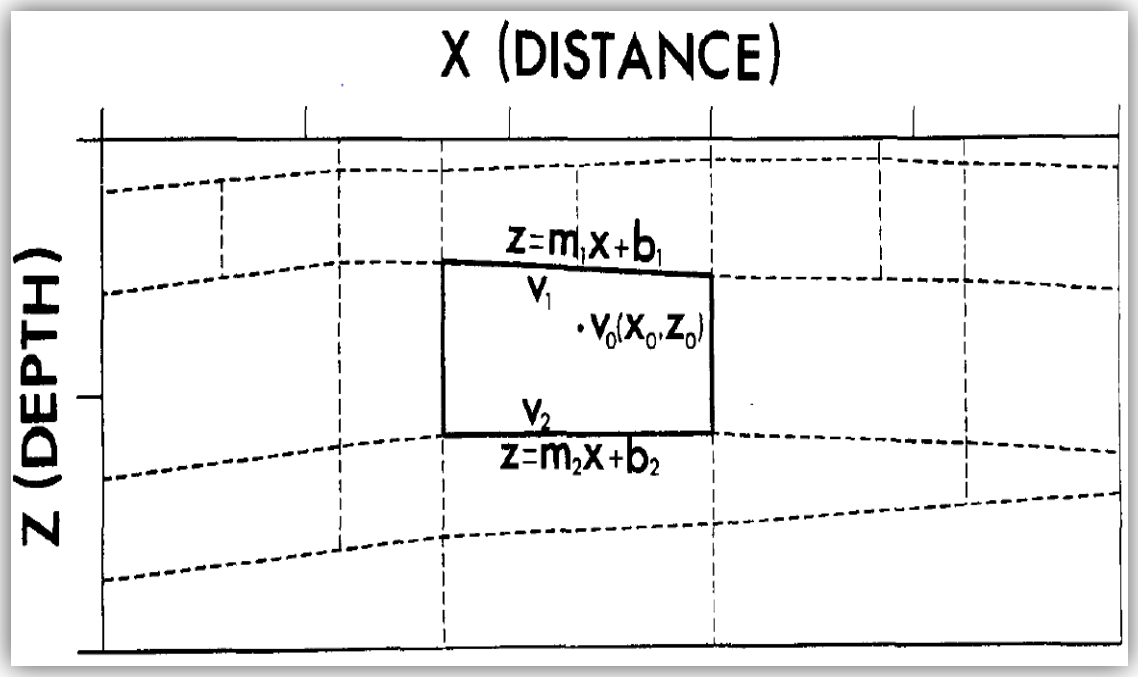

Figure 4.2; *a sample velocity model comprised 27 trapezoidal blocks and 5 layers. Velocity, V_o (x_o, z_o) is calculated from equations 4.1 and 4.2.*

The velocity at any point in a trapezoid is calculated by upper and lower line segments bounding it. The equation of upper and lower line segments is,

$$z = m_1x + b_1 \quad \text{and} \quad z = m_2x + b_2 \qquad (4.1)$$

Therefore, at any point in a trapezoid, the p-wave velocity will be,

$$V_o = [(v_1m_2\text{-}v_2m_1)x_o + (v_2 - v_1)z_o + (v_1b_2 - v_2b_1)]/[(m_2\text{-}m_1)x_o - (b_2\text{-}b_1)] \quad (4.2)$$

In the above equation v_1 and v_2 are the velocities of the above and lower layers in the trapezoid while m_1, and m_2 are the slopes of the line segments.

4.2.1) Programmed Ray Tracing;

In any ray tracing computer program, the rays are traced by solving the ray-tracing equations. Two sets of first-order ordinary differential equations are (C.A Zelt, 1988).

$$\frac{dz}{dx} = \cot\theta \qquad \frac{dx}{dz} = \tan\theta$$

$$\frac{d\theta}{dx} = \frac{(v_z - v_x \cot\theta)}{v} \qquad \frac{d\theta}{dz} = \frac{(v_z \tan\theta - v_x)}{v}$$

(4.3a) (4.3b)

Where initially it is supposed that $x = x_0$, $z = z_0$ *and* $\theta = \theta_0$ (Cerveny et al., 1977, eq. 4.3a and 4.3b).

θ is a variable and is the angle between z-axis and tangent to the ray. Partial derivatives of velocity w.r.to x (offset) and z (depth) axis are represented by v_x and v_z in the equation. Initial conditions are assumed as any point (x_0, z_0) representing the location of source and θ_0 being the take-off angle. The equation 2a accounts when ray travels near-horizontally while 2b considers the near vertical propagation. However, in any case, Snell's law must hold for any type of rays to be traced (C.A Zelt, 1988).

Once one ray has been traced, the step length along x and z-axis, to trace next ray is given by the following equation,

$$\Delta = \frac{\alpha v}{|v_x|+|v_z|} \qquad (4.4)$$

Above equation reveals that in case of strong lateral (v_x)or vertical (v_z)velocity gradients, the ray step length will be small and vice versa. It is because of the fact that in case of strong velocity gradients, large ray bending will occur. Therefore, in order to trace rays accurately, the step length must be smaller. Alpha α, is constant and supplied by the user and it serves as a guarantee to trace the rays with accuracy and efficiency (C.A Zelt, 1988).

In the ray-tracing program three main kinematic ray families are searched based upon their ray- takeoff angles (calculated from the horizontal), in any model layer as shown in figure 4.3. It includes (C.A Zelt, 1988).

Refracted Rays; which refract in the layer. For this class, first the search mode determines the take-off angle of the uppermost and lowermost refracted rays in the layer. Once the upper and lower limit of the take-off angles has been determined, it traces the intermediate family rays according to the maximum number of allowed rays within these limits.

Reflected Rays; This family of rays reflect from the bottom of the layer. In reflected family case, first the smallest take-off angle for the reflected is determined in search mode. Once it has been established, then other family rays are traced from this smallest angle up to maximum angle (mostly 90^0) i.e. vertical.

Head Waves; Such kind of waves propagate along the top of the layer. For such kind of ray family, the search mode looks for those rays which strike the upper boundary of the layer at critical angle. Thus all those rays which emerge at this angle are traced to give a family of head waves.

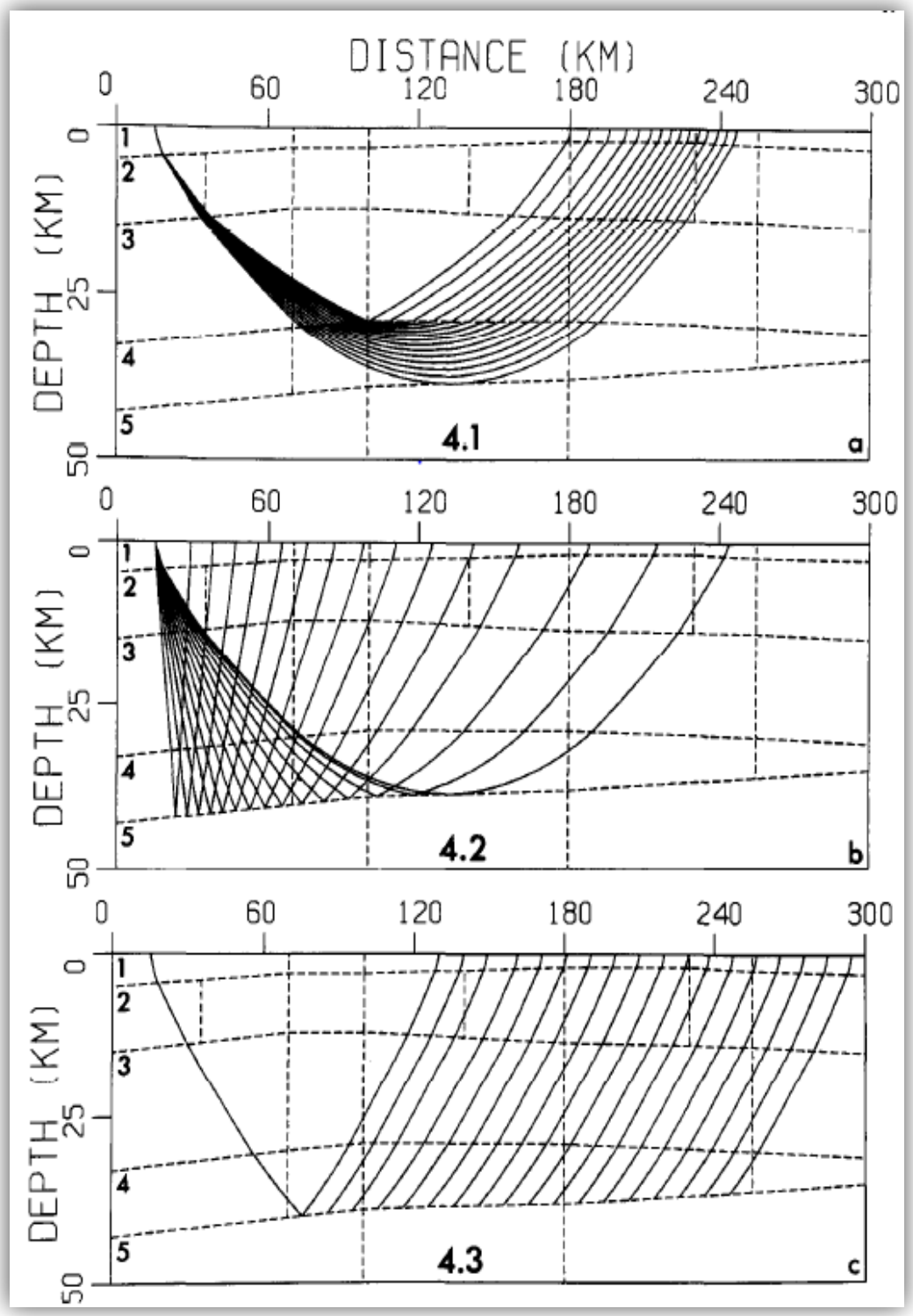

Figure 4.3: *Refracted, reflected and head-wave kinematic ray families. a) Refracted rays (code 4.1), b) Reflected rays (code 4.2) c) Head waves (4.3) (C.A Zelt, 1988).*

4.2.2) Ray Search Mode;

Search mode operates similar for all the three ray types. Let us take the example of determining the take-off angle of an uppermost refracted ray in any layer. For a medium with no lateral variation of the velocity i.e. laterally homogenous, the take-off angle Φ_0 from the horizontal can be written as, (C.A Zelt, 1988).

$$\Phi_0 = 90° - \sin^{-1}\left({}^{v_0}/_{v}\right) \qquad (4.5)$$

In above equation 'v_0'represents velocity function at the source and 'v' denotes the velocity at the top of the specified layer. After tracing the first ray, a second ray is traced using a take-off angle of ($\Phi_0 + \partial\Phi$) if the first ray did not enter the layer or by ($\Phi_0 - \partial\Phi$), if first ray entered the layer. Where $\partial\Phi$ represents a specified portion of the angle difference between uppermost and lowermost take-off angles calculated in the search mode i.e. $|\Phi_0^* - \Phi_0|$. In previous case if the first or second rays did not bisected the layer boundary a new set of rays will be traced using angle ($\Phi_0 + 1/2\partial\Phi$) and ($\Phi_0 - 1/2\partial\Phi$). This practice will be continued until the traced rays bisect the layer boundary as shown in the figure 4.4 (C.A Zelt, 1988).

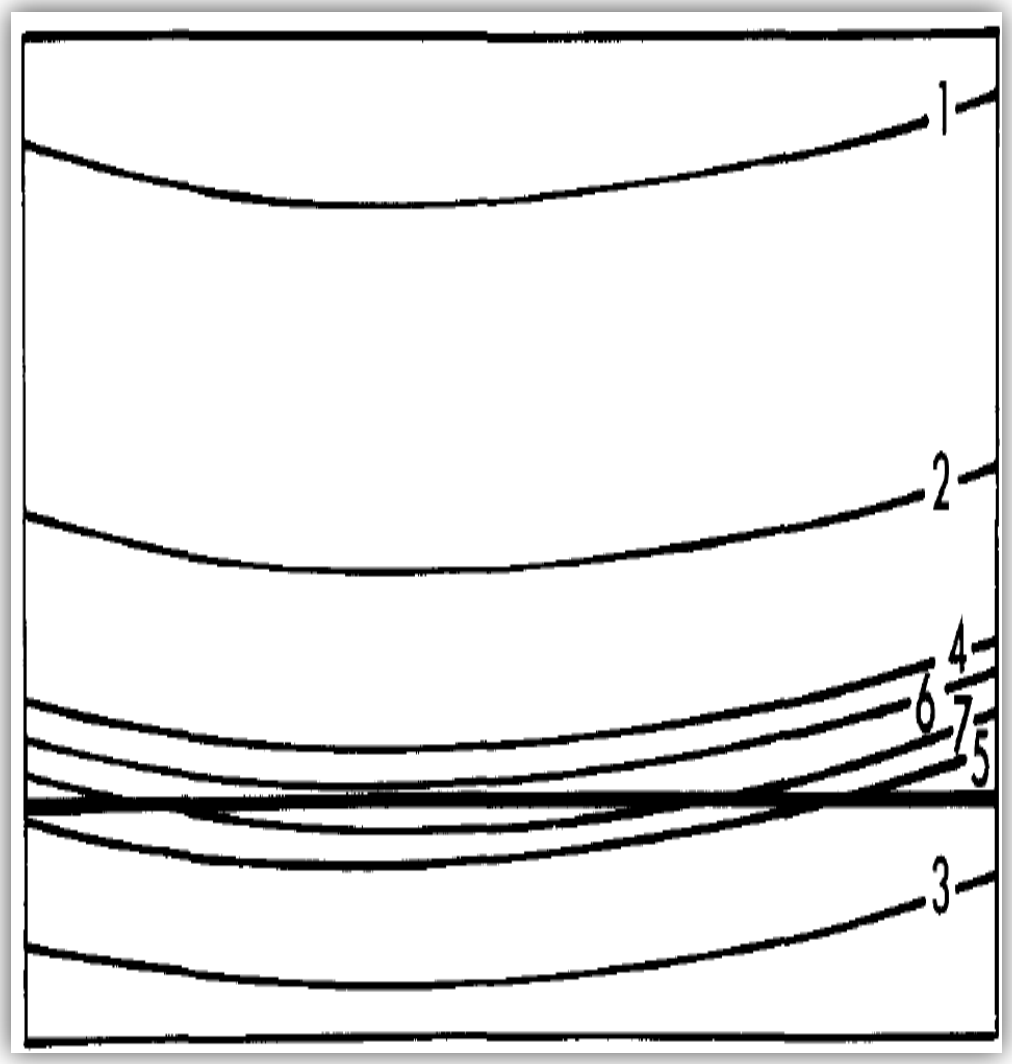

Figure 4.4; *a total of seven rays have been traced for a search to calculate the shallowest or uppermost refracted ray in a layer (C.A Zelt, 1988).*

It has been observed that about ten rays are satisfactory to effectively define the structure however in the case of strong lateral velocity gradients this number can be doubled. Normally, user specifies the maximum number of rays to be traced between two end members. However, software will stop searching for the intermediate rays if the distance between the uppermost and lowermost rays is smaller than the pre-defined distance. The traced ray family can be subjected to any type of conversion or layer boundaries. For example P-S or S-P conversions, free surface or multiple reflections. Similarly if the location of shot points in below the surface of the model, still rays can be traced as moving upward (C.A Zelt, 1988).

The search mode traces the rays in kinematic sense i.e. looks for a specific whole family of rays of any type rather than two-point ray-tracing approach when is based upon tracing the

rays up to a specific receiver (cf. Cassell, 1982). Kinematic ray tracing has the advantage that a specific portion of the model can be studied using a specific family of rays (C.A Zelt, 1988).

5) Processing of wide-angle seismic data;

It is almost impossible to extract any geological information from the raw data acquired in the field. Therefore, it must be processed. Basically, processing consists of a series of computer routines which are applied on the raw data. It increases the signal to noise ratio and results in interpretability of the data.

Processing of OBS data was carried out in Seismic Unix. In our case the following steps were used.

- Velocity reduction
- Band-pass filtering
- Automatic gain Control (AGC)
- Spiking Deconvolution
- Rotation of the horizontal components of OBS and Land Data.

Above processing steps are explained in detail below.

5.1) Velocity Reduction;

It is done by changing the time axis to (time – offset/V.red). V.red denotes the reduction velocity. Reduction velocity is chosen on the basis of objective of the study and it aids in the interpretation of the arrivals. In crustal scale refraction studies, the data is often reduced by 8km/s. It is because of the fact that P-wave velocity in the upper mantle is of this magnitude.

However, in our case, as the purpose was to enhance s-wave arrivals, a reduction velocity of 4.62km/s was applied because it represents s-wave velocity in upper mantle. In this way s-wave arrivals from upper mantle or Moho appear as near horizontal events, and are easily identifiable. Similarly those arrivals which have lower apparent velocities than the V. red appear as having positive slopes and vice versa as shown in the figure 5.2 below. Positive slope means that for any family of s-wave arrivals, as the offset increases from the OBS location, it arrives at later times at farther traces. Whereas, the term negative slope suggests that farther offset arrivals come at lesser times for any family of ray paths.

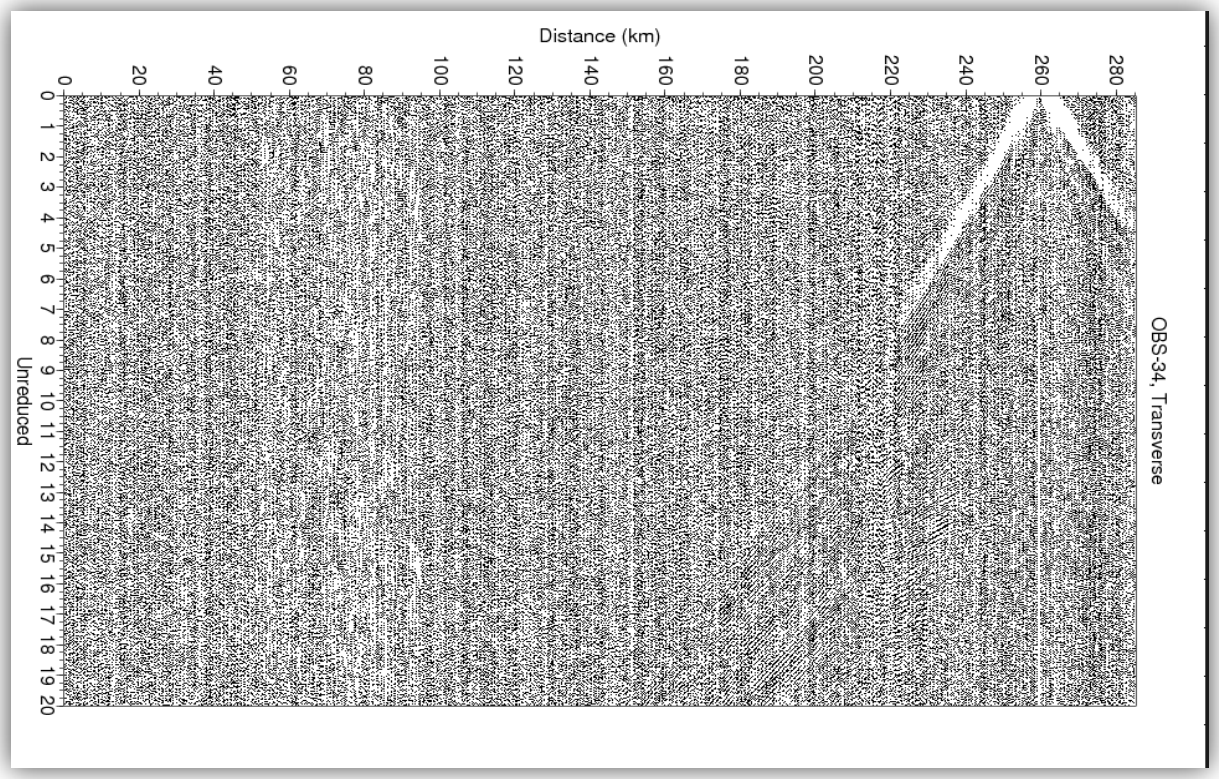

Figure 5.1: *(Above) Profile-4, OBS34, without any Velocity Reduction applied.*

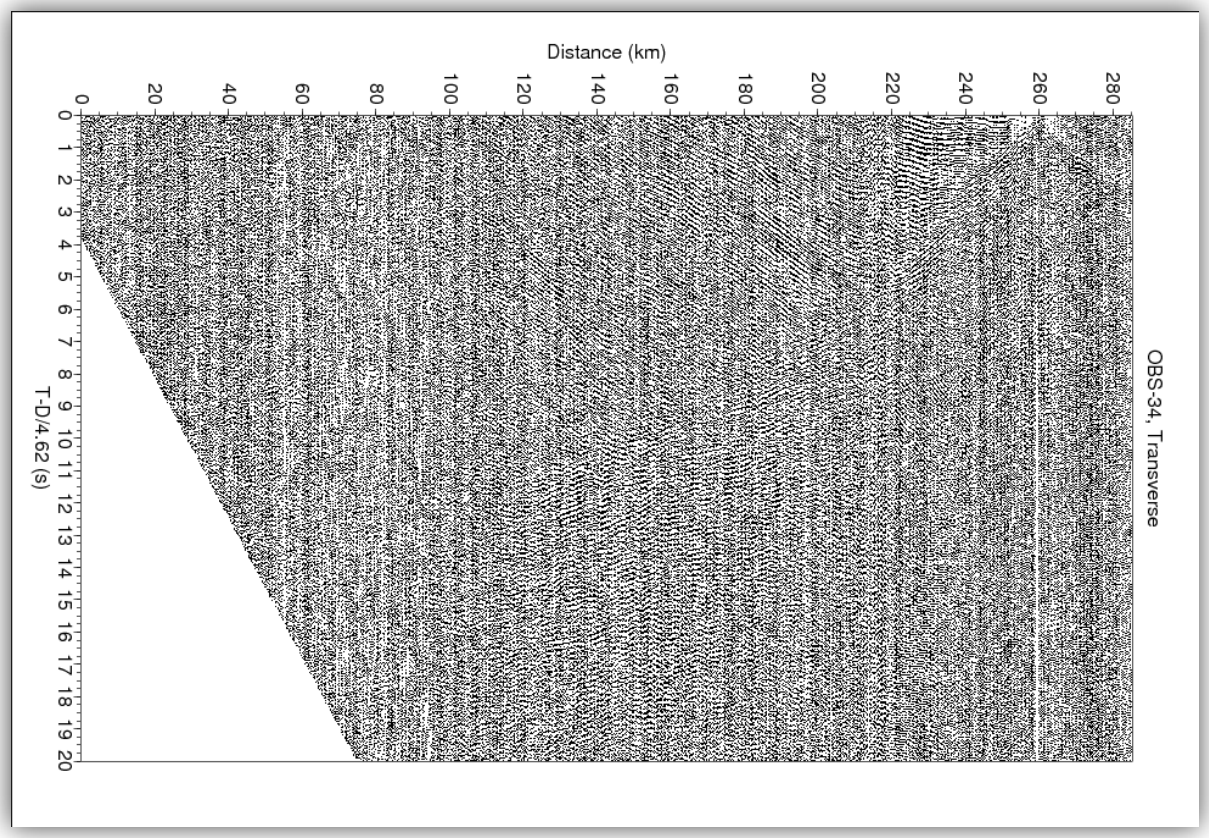

Figure 5.2: *(Above) Profile-4, OBS34, Reduction Velocity of 4.62 applied.*

5.2) Band-pass filtering;

The recorded seismic data contains both signal and noise. Signal is that portion of data which carries subsurface geological information while noise consists of all the remaining portion.

Noise can be further subdivided into two types based upon its appearance in the seismogram, i.e. random and coherent.

Random noise does not show any specific pattern and is mostly connected with factors not related to the survey for e.g. wind, vehicles, rain or any vibration caused by marine traffic. While coherent noise follows a distant pattern and shows continuity from trace to trace. It may distort the seismic signal. Its definition is based upon the nature of investigation being carried out. For example in case of wide-angle OBS survey, refracted arrivals represent signals while in reflection surveys, they are classified as coherent noise. Other examples of coherent noise include, cable noise, multiples, diffractions, direct waves and out of plane reflections.

There are various ways to remove seismic noises. Mostly frequency filtering of the seismic data is used to get rid of noises. It is particularly helpful when signal and noise have different frequency spectra.

In our case a band pass filter 4-6-14-16 was used to suppress the noises. It allows passing only those frequencies which are above 4 Hz and lower than 16 Hz.

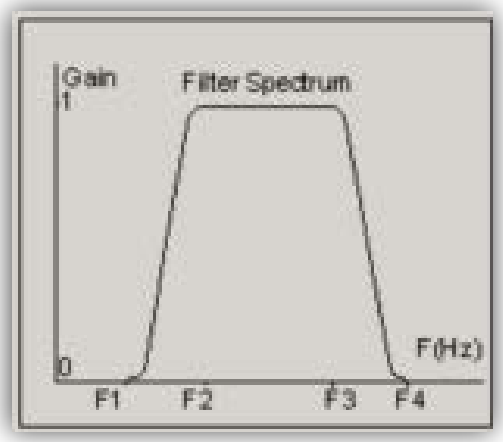

Figure 5.5; *Bandpass filter, F(Hz) represents frequency spectrum of the output. F1=4, F2=6, F3=14 and F4=16 (Source= SeisView)*

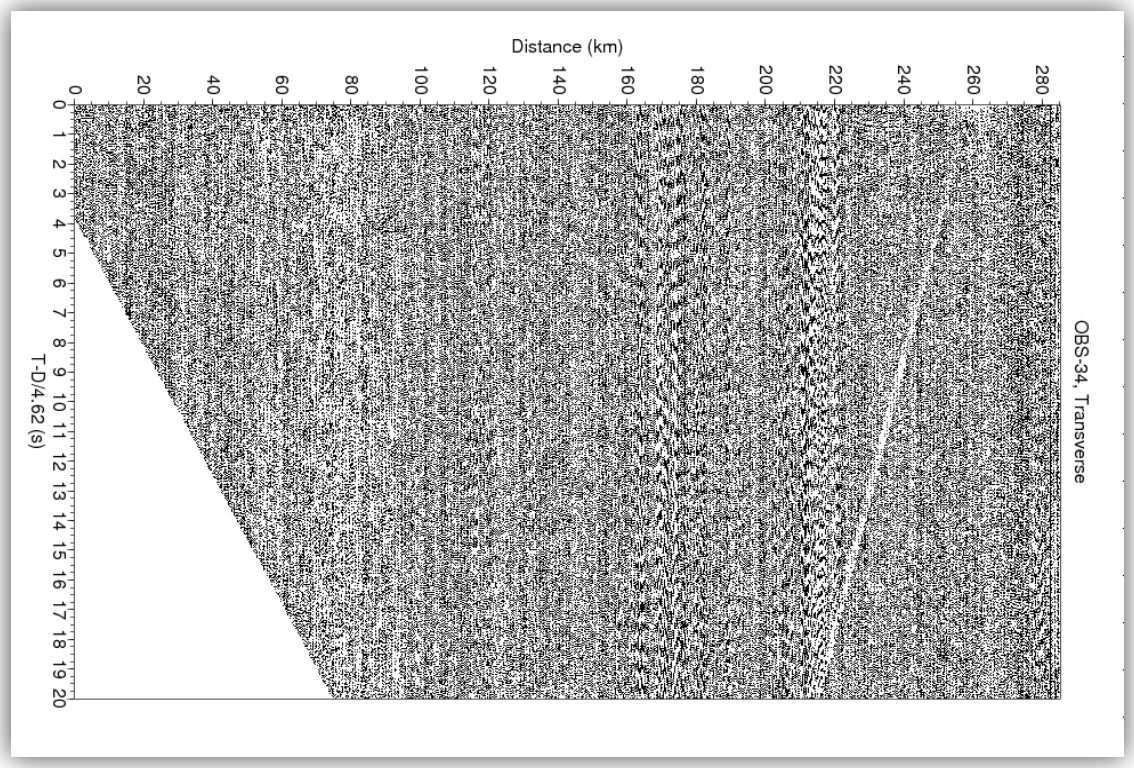

Figure 5.6*; Profile-4, OBS-34, before band-pass frequency filtering. Note the low frequency (high amplitude) random noise and coherent low frequency direct waves in a 4.62 km/s velocity reduced and AGC applied data.*

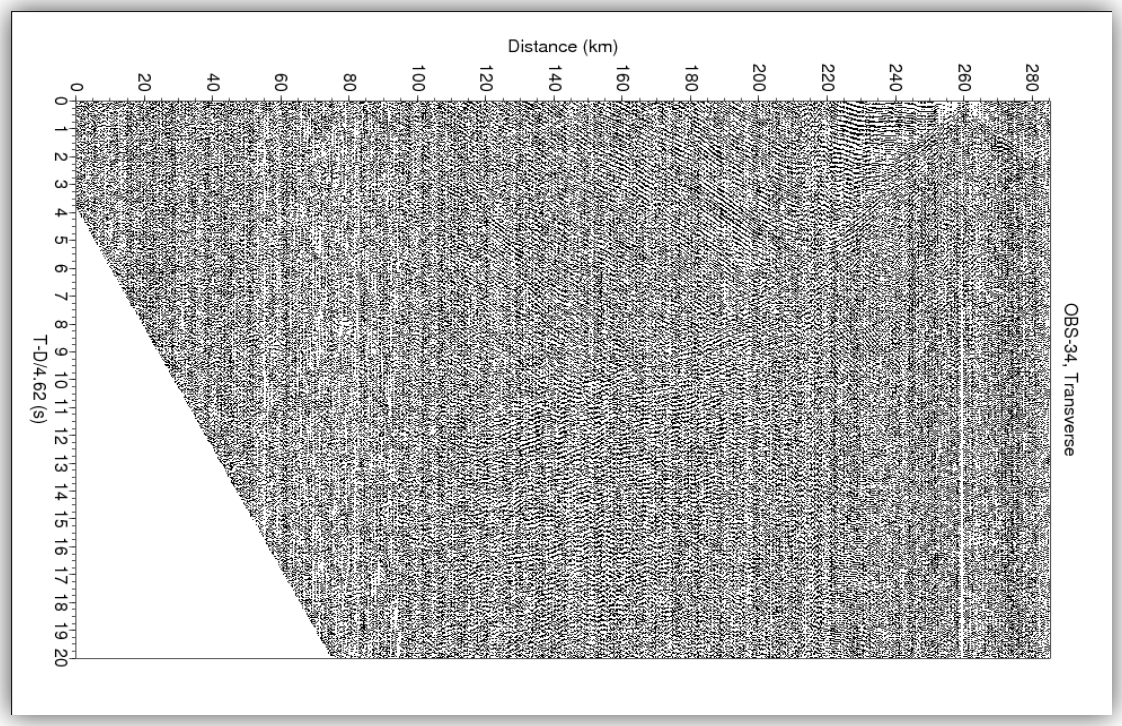

Figure 5.7; *Profile-4, OBS-34, Band-pass frequency filtering attenuates the above mentioned noises and enhances the S/N ratio.*

5.3) Spiking Deconvolution;

Initially when a seismic pulse is generated by a source, it contains all the frequencies which are characteristic to that source and is compressed in time domain as shown below in figure 5.8. As it travels down the earth, its shape changes as a result of absorption of energy through the earth and geometrical spreading. This results in loss of higher and higher frequencies and lengthening of the initial spike.

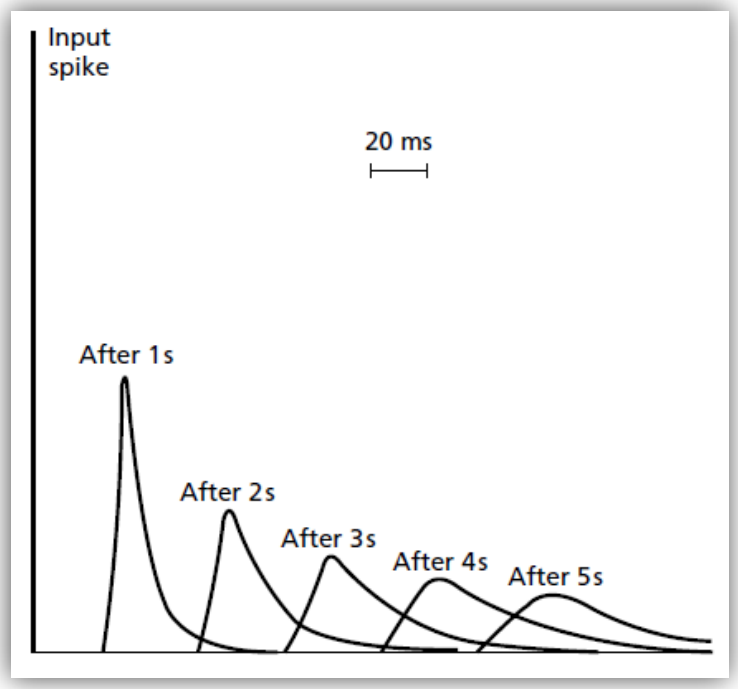

Figure 5.8; *Progressive change of shape of an initial spike as it attenuates through the earth with time (After Anstey 1977).*

Deconvolution is an inverse filtering procedure. It attempts to restore the original shape of the seismic pulse to a spike by introducing the lost frequencies.

Different kind of deconvolution schemes can be used for various purposes. However, in this case Spiking/Whitening Deconvolution was used. To compress the wavelet, white noise (the same amplitude for all frequency components) was added to the data. It improved the vertical resolution of the data as shown in figure 5.10 (Kearey, 2001)

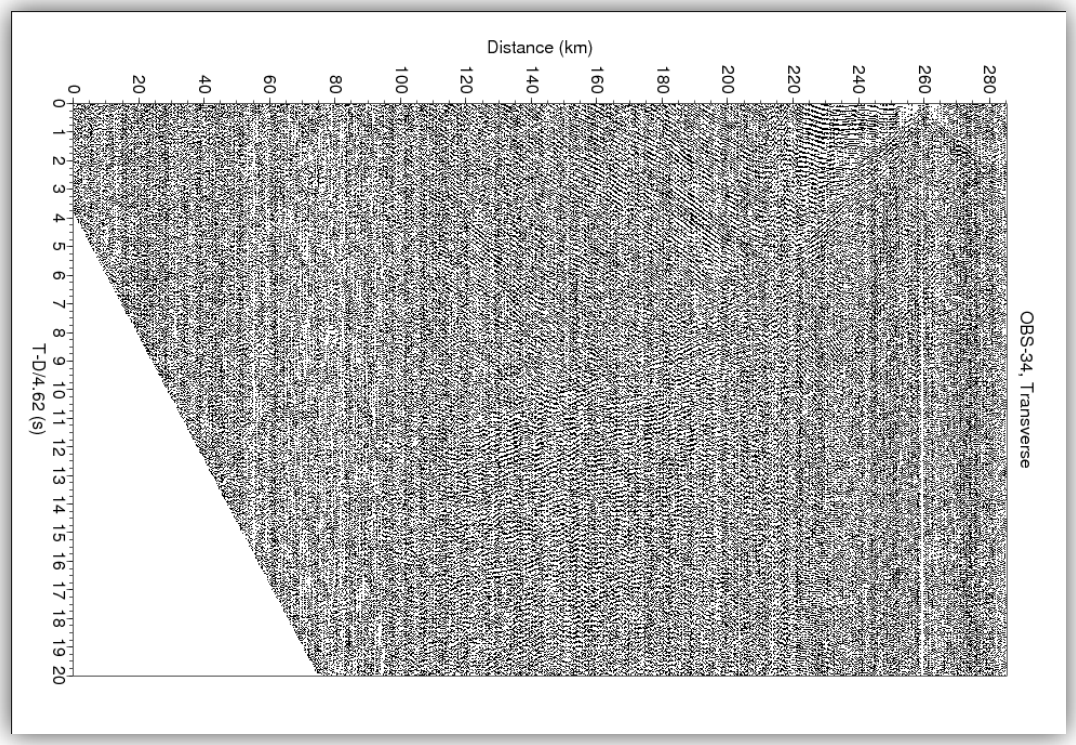

Figure 5.9; *Profile-4, OBS-34 without deconvolution but V.red=4.62 km/s and AGC applied.*

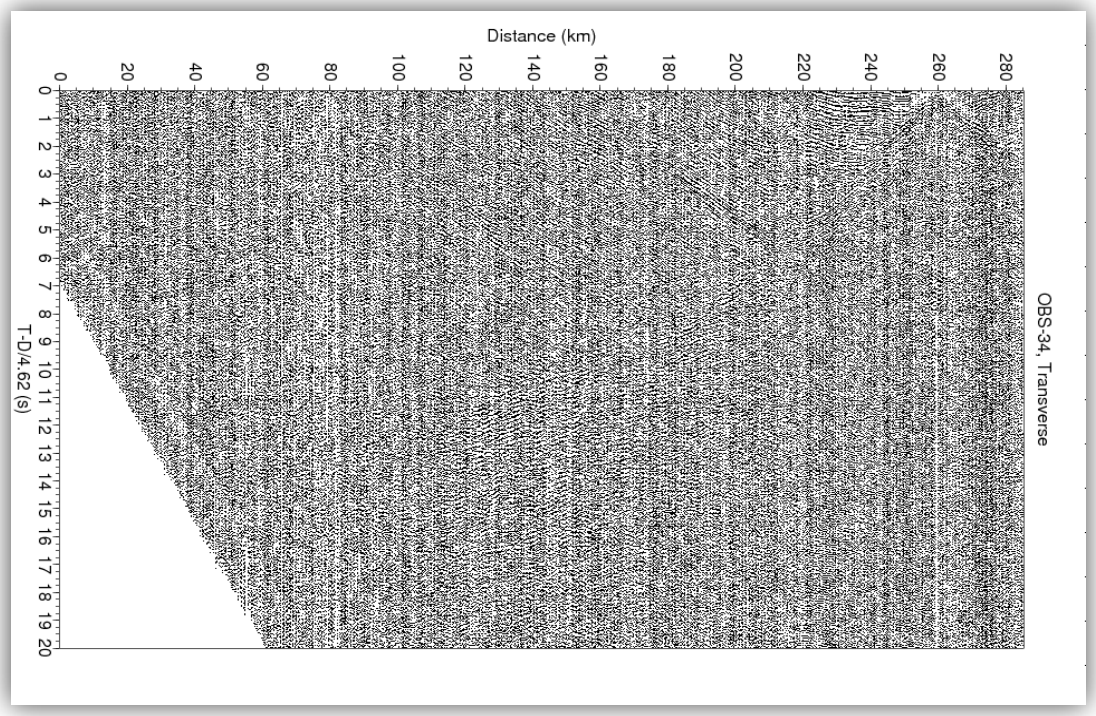

Figure 5.10*; the same record (Figure; 5.9) with deconvolution applied. It results in compressed wavelet and increased vertical resolution.*

5.4) Automatic Gain Control;

As it has been previously discussed that seismic pulse experiences absorption and geometrical spreading when it travels into the earth. As shown in figure 5.11 below, the losses are directly related to the offset and the depth to which pulse travels. Large offset and later arriving signals diminish in amplitudes much more than the preceders. Therefore, they must be amplified for better interpretation.

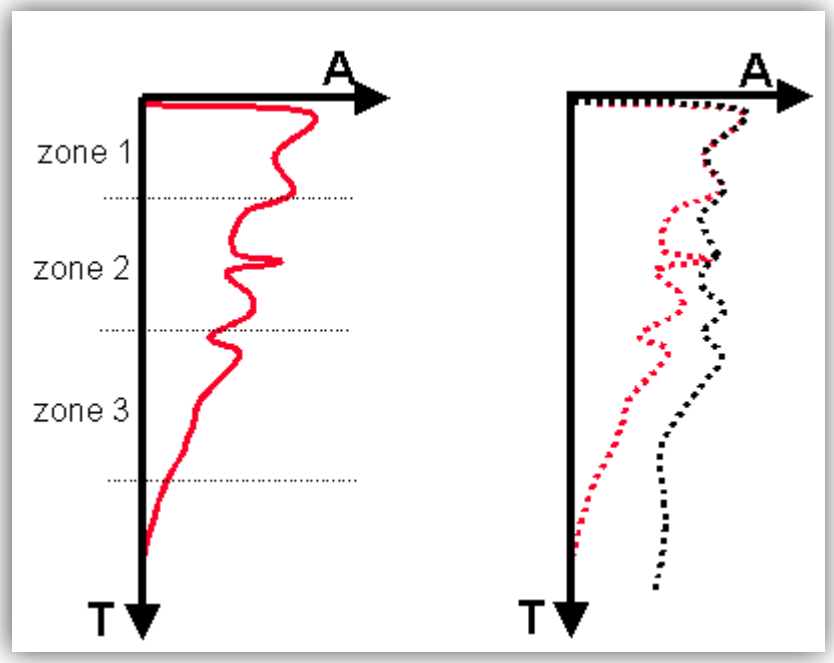

a) Amplitude decay b) After AGC Correction (xsgeo.com)

Figure 5.11; Decay in amplitude of a signal with time (red) and result of AGC (dotted black),

AGC is the most common scaling procedure applied. For a fixed length time window, average amplitudes are calculated in that window. This average amplitude value is compared to a reference value and gain is applied on all the data in that window. The process continues to the later times until whole trace has been gain applied.

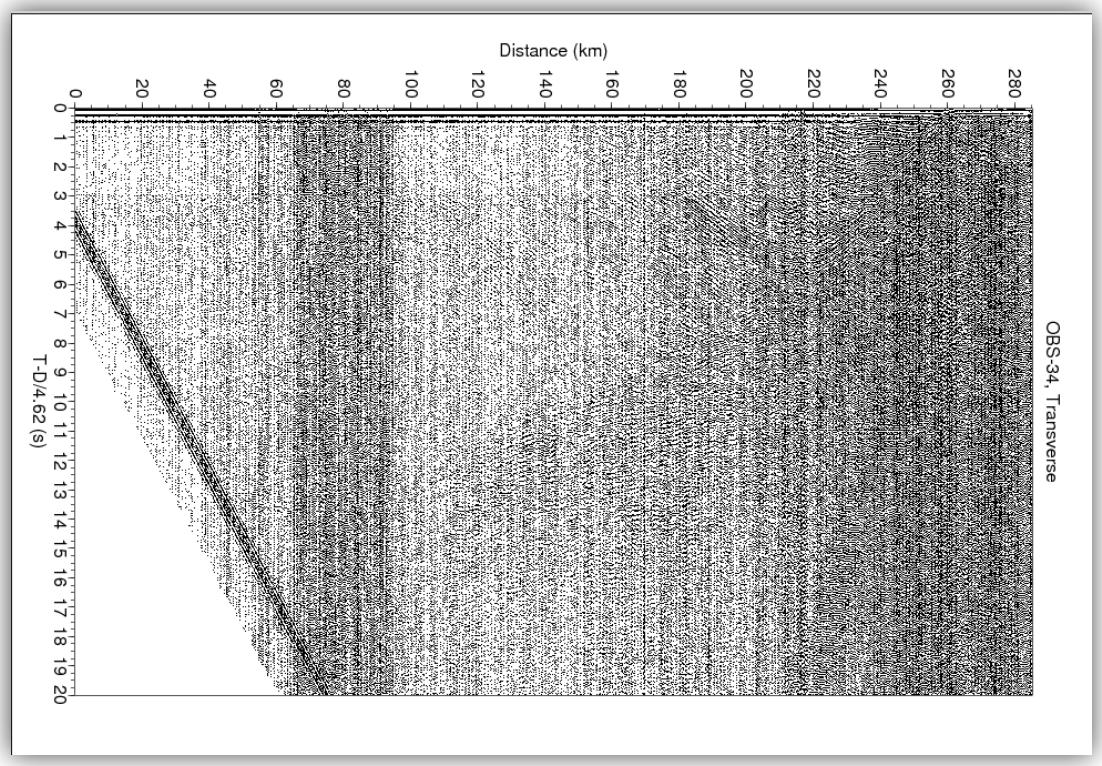

Figure 5.12; *Profile-4, OBS-34, without AGC applied. Note diminishing amplitudes at later arrivals and large offset.*

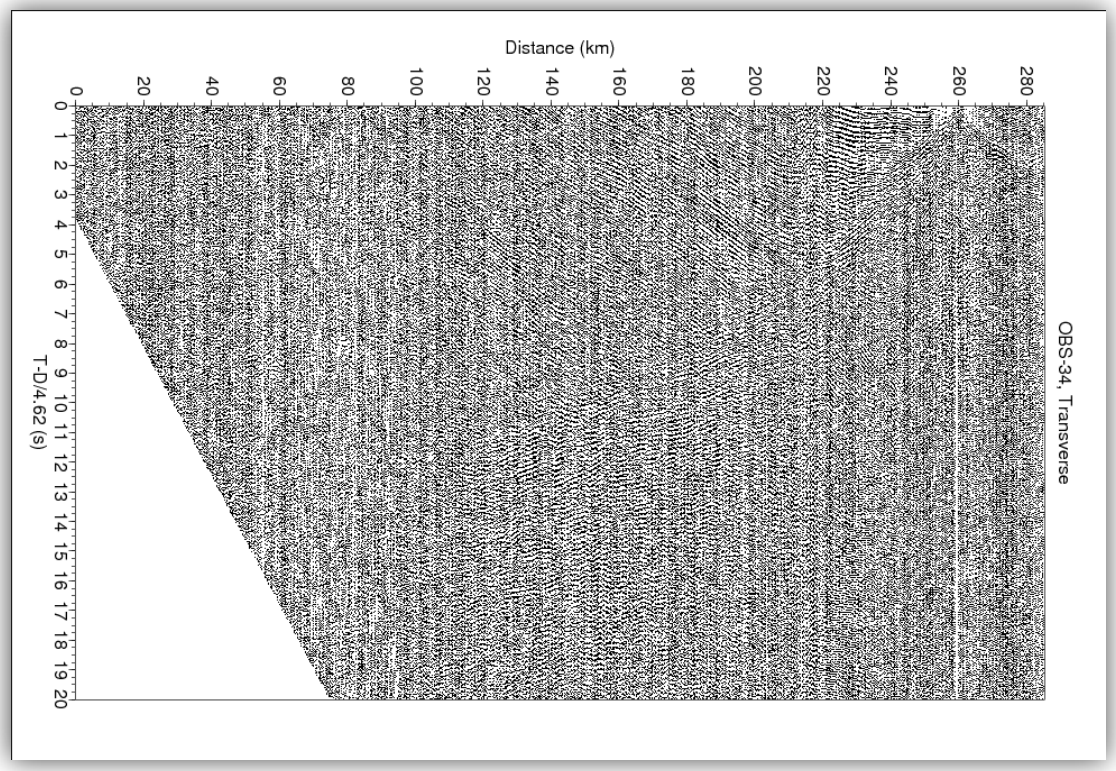

Figure 5.13; *Profile-4, OBS-34, after the application of Gain. Late and far-offset arriving arrivals have been enhanced.*

5.5) Rotation of the Data;

Since 3-C Ocean bottom seismometers sink into ocean as free falling objects, their horizontal components are not oriented into cross-line and in-line directions relative to the source. Their alignment is completely arbitrary. We need to realign them relative to source-centered common orientation (Gaiser, 1998).

Attempt was made to realign all the 3-C OBS's horizontal components parallel and perpendicular to the source-receiver plane. Thus in this way the radial component points towards the source, and will recored particle motion parallel to the source-receiver plane.

It has been observed that seismic signal which consists of reflections, refraction and head waves have source-receiver direction as their main polarization plane. This means that using above rotation scheme; signal should get stronger on radial component and minimum energy should be present on transverse component (Gaiser, 1998).

In order to estimate the angles to rotation for horizontal components information of direct wave travel time information was used. This wave travels direct from shot point to the OBS in the water. Due to poor data quality it is not possible to pick direct wave phases on all the stations. Therefore, another technique was used for such OBS-stations . OBS stations data was rotated for 0^o to 90^o with a successive angle increment of 20^o and was compared for every angle increment. Those angles which gave improved quality relative to un-rotated ones were selected for interpretation. After the rotation scheme first break arrivals showed improved continuity on rotated OBS stations as shown in figure 5.15.

For majority of the seismometers, this scheme worked and resulted in relatively better data quality. In case of land-stations since all of them had the fixed and same azimuthal orientation, therefore, they were angle rotated by determining the azimuth of the profile lines relative to north.

As shown in figure 5.15 below, a significant improvement in S/N ratio can be observed in the OBS-34, radial- Component after the application of rotation angle of 110^O. Although not shown here, signal quality on OBS- 34, Transverse-Component decreases significantly because of concentration of energy in the radial direction.

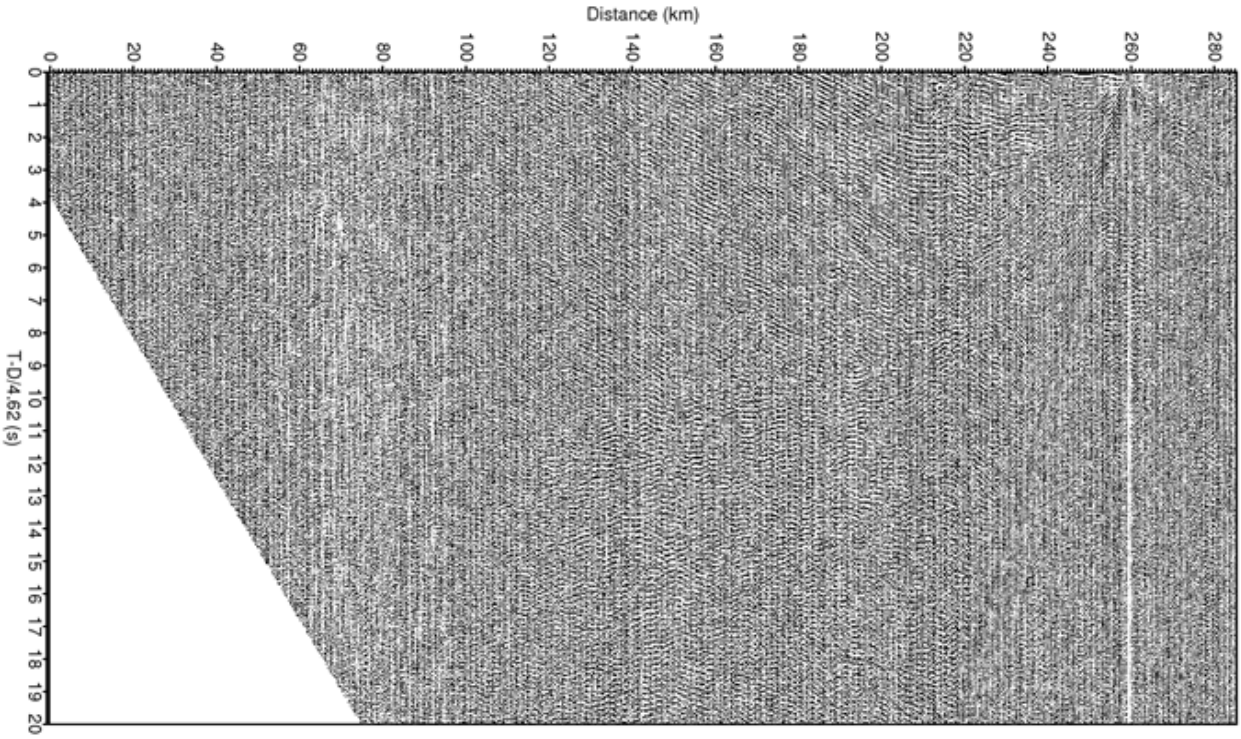

Figure 5.14*; Profile-4, OBS-34, All the above mentioned processing steps applied except rotation.*

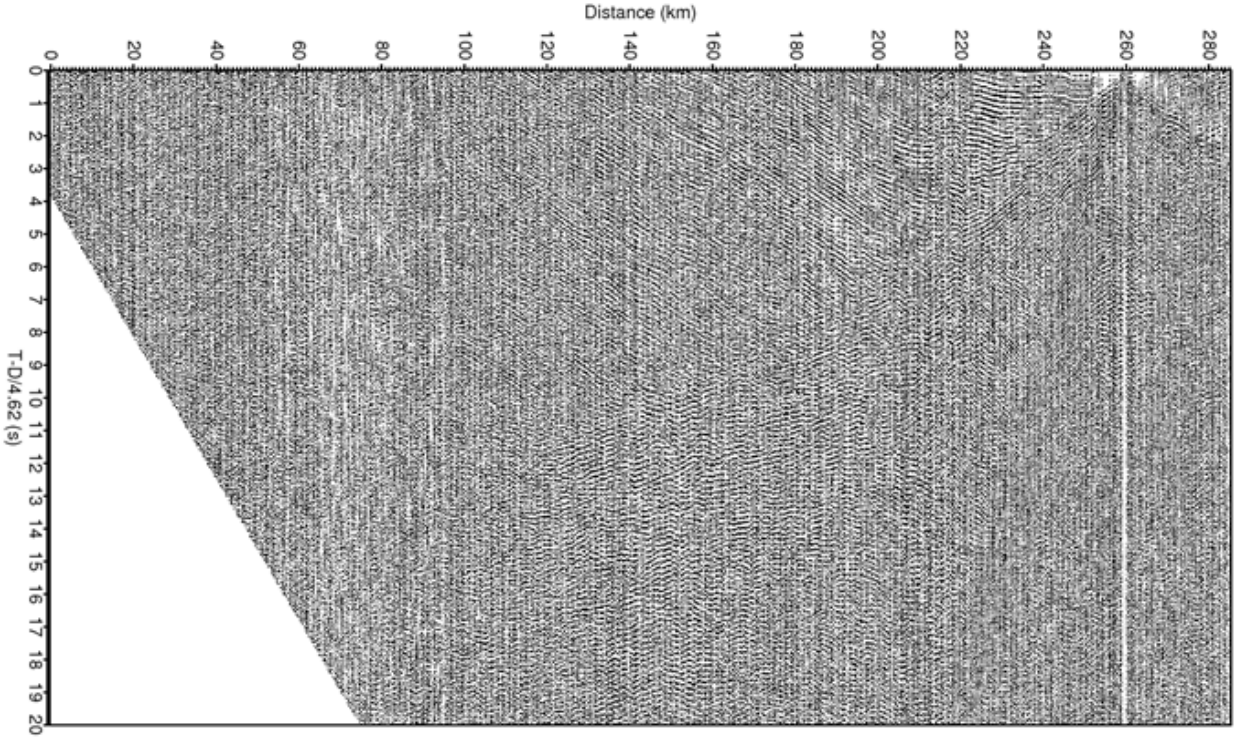

Figure 5.15; *Profile-4, OBS-34 radial, after the application of rotation angle of 110^0. Note the continuity of first arrivals opposed to un-rotated section.*

6) Interpretation and Modeling of data;

After the processing step, converted shear wave phases were identified and modeled on radial components of OBS's of Profile-3-03 and 4-03.

The already generated p-wave models (Breivik et al, 2011) interpreted from vertical component of seismometers were used as a base model for the interpretation and modeling of converted s-waves identified on radial components. Free boundary reflectors interpreted by p-wave data were not included in the modeling scheme as it is not expected to identify weak and localized converted s-waves, originating from them. It was supposed that same p-wave interface represent an s-wave interface.

The same software 'RAYINVR' was used for the s-wave modeling. It requires three parameters for ray-tracing, i.e. conversion boundary, nature of conversion and Poisson ratio. Nature of conversion means whether ray refract, reflect or propagate as head wave.

Although more than two p to s-conversions can be modeled however, energy loss for multiple conversions is great so it is not expected to get strong signal in that case. Therefore, whole of the modeling was limited to only one conversion i.e. from P to S.

As explained in the previous chapter, Poisson ratio specifies the relation between p and s-wave velocities. Once we have provided the correct conversion interfaces and nature of conversion, a suitable value for Poisson ratio should be provided iteratively so that observed and calculated travel times fit each other.

All the OBS arrivals are assigned an uncertainty value for the actual arrival time of any signal and the one interpreted by the interpreter. This value is based upon the confidence in picking the arrivals. Normally, OBS arrivals closer to the OBS location are more certain and are given low uncertainty values. The ease of picking decreases at farther offsets and so does the uncertainty values. In our case since the data quality was already poor therefore uncertainty values in the range of 150 to 250ms were assigned to different arrivals depending upon the confidence in picking the arrivals.

As shown in figure below, various s-wave phases were identified. The whole of the horizontal components has been applied 4.62 km/s reduction velocity to enhance the s-wave arrivals.

6.1) Classification of Arrivals;

Following class of s-wave arrivals were identified,

PPS Arrivals; these kind of arrivals are recorded quite early in time. It is because that seismic energy travels most of its path at high velocity i.e. as p-waves. However, when it reaches to shallower interfaces on its way back to receiver; it is converted from p to s-wave and recorded as an s-wave. As it travels most of its path with higher apparent velocities than the reduction velocity of 4.62 km/s, it has negative slope as shown in figure 6.1 below.

PSS Arrivals; It comprises converted s-wave energy when p-waves are converted to s-waves on their way down in the model. Therefore, it arrives at later times and has a positive slope. SS-wave (Sg) arrivals are a special kind of PSS arrivals. These are identified as s-wave energy which is generated by the conversion of p to s-wave at the ocean-bottom interface on their way down. After this it travels whole of its propagation path as an s-wave. As s-waves travel at lower apparent velocities than p-waves, such arrivals are one of the last to be recorded.

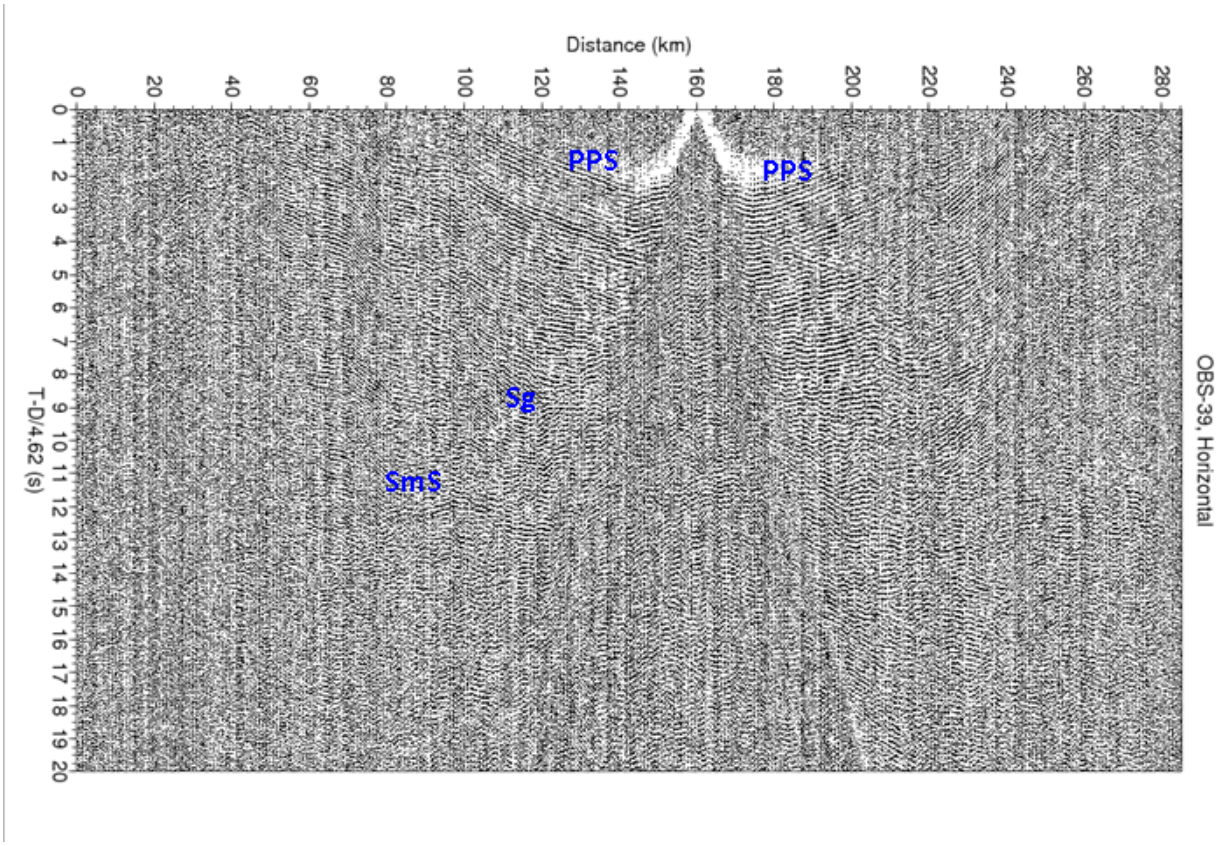

Figure 6.1*; Profile-OBS39, radial, different arrivals highlighted. (Explained in text)*

SmS Arrivals; Such kind of arrivals represent reflected s-waves at Moho. After converting from p to s-waves at ocean-bottom interface, these travel nearly whole of their journey as s-waves.

PSP Arrivals; Such kind of waves start their journey as a p-wave, however, these are converted two times. One from p to s-wave then 2nd time from s to p-wave again. These arrivals are recorded primarily on vertical-components of 3-C seismometers. However, in our case these arrivals were not modeled because due to two conversions, very less energy is recorded on seismometers and were not possible to identify any of it within acceptable uncertainty ranges.

6.2) Interpretation and Modeling of Profile 3-03;

It consisted of twelve ocean-bottom seismometers (OBS-21, 22, 23, 24, 25, 26, 27, 28, 29, 30, and 32) and accompanying five land stations (Land-2, 3, 6, 8, 10). OBS-23 is a hydrophone which record only pressure variations. It was not used for s-wave modeling. Naming convention used for different ray paths is shown in Table#1 below.

TABLE # 1. Naming convention used for ray-tracing.

Ray Code	**Explanation**
PPS*x.y*	Ray travels most of its path as a p-wave.
PSS*x.y*	Ray travels most of its path as s-wave.
SS*x.y*	Conversion from p to s-wave took place at ocean-bottom interface on its way down.
SmS	Reflected s-wave from Moho, with conversion from p to s-wave took place at sea-floor on its way down.
x=	Represents interface at which reflection, refraction or head-wave takes place.
y=	Nature of conversion, 1=refraction, 2=reflection and 3=Head wave

Below is the short description of S/N ratio, interpretation and modeling results of each OBS and Land-Station.

Since the principle objective of this thesis is to determine Vp/Vs ratios for the different parts of the already generated p-wave velocity model, especially for the basement layers. Therefore, S/N ratio is a rather qualitative term used here and is dependent upon how well the different arrivals from each of stations constrain the Vp/Vs values for different parts of the model. A

poor s-wave data quality could be a result of different factors. For e.g. shear waves lose their amplitudes in the crust faster than the p-waves. Masking of shear wave arrivals by scattered p-wave energy and multiple p to s-wave conversions also reduce S/N quality of the shear wave data.

OBS-21; It has a relatively poor data quality with only two identifiable first arrivals interpreted to be s-waves converted at ocean-bottom interface on the way down. Similarly both the arrivals have been modeled to be refracted ones and refraction took place at sediment-basement boundary. Although these travel as s-waves they are recorded relatively early because of their shallow paths.

OBS-22; it also has poor data quality. Only three s-wave arrivals can be seen. The upper two arrivals are refractions from sediment-basement boundary, while the third represent a high velocity reflection from 3rd basement interface. Their positive dips at 4.62 km/sec reduction velocity conform that these are s-wave-arrivals.

OBS-24; Contains relatively good data quality. It provides good constraint on Poisson ratio between sediments and first and second basement velocity layers. Except one, all the s-wave arrivals have been modeled to be reflections and refraction events originating from basement. Since sediment-basement interface has good acoustic contrast, it provides an efficient interface for refractions.

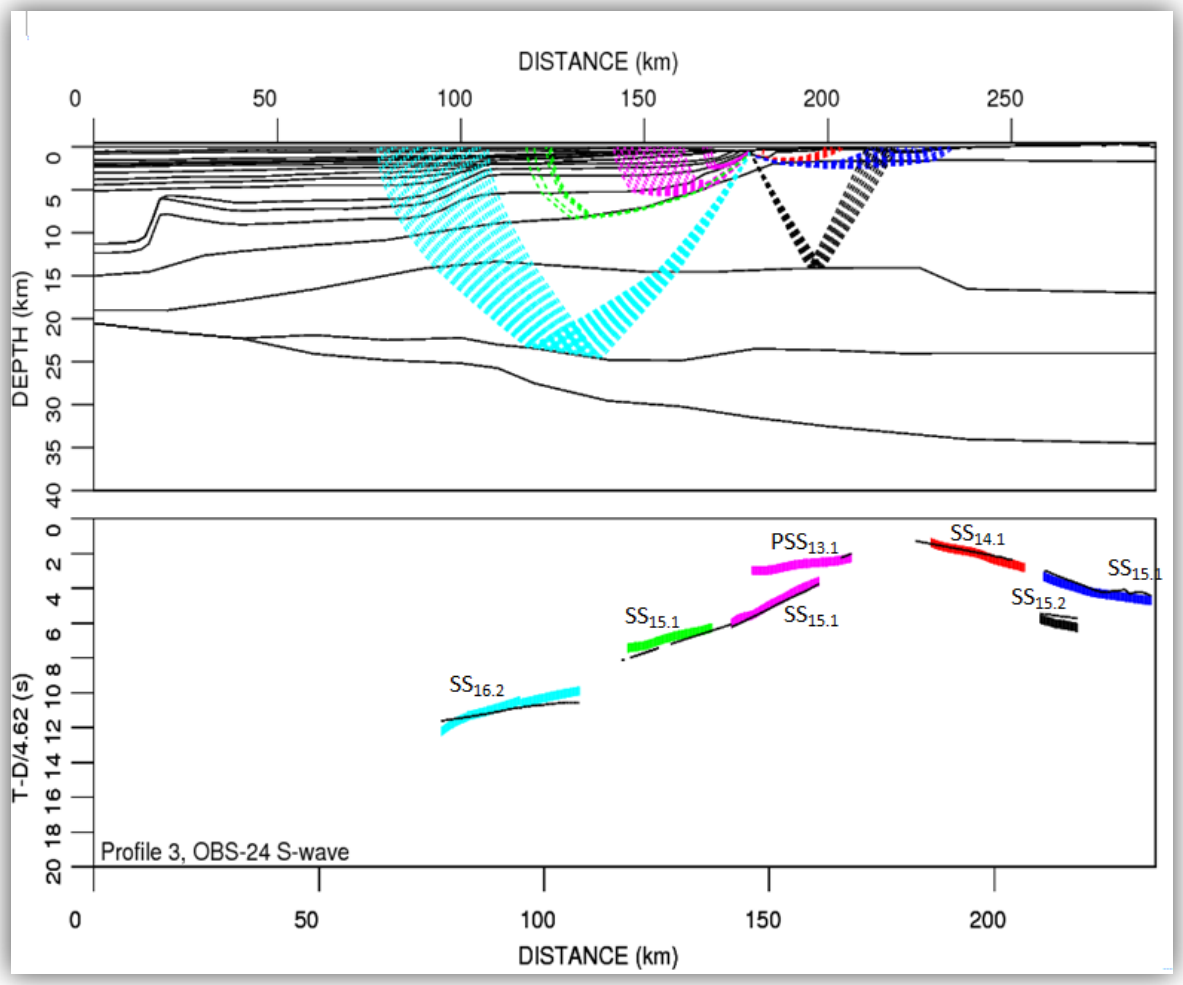

Figure 6.2; *Profile-3, OBS-24. Upper window; traced rays. Lower Window; Bold color lines represent interpreted arrivals while narrow black lines show the calculated arrivals by ray-tracing.*

OBS-25; Data quality is poor, but provides relatively reliable constraint on 3rd basement layer. Four converted s-wave arrivals can be seen. Two arrivals on the right side are head wave from the top-basement while on left are high apparent velocity reflections from 2nd and 3rd basement layer. Sub-horizontal appearance of late arriving signal suggest that they propagated as s-waves deep into crust.

OBS-26; it has quite poor data quality and only two refractions can be identified originating from lower sediment layers. However, it could constrain Poisson ratio for sediments in 120-150 km interval.

OBS-27; All the Arrivals have been interpreted to be originating from top-basement or sedimentary layers above. It doesn't provide any constrain on basement layers, however, it does limit Poisson ratios for overlying sedimentary strata.

OBS-28; it also exhibit quite poor data quality and arrivals can be interpreted with limited continuity. Ray coverage is limited only to the sedimentary strata. Noise level is quite high in this data as compared to other ones probably due to some instrumental problem. Only two PPS and less continuous SS arrivals can be modeled.

OBS-29; Data quality is very poor on this record. Only few arrivals can be interpreted. It may provide constrain on Poisson ratio for sediments between 65-80 km. Although right hand side arrivals don't travel into deep crust, still they arrive late, which is because of most of their travel through sediments at low angles.

OBS-30; Due to quite bad quality data, only two arrivals can be interpreted. Both the arrivals are reflections, one from top of the basement and other from the Moho. Right hand side arrival reflects from top of Moho and they appear as sub-horizontal in the seismic record. This could also provide a good estimated of Vp/Vs ratio in the whole of the crust around 80-110 km offset.

OBS-31; it contains extremely poor data, and only one reflection event arriving from top of Moho could be traced.

OBS-32; only one small reflection from top of basement can be traced. It could provide constraints on Poisson ratio for upper sedimentary strata between 30-50 km.

Land station-2; although the data quality is poor on it, however, it still can constrain first and second basement layers. Therefore, it provides good constraints on Poisson ratio for these layers. All the three arrivals are p to s-converted at above mentioned layer boundaries. Near-horizontal appearance of late arriving PPS suggest they travelled as p-wave for most of their journey.

Land station-3; since Land-2 and Land-3 are located very close to each other, it exhibits nearly the same arrivals as on Land-2 in terms of converting interfaces.

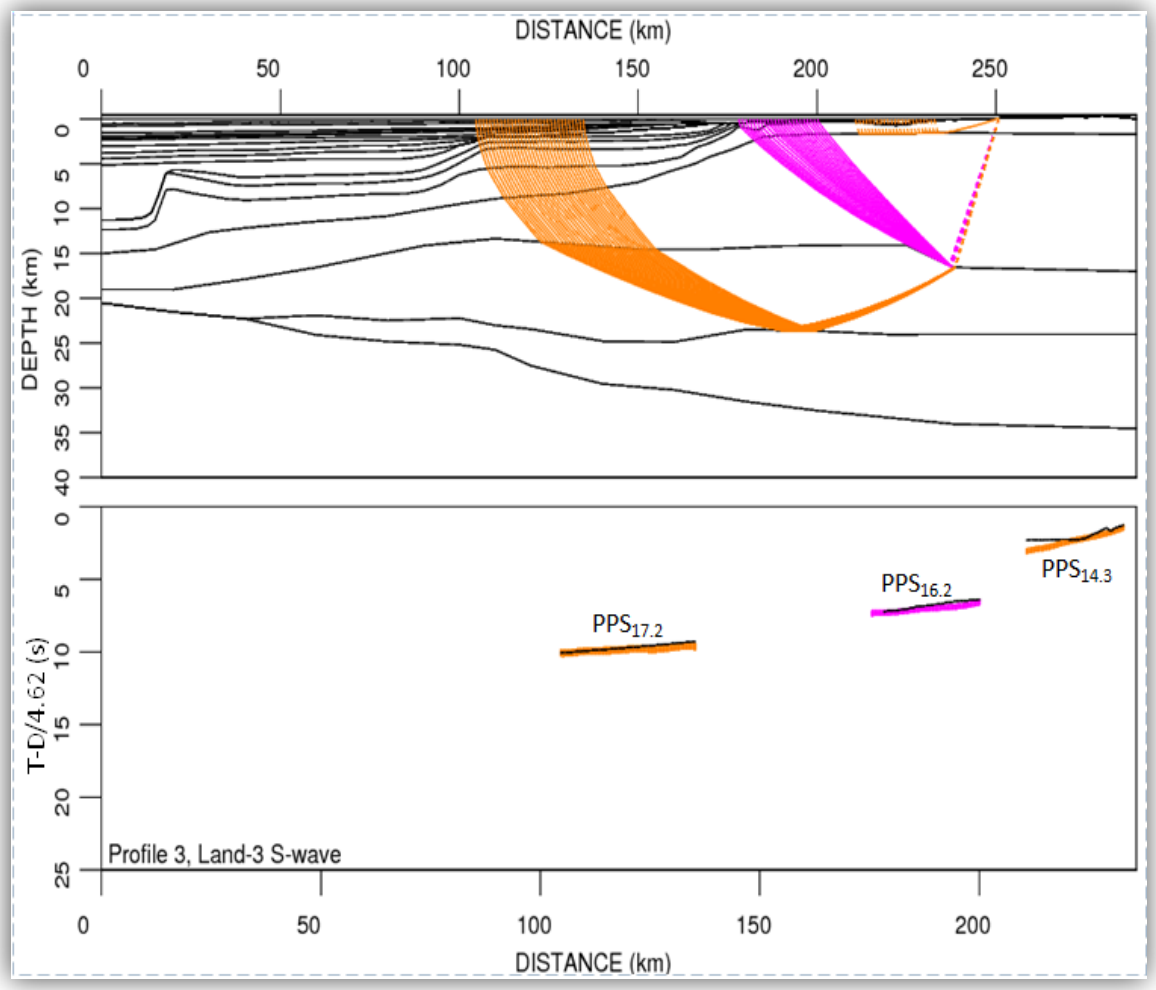

Figure 6.3; *Profile-3, L. Station-3. Upper window; traced rays. Lower Window; Bold color lines represent interpreted arrivals while narrow black lines show the calculated arrivals by ray-tracing.*

Land-6 and 8; due to their closeness, the same kind of arrivals can be seen on them. Both have only two refracted p to s-arrivals each, where conversion takes place at first and second basement layers. Land stations provide quite good constrains on Poisson ratios for upper three crustal layers between 200-280 kms.

Land-10; this station contains only one near offset head wave trapped in first basement layer.

6.3) Interpretation and Modeling of Profile 4-03;

This profile consists of eleven 3-C OBS (OBS-33, 34, 35, 37, 38, 39, 40, 42, 45 and 46) and six 3-C Land Stations (L-1, 2, 4, 5, 7 and 9). OBS-37 contained very poor data quality so was not used for modeling of shear waves, and OBS-40 and L-4 contained very small amount of

data and it was not possible to perform any meaningful interpretation using them, so they were skipped as well. The same naming convention given in Table#1 is used.

Below is the S/N ratio, interpretational and modeling summary of each of the stations.

OBS-33; Although, only three converted s-wave arrivals can be picked on it, still it successfully constrain the first, second and fourth basement layer. All the three phases convert on the ocean-bottom interface on their way down. Calculated reflection event from top of Moho is in good agreement with the interpreted ones.

OBS-34; it exhibits almost the same behavior as the OBS-33. All the three interpreted arrivals are p to s-converted at ocean-bottom interface on their way down.

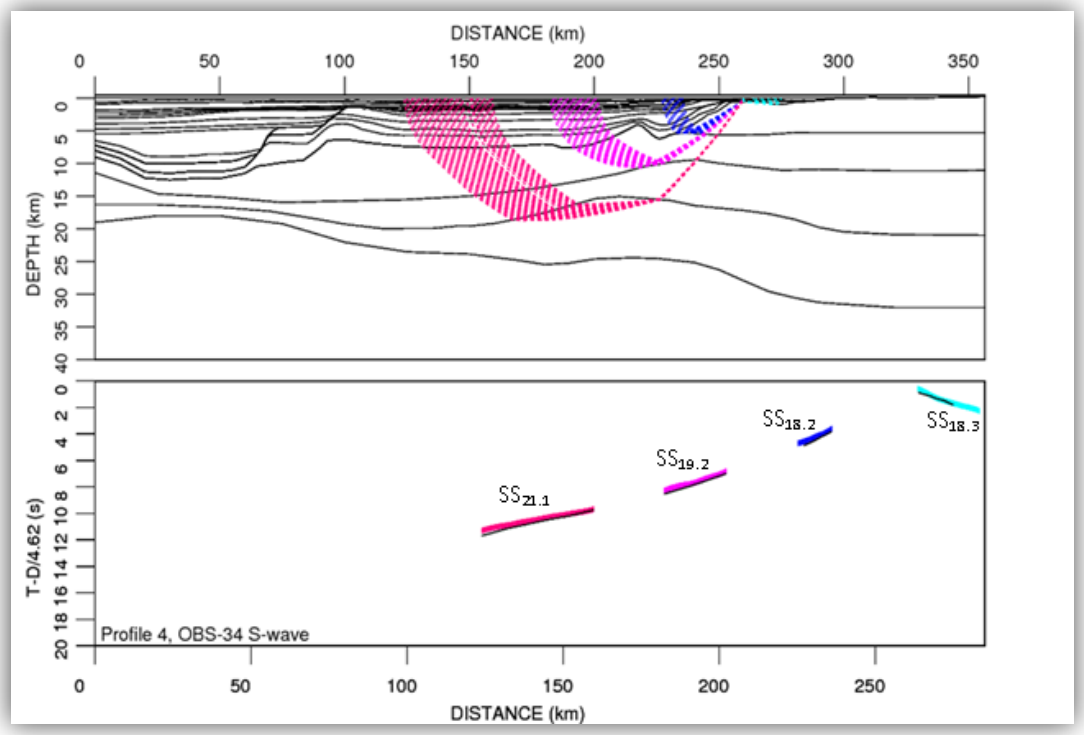

Figure 6.4; *Profile-4, OBS-34. Upper window; traced rays. Lower Window; Bold color lines represent interpreted arrivals while narrow black lines show the calculated arrivals by ray-tracing.*

OBS-35; the arrivals can be interpreted as converted s-waves and conversion took place on the ocean-bottom interface on their way down. On the left side, converted s-wave has been modeled to be reflecting from Moho while right side represent reflections from first and second basement layers, respectively.

OBS-39; two PPS refractions can be identified on it. Their negative slopes and early arrivals indicate that they travelled most of their journey as p-waves. However, two PSS arrivals can also be identified reflecting from Moho.

OBS42; although it contains poor data quality; however it can serve as a guide for aggregated Poisson ratio for all the basement layers. Because, it contains two refracted PSS arrivals from top of mantle and one refracted PSS arrivals from sediment-basement interface.

OBS45; in spite of bad data quality, four PSS arrivals can be interpreted. Again these arrivals constrain Poisson ratio for whole basement and partially its layers as well. All of these have been modeled to be reflections from different basement layers.

OBS46; it is the last OBS sea-ward. It contains poor data quality with no arrivals at large offset and later times. Only one head wave constraining upper sedimentary cover and two reflections from first and second basement layers can be modeled.

Land-1; it has quite poor quality data and only one short-offset arrival can be identified and has been modeled as PSS wave reflecting from second basement velocity layer. Data is quite noisy so it is not possible to model long offset arrivals with confidence.

Land-2; this station is the further continuation of land stations. Three reflections can be interpreted with confidence. All the three arrivals are PPS reflections. Two of them are reflecting from Moho and one reflects from 3rd basement layer. However, these rays convert from P to S at 1st, 3rd and fourth basement layer on their way up and provide a good relative constrain on Poisson ratio for basement layers in 330-356 km.

Land-5; signal quality is quite poor and only two reflected PPS arrivals can be interpreted. One is reflected as 3rd basement layer while the other one is from Moho. As p to s conversion is taking place at 1st and 3rd basement layer, so an approximate estimate of Poisson ratios for basement layers can be made for this offset range.

Land-7; L-5 and L-7 contain almost the same kind of events with same resolution. Due to their closeness, traced rays follow approximately same path and are recorded at the same approximate time. Similar case is with the S/N ratio, which is also bad.

Land-9; it shows up with slightly better data than the L-7 with one additional reflected converted PSS wave, where conversion took place at Moho. So, it provides a good approximation of Vp/Vs ratios for basement layers.

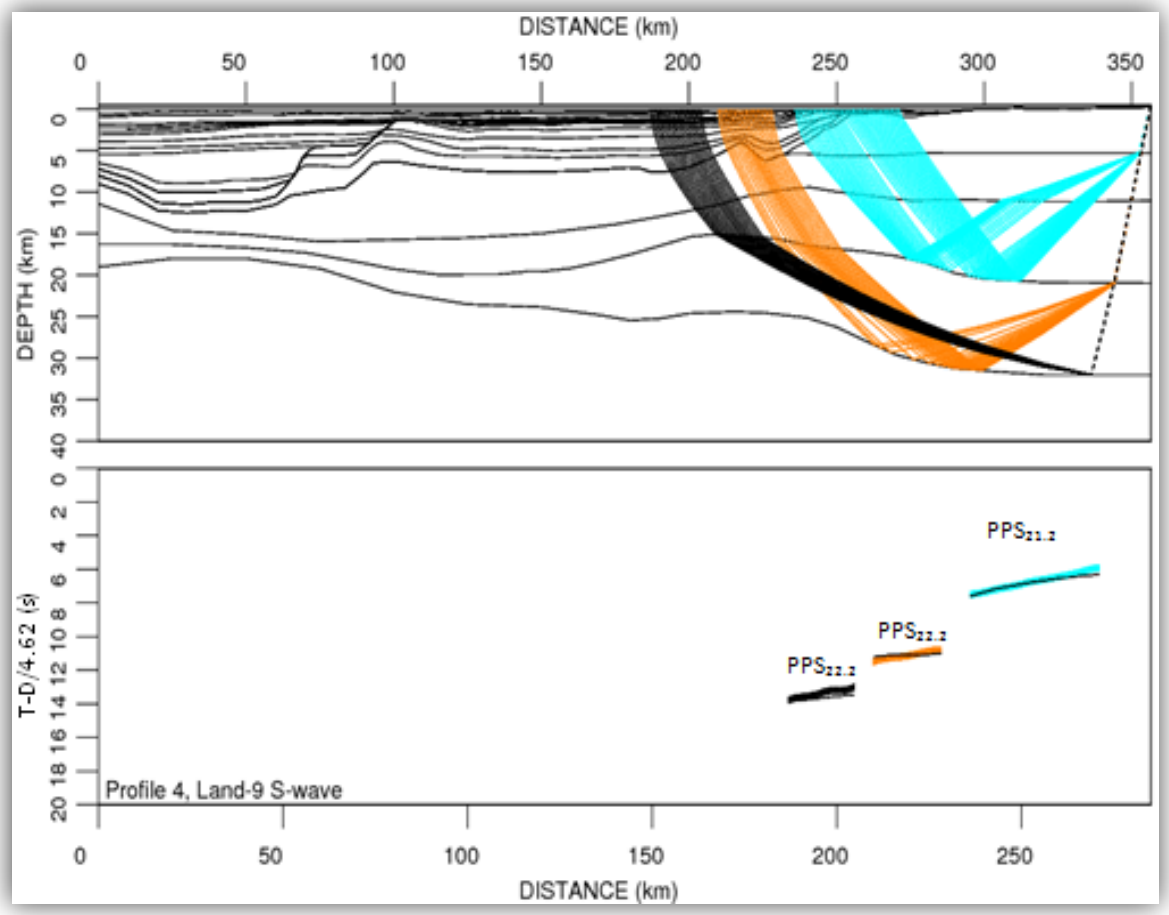

Figure 6.5; *Profile 4, Land Station - 9. Upper window; traced rays. Lower Window; Bold color lines represent interpreted arrivals while narrow black lines show the calculated arrivals by ray-tracing.*

6.4) Interpretational Uncertainties;

As discussed in section 4.3, it is standard practice to show the uncertainties between observed and calculated travel times at the end of modeling for reference.

TABLE # 2; RMS (s) and Chi-squared (χ^2) values for different velocity layers.			
PROFILE-3-03	NPTS	RMS (second)	Normalized χ^2
Sediments	1007	0.31	1.221
Basement Layers	2946	0.37	1.315
Moho	283	0.32	1.547
Average	--------	0.33	1.361
PROFILE-4-03	NPTS	RMS (second)	Normalized χ^2
Sediments	242	0.37	1.984

Basement Layers	1166	0.275	1.154
Moho	1415	0.20	0.622
Average	--------	0,28	1.253

6.5) Conversion Efficiency and Statistics;

Seismic energy is generated as a pure compressional wave by a seismic source (air-gun) in water and s-waves can't propagate through water. However, the observed shear waves in seismic data are generated as a result of conversion of p-waves energy from different interfaces in the subsurface. The percentage of conversion of p-waves to s-waves depends upon angle of incident of p-waves and acoustic impedance contrast across the interface. Therefore, the greater the acoustic impedance contrast greater will be the conversion efficiency. This concept has been discussed in detail in section 3.2.2 and 3.2.3.

Conversion statistics show two interesting results. It has been observed that about 85-90% of s-wave arrivals recorded at ocean bottom seismometers (OBS) are PSS or SS. i.e. p-wave is being converted to s-wave at very shallow depths i.e. 1st or 2nd layer. Then, this converted s-wave propagates the whole of its journey as s-wave. It is verified by their positive slopes and later arrival. However, only 10-15% of the converted s-wave arrivals can be classified as PPS arrivals. These are recorded quite early in time and have negative slopes.

In case of Land-stations, on both profiles, this situation is almost reverse. Statistics show that about 95% of the recorded s-wave signals are PPS arrivals. Except some complex head waves in the upper most basement layer, almost all the conversions from P to S-wave are being taking place at the various basement layers. In fact no PSS arrival, converting from upper sedimentary layers or even sediment-basement interface could be interpreted or modeled.

Above observations can be explained using theoretical concepts dealing conversion of seismic waves and their subsequent energy.

In case of ocean bottom seismometers, most of the P-wave and PPS-wave arrivals don't lag from each other so much. It is probably because of the geometry of the underlying strata. Most of the shallow sedimentary layers are quite thin; therefore, a potential PPS conversion at them should not delay the arrivals so much. Secondly, the energy of the converted s-wave is dependent upon the angle of incidence of the p-wave therefore, short to mid-offset incidence angles result in lower s-wave amplitudes, causing low visibility in already poor quality data.

Abundance of PPS arrivals on land stations could also be explained. As land stations lie further SE from the last shot point, so already weaker PSS arrivals from far-offset shot points loose more amplitude upon reaching them. While most of the PSS energy generated by near-offset shot points between OBS-33 and 36, a very narrow part of the wave-front gets converted into head wave and it is trapped as head wave inside the 1st shallow basement layer. Thus preventing any PSS energy to travel down. However, situation for PPS energy is different here, although, it still gets trapped inside 1st basement layer for shorter offsets. However, for mid to large offsets, it travels most of its path in high velocity basement layers. Therefore, it doesn't lose energy quickly. When it is incident on basement layers from below, high acoustic contrast serves as a perfect conversion interface. Similarly, in spite of travelling in large vertical distance in basement layers, this energy is still detectable because of non-dispersive nature of high-velocity basement layers.

This assumption could also be supported by the fact that PPS arrivals on OBS's have negative slope in 4.62 km/sec reduced seismic section, while PPS arrivals on Land-stations have positive slope and are near-horizontal. Reason is that as PPS energy travel as p-wave most of its path it tends to be recorded earlier, so should have negative slope. However, when this PPS energy is converted to s-waves at one of the much thicker basement layers on their way up; its slope tends to bend in positive manner because of the significant travel time as s-wave in thicker basement layers. Thus, in spite of the fact that these PPS arrivals travel most of their travel path at p-wave, their conversion to s-wave at much thicker basement layers results in their positive slopes due to increased travel times.

6.6) Modelling Results;

After tracing rays on all the OBS and land stations using already generated p-wave models, the Vp/Vs ratios were calculated to that part of the model, where ray-coverage provided good constrain on them.

S-wave velocities (Vs) are dependent upon Poisson ratios and p-wave velocities. Therefore, using p-wave model velocities and provided Poisson ratios, Vs can be calculated and so are the Vp/Vs ratios.

As s-wave ray coverage is poor, it is suitable to denote Vp/Vs ratios on already generated p-wave models rather than building s-wave velocity models, as shown in figures 6.6 and 6.7 below.

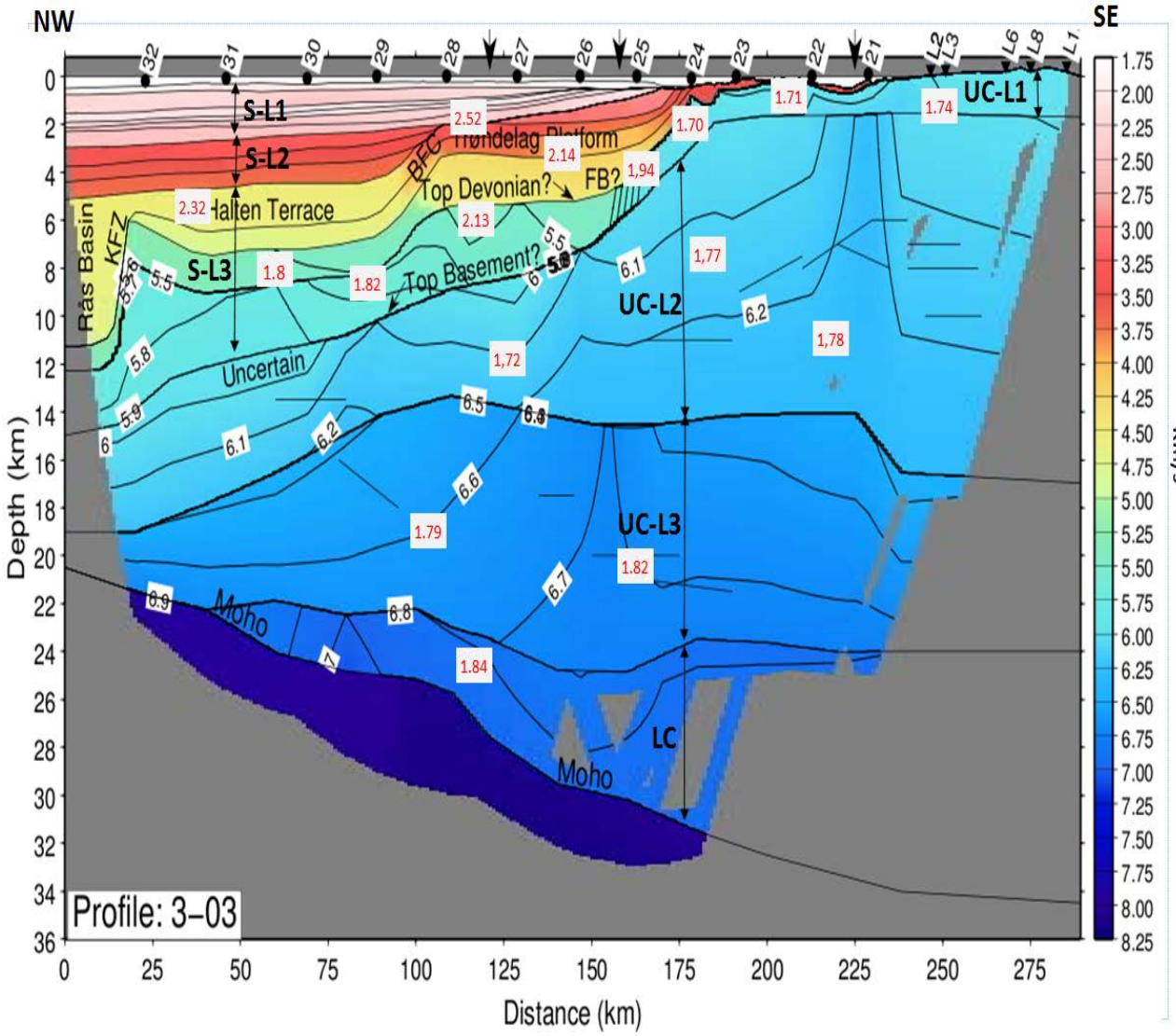

Figure 6.6; *Profile 3-03 P-wave velocity model. Observed Vp/Vs ratios are shown in red-colour. 'S-L1' sediment layer-1, 'S-L2' sediment layer-2, 'S-L3' sediment layer-3, 'UC-L1' upper crustal layer-1, 'UC-L2' upper crustal layer-2, 'UC-L3' upper crustal layer-3, 'LC', lower crust (modified from Breivik et al., 2011)*

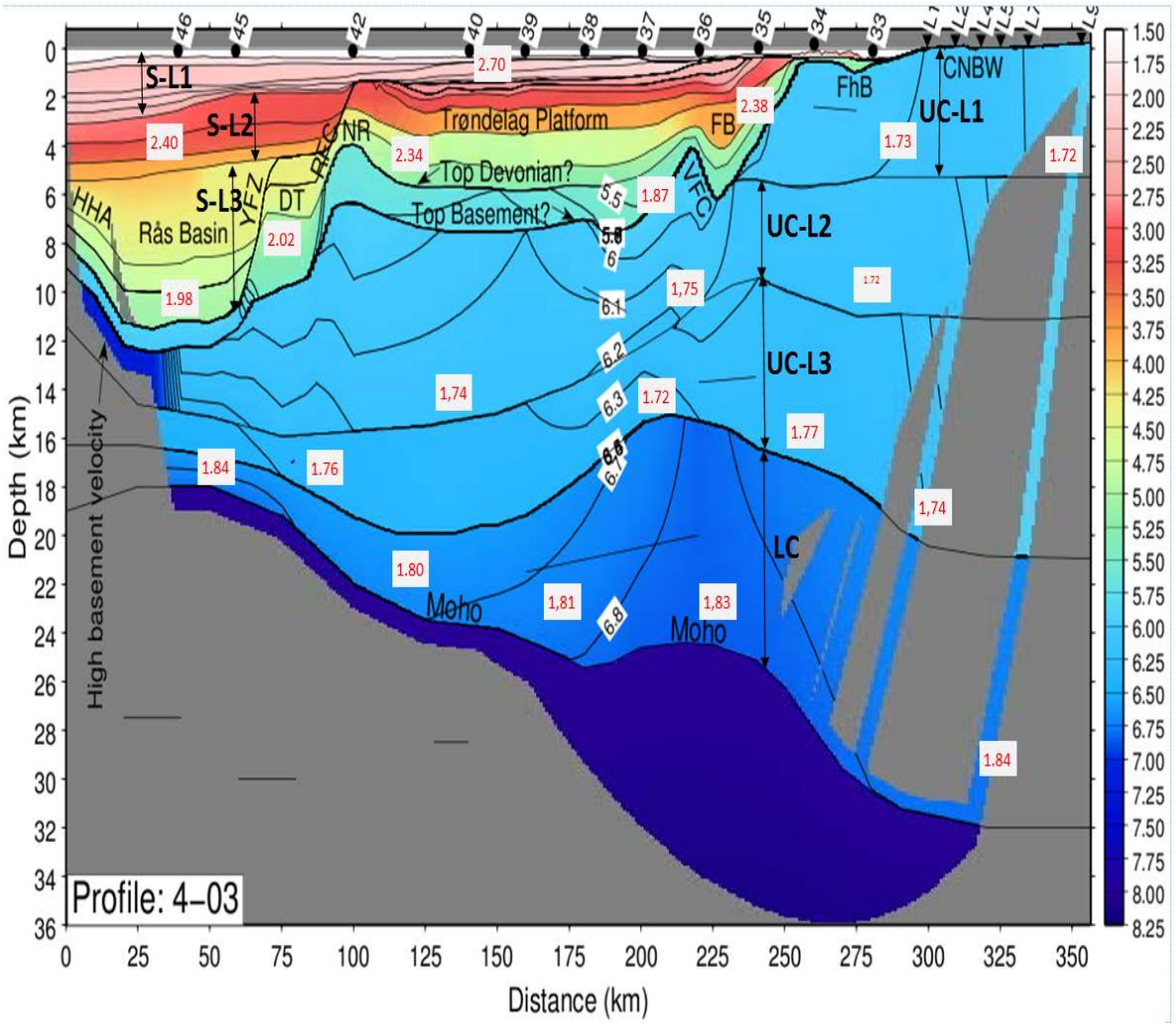

Figure 6.7; *Profile 3-03 P-wave velocity model. Observed Vp/Vs ratios are shown in red-colour. 'S-L1' sediment layer-1, 'S-L2' sediment layer-2, 'S-L3' sediment layer-3, 'UC-L1' upper crustal layer-1, 'UC-L2' upper crustal layer-2, 'UC-L3' upper crustal layer-3, 'LC', lower crust (modified from Breivik et al., 2011)*

7) Discussion on Results;

Numerous studies show that a good agreement exists between Vp/Vs ratios and subsurface lithology. (e.g. Picett, 1963; Domenico, 1984; Tatham, 1985; Tatham and McCormac, 1991). Limestones and sandstones show a low range of Vp/Vs ratio i.e. (1.6-1.75) and (1.84-1.99) respectively. However, shales are associated with higher Vp/Vs values i.e. 1.70-3.0 (Domenico, 1984). However, above mentioned measurements are very much sensitive to nature of pore fluid, porosity, its shape and consolidation degree and may vary drastically upon changing these parameters (Tatham, 1985; Tatham and McCormac, 1991). For example it has been observed that Vp/Vs ratios could extend upto 10.0 to 16.0 in less consolidated sediments up to to 50 m below the sea bottom in the Norwegian Sea (Whitmarsh and Miles, 1990). These high values are related to low degree of compaction in sediments (e.g. Chung et al., 1990; Bromirski et al., 1992). Vp/Vs ratios could be very low in gas filled sandstones i.e. < 1.60, because low p-wave velocities in such sediments.

7.1) Vp/Vs ratio for the sedimentary layers;

In both profiles the sediment p-wave velocity layering can be divided into 3-distant categories. The shallower upper layer represented by 2-2.5 km/s p-wave velocities while second sediment layer can be classified by 3-3.5 km/s p-wave velocity range. Similarly, third layer with p-wave velocities around 4-5.5 km/sec is shown in the figures 6.6 and 6.7. Velocity coloring distinguishes them as light pink (1st layer), red (2nd layer) and yellow to green (3rd).

Layer-1;

Due to poor data quality only few arrivals have been interpreted to be constraining Vp/Vs in this layer and therefore, further resolution is not possible. Average Vp/Vs in this layer is calculated to be 2.50 along Profile-3 while 2.70 along Profile-4. Variation in these values along both the profiles can't be calculated due to limited arrivals, so these Vp/Vs ratios have been considered as the representative values for this layer.

The relatively high values of Vp/Vs observed are due to poor consolidation of sediments just below the sea bed. The same trend has been observed by several other studies as well. P. Digranes et al., 1998 have reported a Vp/Vs value of 2.2-2.4 for the same sediment layer (0-3 km depths) just adjacent to our study area further NW. As the layer thickens to the NW, slightly lower values could be because of increasing compaction further NW as compared to our area. As our Vp/Vs values (=2.5 and 2.7) have been calculated near OBS-28 and OBS-39

in Profile-3 and 4, therefore it is very much likely that Vp/Vs values decrease to 2.2-2.4 to NW for this layer. Similarly as Vp/Vs ratios of 3.0 to 5.50 has also been observed in shallow sediments in Lofoten Continental Margin further north (Kodaira et al, 1996).

Layer-2;

Vp/Vs of 2.40 have been calculated for this layer on Profile 4 close to NW end of the profile. However this layer is not constrained by arrivals on profile 3. Comparative studies for the same depths (3-5 km) show an average value of Vp/Vs=2.3 close to Profile-4 and a value of 2.1 close to Profile-3 further NW (Digranes et al, 1998). Therefore, approximately 2.1 or 2.2 Vp/Vs value range can be expected for this layer under Profile-3. However, it should be noted that values represented by Digranes et al, 1998 are average Vp/Vs values along the whole length (average length=120 km) of their profiles just further NW from our profiles.

Layer-3;

This layer is present between upper reddish layer and lower top-basement, roughly on both the profiles. Moderate lateral velocity variations exist in this layer and hence the Vp/Vs ratios.

Profile-3 covers only a portion of Rås Basin and no s-wave arrivals can be mapped from this basin. However, Profile-4 shows s-wave arrivals under the Rås Basin at about 10-11 km depth. Since sediment Layer-2 has 2.4 Vp/Vs, so this layer is constrained by Vp/Vs of 1.98. No comparison can be made further NW because; Rås Basin is localized only in this area. It is interesting to note that a Vp/Vs of 1.75 is noted immediately further NW from Profile-4 for the same depths. It is because that Rås Basin is a localized deep basin and represents low-velocity sediments present at greater depth. However, this trend terminates further NW and is replaced by upper basement layer with lower Vp/Vs ratios. Therefore, Vp/Vs ratio of 1.98 in Rås Basin is reasonable because of the sedimentary fill. Depth to top basement is uncertain along both the profiles. Therefore lower boundaries for the sediment layers can’t be marked with full certainty.

Similarly as we move NW to SE between 3rd sedimentary layer and top basement another interesting thing is observed. Along Profile-3, Vp/Vs for 3rd sediment layer have been averaged to be 1.81 under OBS-29, however towards SE direction, this value changes to 2.13. Roughly same trend is observed under Profile-4 where Vp/Vs of 1.98 under Rås Basin changes to 2.02 under the Dønna terrace with further increase to 2.34 as we move more

towards the SE direction. It could be justified by the fact that decreasing burial depths causes metamorphic grades getting lower, thus increasing Vp/Vs.

Central Norway Basement window (CNBW) is exposed along the S-eastern tip of Profiles. A significant decrease in p-wave velocities is observed under OBS25 and 26 along Profile-3. Breivik et al, 2011 concluded that it could represent a Devonian detachment transporting Devonian strata to NW. From here on top basement lies under Devonian strata. This assumption could be supported by sharp Vp/Vs changes along this transition. Being 1.70 SE and 1.94 towards the NW side i.e. transition from lower Poisson ratio to higher indicate change of lithology.

7.2) Vp/Vs ratio for basement and Moho;

Profile-3 and 4 show that basement is heterogeneous and is composed of different distinctive velocity layers (Breivik et al, 2011). For interpretational purpose we can name it as Upper and lower crust. Upper crust is further classified into three distinctive layers i.e. Layer-1, 2, and 3 as shown in figures 6.6 and 6.7.

Upper Crust;

Upper crustal Layer-1 is exposed on the SE side of both profiles as CNBW. However, after OBS-35 on P-rofile 4 and OBS-25 on Profile-3, Devonian detachment results in placement of Devonian strata on it. From here, only two upper crustal layers can be identified (Breivik et al. 2011).

Upper Crust along with lower crust represents dominant p to s-conversion interfaces and most of the arrivals which travel to land stations from NW to SE direction are being converted at upper crustal level.

Its layer-1 (CNBW) present on SE side has an average Vp/Vs ratio of 1.72 on both of the profiles. Its 2nd and 3rd layers which extend all along both profiles have average Vp/Vs of 1.76 on Profile-4. Studies adjacent to our profiles in NW direction suggest Vp/Vs=1.75 for these layers (P. Digranes et al. 1998). Similarly, values obtained under Profile-4 are also in agreement with those measured further north in Lofoten area i.e. 1.73 (Mjelde and Sellevoll, 1993). Holbrook et al, 1992 concluded that average Vp/Vs values in continental crust are close to 1.73. By keeping in view the uncertainty associated with the picks i.e. 150-200ms, it can be concluded that Vp/Vs ratio of 1.76 agrees with this on Profile-3 and 4.

Similarly Vp/Vs measured for upper crust along Profile-3 does show deviation from what measured along Profile-4. Profile-4 does not have so much lateral and vertical velocity variations in the upper crust as compared to Profile-3. Therefore, Vp/Vs show more variations along Profile-3 for this layer. P-wave velocities are higher in Layer-3 than in Layer-2 under Profile-3 as compared to velocities under Profile-4 which have comparable velocities in both layers. Layer-2 shows variation of Vp/Vs to 1.72 at NW to 1.78 towards SE. Similarly, Layer-3 also shows the same trend having 1.79 values of Vp/Vs on right side and 1.82 to the left. The average Vp/Vs values measured adjacent to the Profile-3 further NW differ slightly, i.e. 1.75.

Lower-crust;

Along Profile-4 Vp/Vs of 1.83 is observed at the top of bulge in Moho under OBS-35. It varies slightly to 1.80 under OBS-39 and 1.84 under OBS-45. Therefore, Vp/Vs of 1.82 represent average value for lower crust. Studies close to Profile-4 in NW-direction do show Vp/Vs of 1.80 for the lower crust (P. Digranes et al. 1998). Similarly, It is evident that Vp/Vs for lower crust are significantly higher than the 1.75 in upper crust.

Laboratory measurements of oceanic basalts show a Vp/Vs ratio of 1.86-2.04 (Hamilton, 1979) while measurement on gabbro indicated a Vp/Vs ratio of 1.77-1.90 (Holbrook et al, 1992). Upper, middle and lower oceanic crustal measurements at the Lofoten margin reveal Vp/Vs ratios of 1.86, 1.76 and 1.80 respectively (Kodaira et al, 1996). A Vp/Vs ratio close to 1.90 has been calculated at the continent-ocean transition in the same area (Mjelde et al, 1996b). Similarly Vp/Vs ratio of 1.88 has also been calculated at the Green-margin (Chian and Louden, 1994).

The lower crust in the outer Vøring area has been supposed to be magmatic under-plated body which was created before the opening of Norway and Greenland, source to which was Iceland hot spot as discussed by Skogseid et al, 1992 and Eldholm and Grue, 1994. However, in our case no evidence of magmatic under-plating can be found.

7.3) Lithological Interpretation;

Profile-4

For Profile-4, along the three upper crustal layers the average Vp, Vp/Vs and σ values are presented below,

Upper-crust, Layer-1; Vp=6.03 km/s, Vp/Vs=1.72 and σ=0.245

Upper-crust, Layer-2; Vp=6.15 km/s, Vp/Vs=1.73 and σ=0.250

Upper-crust, Layer-3; Vp=6.28 km/s, Vp/Vs=1.747 and σ=0.26

The ranges in Vp, Vp/Vs and σ suggest that composition of upper crust to be Granitic (Birch, 1961, Holbrook et, al, 1987 Holbrook et al, 1988, Christensen, 1988). It is difficult to estimate the exact mineralogical composition responsible for Poisson ratios for the layers. However, average 0.255 Poisson ratio value show higher quartz content in the upper crust. Similarly slight increase in Poisson ratio with depth represent decreasing quartz content in the upper basement layers.

For lower crust the value for different parameters are Vp=6.7-6.8 km/s, Vp/Vs=1.82 and σ=0.285-0.29. Therefore an increase in Poisson ratio is observed from the upper crust to the lower one. This increase is probably attributed to the more quartz-poor mafic composition of the lower crust. Granulite rocks represent the most favorable candidate for the lower crust. These might include intermediate-mafic to mafic rocks i.e. anorthosite, pyroxene and hornblende Granulitic facies. However, it is difficult to state about the exact lithology of the lower crust (Holbrook et, al, 1987 Holbrook et al, 1988, Christensen, 1988)

Similarly, lateral variations in Poisson ratio are also observed in the lower crust. For e.g. under OBS-36 different parameters are, Vp=6.82 km/s, Vp/Vs=1.83 and σ=0.29 while for OBS-40 above values are Vp=6.7 km/s, Vp/Vs=1.80 and σ=0.275. Probably, such lateral changes are probably related to changes in quartz content. Poisson values σ=0.275 show more quartz content (>10%) than σ=0.29 as discussed by Holbrook et, al, 1987 Holbrook et al, 1988.

Profile-3

For Profile-3, along the three upper crustal layers the average Vp, Vp/Vs and σ values are given below,

Upper-crust, Layer-1; Vp=5.90 km/s, Vp/Vs=1.73 and σ=0.25

Upper-crust, Layer-2; Vp=6.28 km/s, Vp/Vs=1.74 and σ=0.267

Upper-crust, Layer-3; Vp=6.62 km/s, Vp/Vs=1.80 and σ=0.273

Similar to Profile-4, the range of above parameters show that Upper-crust is composed of quartz-rich Granitic rocks under Profile-3. However, here the average σ values for crustal layers are bit higher than for the Profile-4. It probably suggests slightly more quartz rich granitic rocks under Profile-3 as compared to Profile-4. Just like Profile-4 decreasing quartz content is observed in the successively deeper upper-crustal layers. This decrease is shown by increasing average Poisson ratio values for deeper layers.

In case of lower crust the seismic parameters derived are,

Lower-crust; Vp=6.94 km/s, Vp/Vs=1.84 and σ=0.285.

Along Profile-3 lower crust is thinner as compared to Profile-4. The Poisson value of 0.285 shows that it has similar composition like the lower-crust along Profile-4. In case of Profile-4, lateral variations in Poisson ratios were observed. However, due to poor quality coverage of the lower-crust along Profile-3 only one Poisson ratio value can be calculated.

8) Conclusions;

- A relatively low quality shear wave data has been recorded on three-component Ocean Bottom Seismometers (OBS) and accompanying Land Stations along the Profiles 3-03 and 4-03. Shear-wave modeling has been performed by using already generated p-wave models utilizing 2-D kinematic ray-tracing. All of the observed s-wave arrivals have been interpreted and modeled to be P to S-conversions at various velocity interface and subjected to mode conversion only once along their ray-path.
- For shallower sediments (1-6 km depths) relatively higher Vp/Vs ratios have been observed i.e. 2.0-2.6. Higher values show the presence of unconsolidated sediments. For deeper sediments (6-11 km depth) present north-western parts of the profiles, Vp/Vs ratios decrease to 1.8-2.0 km. This reduction in Vp/Vs ratio is an indicative of higher compaction in the lower sediments as compared to the upper ones.
- High velocity basement layers act as dominant conversion interfaces especially for those stations which are closer to the land and significantly higher P to S-wave converted energy is observed for greater angle of incidences along basement layers. For upper crust the mean Vp/Vs ratio of 1.75-1.78 indicates its continental origin.
- Upper-crust is composed of quartz-rich granitic rocks under both the profiles. However, the percentage of quartz decreases with depth and mafic character increases.
- The high average Vp/Vs ratios (Vp/Vs=1.84) for lower crust along both the profiles show that it is composed of intermediate-mafic to mafic constituents.

References

Andersen, T. B., Jamtveit, B., Dewey, J. F., & Swensson, E. (1991). Subduction and eduction of continental crust: major mechanisms during continent-continent collision and orogenic extensional collapse, a model based on the south Norwegian Caledonides. Terra Nova, 3(3), 303-310.

Anstey, Nigel Allister. Seismic Interpretation: The Physical Aspects: Being a Record of the Short Course, the New Seismic Interpreter. International Human Resources Development Corporation, 1977.

Beaumont, Christopher, Charlotte E. Keen, and Ross Boutilier. "On the evolution of rifted continental margins: comparison of models and observations for the Nova Scotian margin." Geophysical Journal International 70.3 (1982): 667-715.

Bering, D. "The orientation of minor fault plane striae and the associated deviatoric stress tensor as a key to the fault geometry in part of the More–Trondelag fault zone, on-shore central Norway." Structural and Tectonic Modelling and its Application to Petroleum Geology. Norwegian Petroleum Society (NPF), Special Publications 1 (1992): 83-90.

Bevington, Philip R., and D. Keith Robinson. Data reduction and error analysis for the physical sciences. Vol. 2. New York: McGraw-Hill, 1969.

Birch, Francis. "The velocity of compressional waves in rocks to 10 kilobars: 2." Journal of Geophysical Research 66.7 (1961): 2199-2224.

Blystad, P., Brekke, H., Færsethf, R.B., Skogseid, J. & Tørudbakken, B. 1995. Structural elements of the Norwegian continental shelf. Part II: The Norwegian Sea Region. NPD-Bulletin No. 8, the Norwegian Petroleum Directorate, 45.

Bott, M. H. P. "Crustal doming and the mechanism of continental rifting." Tectonophysics 73.1 (1981): 1-8.

Breivik, A. J., Mjelde, R., Raum, T., Faleide, J. I., Murai, Y., & Flueh, E. R. (2011). Crustal structure beneath the Trøndelag Platform and adjacent areas of the mid--Norwegian margin, as derived from wide-angle seismic and potential field data. Norwegian Journal of Geology, 90, 141-161.

Brekke, Harald, and Frldtjof Riis. "Tectonics and basin evolution of the Norwegian shelf between 62oN and 72oN." Norsk Geologisk Tidsskrift 67.4 (1987): 295-321.

Brekke, Harald. "The tectonic evolution of the Norwegian Sea continental margin, with emphasis on the Voring and More basins." Special Publication-Geological Society of London 167 (2000): 327-378.

Bromirski, P.D., Frazer, L.N., Dunnebier, F.K., 1992. Sediment shear Q from airgun OBS data. Geophys. J. Int. 110, 465–485.

Bukovics, C., Cartier, E. G., Shaw, N. D., and Ziegler, P. A. (1984). Structure and development of the mid-Norway continental margin. In Petroleum geology of the North European margin (pp. 407-423). Springer Netherlands.

Bukovics, Christian, and Peter A. Ziegler. "Tectonic development of the Mid-Norway continental margin." Marine and Petroleum Geology 2.1 (1985): 2-22.

Cassell. B.R., 1982, A method for calculating synthetic seismograms in laterally varying media: Geophys. J. Roy. Astr. SK 69, 339.354

Červený V., Pšenčík L., 1981. 2-D seismic ray package. Res. Rep., Institute of Geophysics, Charles University, Prague.

Cerveny, V., I. A. Molotkov, and I. Psencik (1977). Ray Method in Seismology, Charles Univ. Press, Prague.

Chian, Deping, and Keith E. Louden. "The continent-ocean crustal transition across the Southwest Greenland Margin." Journal of Geophysical Research: Solid Earth (1978–2012) 99.B5 (1994): 9117-9135.

Christensen, N. 1. Poisson‘s ratio and Crustal Seismology, Journal of Geophysical Research, Vol. 101, No. B2, Pages 3139-3156, February 10, 1996

Chung, T.W., Hirata, N., Sato, R., 1990. Two-dimensional P- and S-wave velocity structure of the Yamato Basin, the southern Japan sea, from refraction data collected by an ocean bottom seismographic array. J. Phys. Earth 38, 99–147.

Daley P.F., Krebes E.S. (2004). SH wave propagation in viscoelastic media. Studia Geophysica et Geodaetica 48, 563-587.

Dewey, John F. "Plate tectonics and the evolution of the British Isles Thirty-fifth William Smith Lecture." Journal of the Geological Society 139.4 (1982): 371-412.

Digranes, P., Mjelde, R., Kodaira, S., Shimamura, H., Kanazawa, T., Shiobara, H., & Berg, E. W. (1998). A regional shear-wave velocity model in the central Vøring Basin, N. Norway, using three-component Ocean Bottom Seismographs. Tectonophysics, 293(3), 157-174.

Domenico, S.N., 1984. Rock lithology and porosity determination from shear and compressional wave velocity. Geophysics 49, 1188–1195.

Doré, A. G., and E. R. Lundin. "Cenozoic compressional structures on the NE Atlantic margin; nature, origin and potential significance for hydrocarbon exploration." Petroleum Geoscience 2.4 (1996): 299-311.

Edwin S. Robinson, Cahit Çoruh, Basic exploration geophysics, ISBN 047187941X, 9780471879411, Wiley, 1988, p#15-22.

Eldholm, O and Coffin, MF, Large Igneous Provinces and Plate Tectonics, History and Dynamics of Global Plate Motions, American Geophysical Union, MA Richards, RG Gordon, RD Van Der Hilst (ed), Washington DC, pp. 309-326. ISBN 0-87590-979-5 (2000)

Eldholm, O., Grue, K., 1994. North Atlantic volcanic margins: Dimensions and production rates. J. Geophys. Res. 99, 2955–2968.

Fossen, Haakon. "Extensional tectonics in the Caledonides: Synorogenic or postorogenic?." Tectonics 19.2 (2000): 213-224.

Foucher, J. P., Le Pichon, X., Sibuet, J. C., Roberts, D. G., Chenet, P. Y., Bally, A. W., ... & Turcotte, D. L. (1982). The Ocean--Continent Transition in the Uniform Lithospheric Stretching Model: Role of Partial Melting in the Mantle [and Discussion]. Philosophical Transactions of the Royal Society of London. Series A, Mathematical and Physical Sciences, 305(1489), 27-43.

Gabrielsen, R. H., Foerseth, R., Hamar, G., & Rønnevik, H. (1984). Nomenclature of the main structural features on the Norwegian Continental Shelf north of the 62nd parallel. In Petroleum Geology of the North European Margin (pp. 41-60). Springer Netherlands.

Gabrielsen, Roy H., Rune Kyrkjebø, Jan Inge Faleide, Willy Fjeldskaar, and Tomas Kjennerud. "The Cretaceous post-rift basin configuration of the northern North Sea." Petroleum Geoscience 7, no. 2 (2001): 137-154.

Gaiser, James E. "Compensating OBC data for variations in geophone coupling." 1998, SEG Annual Meeting, 1998.

Grønlie, A., et al. "Fission-track and K-Ar dating of tectonic activity in a transect across the Møre-Trøndelag Fault Zone, central Norway." Norsk Geologisk Tidsskrift 74.1 (1994): 24-34.

Haller, J., Haller, J., Haller, J., Haller, J., & Geologist, S. (1971). Geology of the East Greenland Caledonides (p. 415). New York: Interscience.

Hamilton, E.L., 1979. Vp=Vs and Poisson's ratio in marine sediments and rocks. J. Acoust. Soc. Am. 66, 1093–1101.

Hellinger, Steven J., and John G. Sclater. "Some comments on two-layer extensional models for the evolution of sedimentary basins." Journal of Geophysical Research: Solid Earth (1978–2012) 88.B10 (1983): 8251-8269

Holbrook, W. Steven, Dirk Gajewski, and Claus Prodehl. "Shear wave velocity and Poisson's ratio structure of the upper lithosphere in southwest Germany." Geophysical Research Letters 14.3 (1987): 231-234.

Holbrook, W. Steven, Dirk Gajewski, Anton Krammer, and Claus Prodehl. "An interpretation of wide-angle compressional and shear wave data in southwest Germany: Poisson's ratio and petrological implications." Journal of Geophysical Research: Solid Earth (1978–2012) 93, no. B10 (1988): 12081-12106

Holbrook, W.S., Mooney, W.D., Christensen, N.J., 1992. The seismic velocity structure of the deep continental crust. In: Fountain, D.M., Arculus, R., Kay, R.W. (Eds.), Continental Lower Crust. Development in Geotectonics 23, Elsevier, Amsterdam, pp. 1–43.

Julian, B. R. and D. Gubbins (1977). Three dimensional seismic ray tracing, J. Geophys. 43, 95-114.

Kearey, Philip, Michael Brooks, and Ian Hill. An introduction to geophysical exploration. Wiley-Blackwell, 2009.

Kodaira, S., Bellenberg, M., Iwasaki, T., Kanasawa, T., Hirschleber, H.B., Shimamura, H., 1996. Vp=Vs ratio structure of the Lofoten continental margin, northern Norway, and its geological implications. Geophys. J. Int. 124, 724–740.

Luetgert, J., 1992. Macray—interactive two-dimensional seismic raytracing for the Macintosh, USGS Open File Rept, 92–356.

McKenzie, Dan. "Some remarks on the development of sedimentary basins." Earth and planetary science letters 40.1 (1978): 25-32.

McMechan, G.A. and Mooney, W.D., 1980. Asymptotic ray theory and synthetic seismograms for laterally varying structures: theory and application to the Imperial Valley, California, Bull. seism. Soc. Am., 70, 2021–2035.

Milnes, A. G., O. P. Wennberg, Ø. Skår, and A. G. Koestler. "Contraction, extension and timing in the South Norwegian Caledonides: the Sognefjord transect." Geological Society, London, Special Publications 121, no. 1 (1997): 123-148.

Mjelde, R., Myhre, B., Sellevoll, M.A., Shimamura, H., Iwasaki, T., Kanazawa, T., 1996b. Modelling of S-waves from an area covered with flood-basalts off Lofoten, N. Norway. Geophys. Trans. 40 (1), 95–117.

Mjelde, R., Sellevoll, M.A., 1993. Possible shallow crustal S-wave anisotropy off Lofoten, Norway, inferred from 3-C Ocean Bottom Seismographs. Geophys. J. Int. 115, 159–167.

Müller, Reidar, Johan Petter Ngstuen, Frøydis Eide, and Hege Lie. "Late Permian to Triassic basin infill history and palaeogeography of the Mid-Norwegian shelf—East Greenland region." Norwegian Petroleum Society Special Publications 12 (2005): 165-189.

Neugebauer, H. J., W. D. Woidt, and H. Wallner. "Uplift, volcanism and tectonics: evidence for mantle diapirs at the Rhenish Massif." Plateau Uplift, The Rhenish Massif—A Case History (1983): 381-403.

Pickett, G. R. "Acoustic character logs and their applications in formation evaluation." Journal of Petroleum Technology 15.6 (1963): 659-667.

Price, I., and R. P. Rattey. "Cretaceous tectonics off mid-Norway: implications for the Rockall and Faeroe-Shetland troughs." Journal of the Geological Society 141.6 (1984): 985-992.

Robinson, E. S., and C. Coruh. "Basic exploration geophysics Wiley." New Yor-k (1988).

Royden, Leigh, J. G. Sclater, and R. P. Von Herzen. "Continental margin subsidence and heat flow: important parameters in formation of petroleum hydrocarbons." AAPG Bulletin 64.2 (1980): 173-187.

Skogseid, J., Pedersen, T., Eldholm, O., Larsen, B.T., 1992. Tectonism and magmatism during NE Atlantic continental break-up: the Vøring margin. In: Story, B.C., Alabaster, T., Pankhurst, R.J. (Eds.), Magmatism and the Causes of Continental Breakup. Geol. Soc. London Spec. Publ. 68, 305–320.

Smelror, Morten, John Dehls, Jörg Ebbing, Eiliv Larsen, Erik R. Lundin, Øystein Nordgulen, Per Terje Osmundsen et al. "Towards a 4D topographic view of the Norwegian sea margin." Global and Planetary Change 58, no. 1 (2007): 382-410.

Smythe, D. K., J. A. Chalmers, and A. G. Skuce. "Dobinson. A., and Mould, AS, 1983. Early opening history of the North Atlantic—I. Structure and origin of the Faroe-Shetland Escarpment." Geophys. J. R. Astron. Soc 72: 373-398.

Spence, G.D., 1983. RAYAMP: An algorithm for tracing rays and calculating amplitudes in laterally varying media: program documentation. Univ. of British Columbia.

Spence, G.D., Whittall, K.P. and Clowes, R.M., 1984. Practical synthetic seismograms for laterally varying media calculated by asymptotic ray theory, Bull. seism. Soc. Am., 74, 1209–1223

Stein, Seth, and Michael Wysession. An introduction to seismology, earthquakes, and earth structure. Wiley-Blackwell, 2009. p=55-113.

Surlyk, Finn, S. Piasecki, F. Rolle, L. Stemmerik, E. Thomsen, and P. Wrang. "The Permian base of East Greenland." In Petroleum geology of the North European margin, pp. 303-315. Springer Netherlands, 1984.

Svetlov, 1. L., A. 1. Epistian, A. 1. Krivko, A. 1. Samoil, 1. N. Odintsev, and A.P. Andreev, Anisotropy of Poisson's ratio of single crystals of nickel alloy, Sov. Phys. Dokl., 33, 771-773, 1988.

Tatham, R. H., M. D. McCormack, R. H. Tatham, and M. D. McCormack. "3. Rock Physics Measurements." In Multicomponent Seismology in Petroleum Exploration, edited by E. B. Neitzel, and D. F. Winterstein, pp. 43-92. Society of Exploration Geophysicists, 1991.

Tatham, R.H., 1985. Shear waves and lithology. In: Dohr, G. (Ed.), Seismic Shear Waves, Part B. Applications. Geophysical Press, London, pp. 86–133.

Terry, Michael P., Peter Robinson, Michael A. Hamilton, and Michael J. Jercinovic. "Monazite geochronology of UHP and HP metamorphism, deformation, and exhumation, Nordøyane, Western Gneiss Region, Norway." American Mineralogist 85, no. 11-12 (2000): 1651-1664.

Turcotte, D. L. "Rifts--tensional failures of the lithosphere." LPI Contributions 457 (1981): 5.

Underhill, J. R. "Jurassic." Petroleum Geology of the North Sea: Basic Concepts and Recent Advances, Fourth Edition (1998): 245-293.

Whitmarsh, R.B., Miles, P.R., 1990. In situ measurements of shear-wave velocity in ocean sediments. In: Hovem, J.M., Richardson, M.D., Stoll, R.D. (Eds.), Shear Waves in Marine Sediments. Kluwer, Dordrecht, pp. 321–328.

Yilmaz, Özdoğan. Seismic data analysis: processing, inversion, and interpretation of seismic data. No. 10. SEG Books, 2001.

Zelt, C. A. and D. J. White, Crustal structure and tectonics of the southeastern Canadian Cordillera, J. Geophys. Res., 100, 24255-24273, 1995.

Zelt, C. A. and R. M. Ellis, Practical and efficient ray tracing in two-dimensional media for rapid travel time and amplitude forward modelling, Can. J. Expl. Geophys., 24, 16-31, 1988.

Zelt, C. A., 3-D velocity structure from simultaneous traveltime inversion of in-line seismic data along intersecting profiles, Geophys. J. Int., 118, 795-801, 1994.

Zelt, C. A., Modelling strategies and model assessment for wide-angle seismic traveltime data, Geophys. J. Int., 139, 183-204, 1999.

Ziegler, Peter A. Geological Atlas of Western and Central Europe: 1982. Vol. 1. Geological Society, 1982.

APPENDIX

On the following pages are the data from the OBS and Land-stations, modeled rays and the calculated and observed travel times for each OBS. The arrivals have also been denoted by the naming convention given in Table 6.1 of the thesis.

Appendix consists of seismic data from each OBS & Land stations from Profile-04-03 & 03,

along with traced-rays & observed & calculated times.

Order is…

1. Profile#3

Land-stations starting from SE up to last land-station to NW.

OBS's starting from SE up to last OBS to NW.

2. Profile#4

Land-stations starting from SE up to last land-station to NW.

OBS's starting from SE up to last OBS to NW.

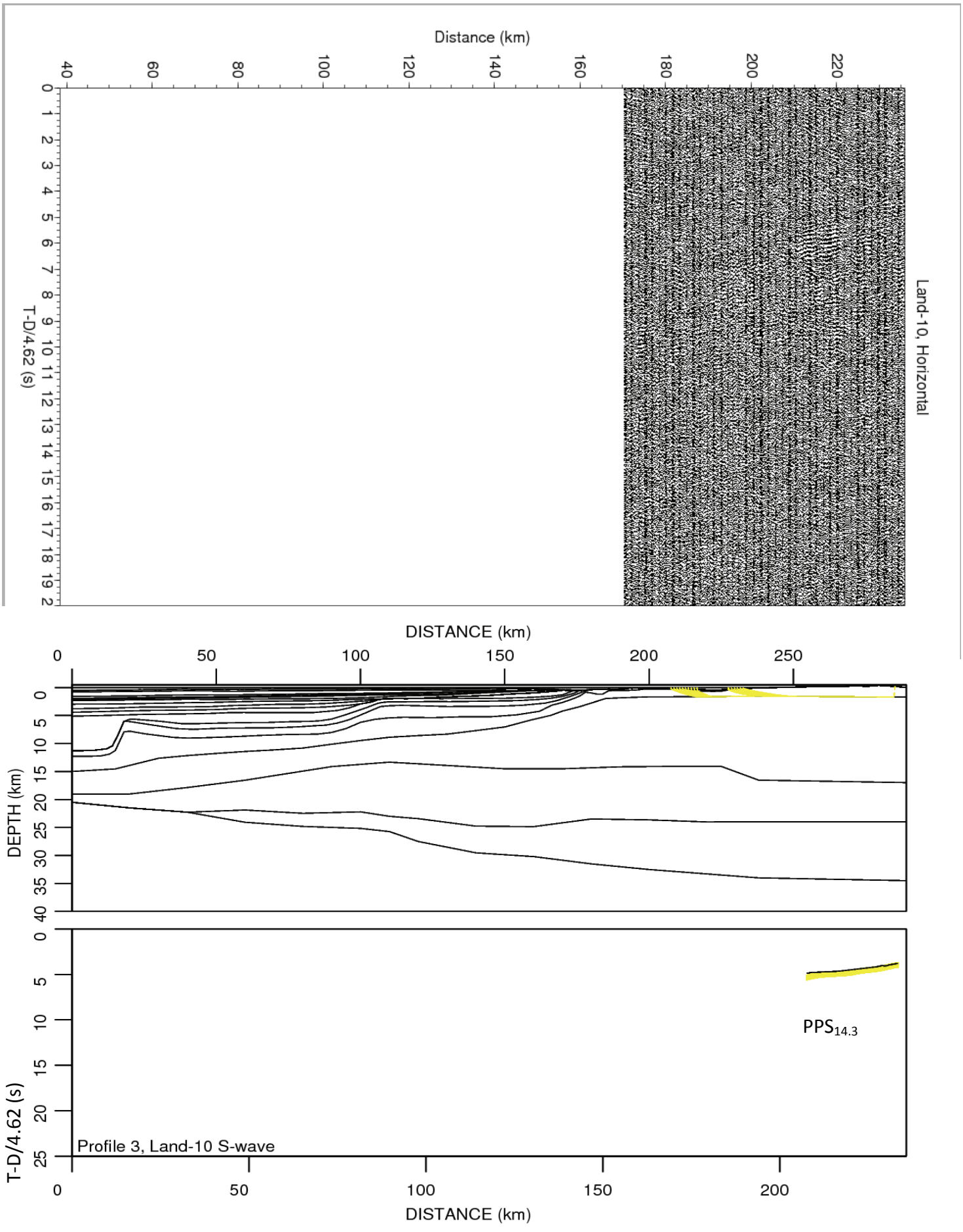

Horizontal component of Land-10 with data plotted in SU and the rays, interpreted and calculated arrivals from Rayinvr.

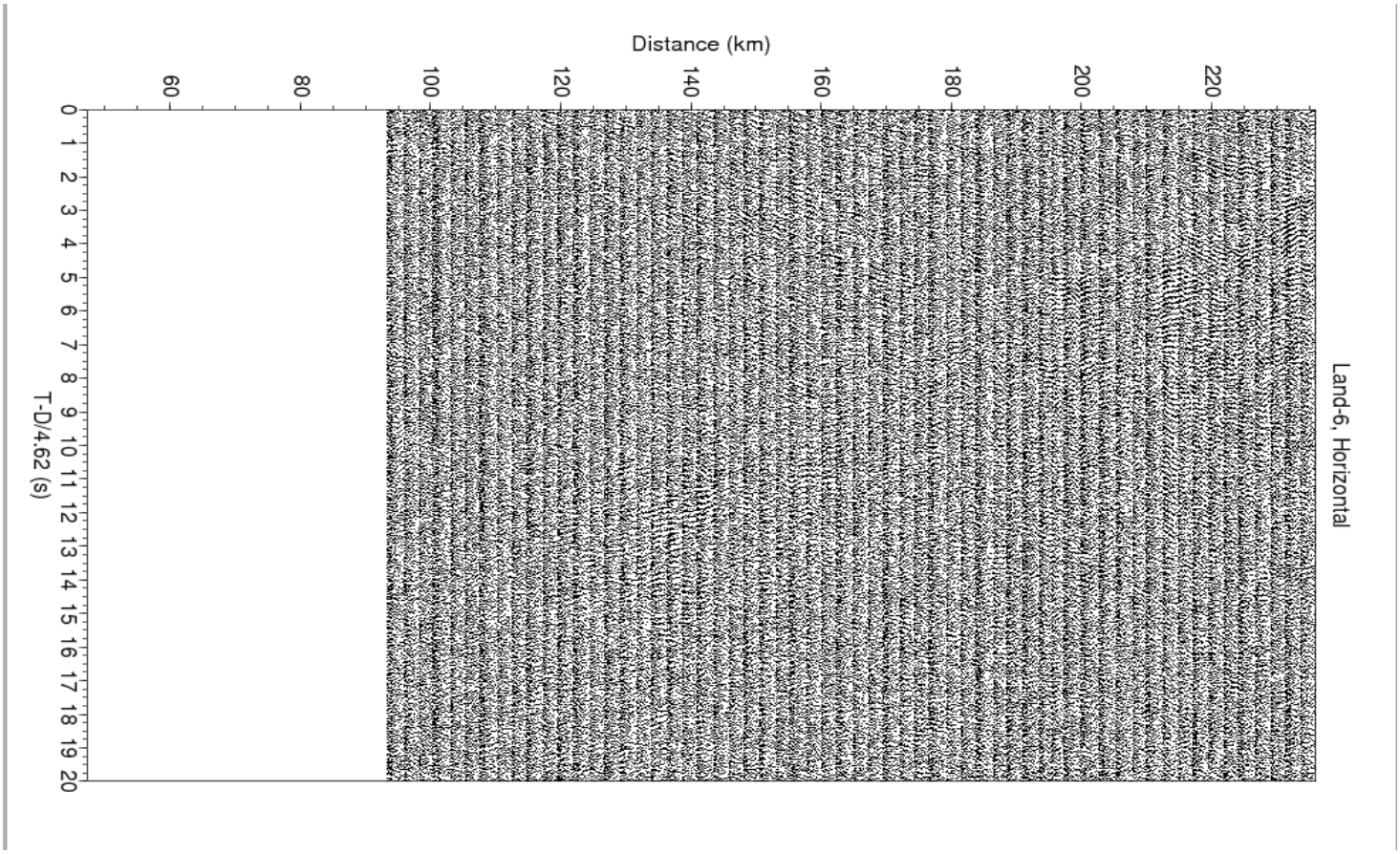

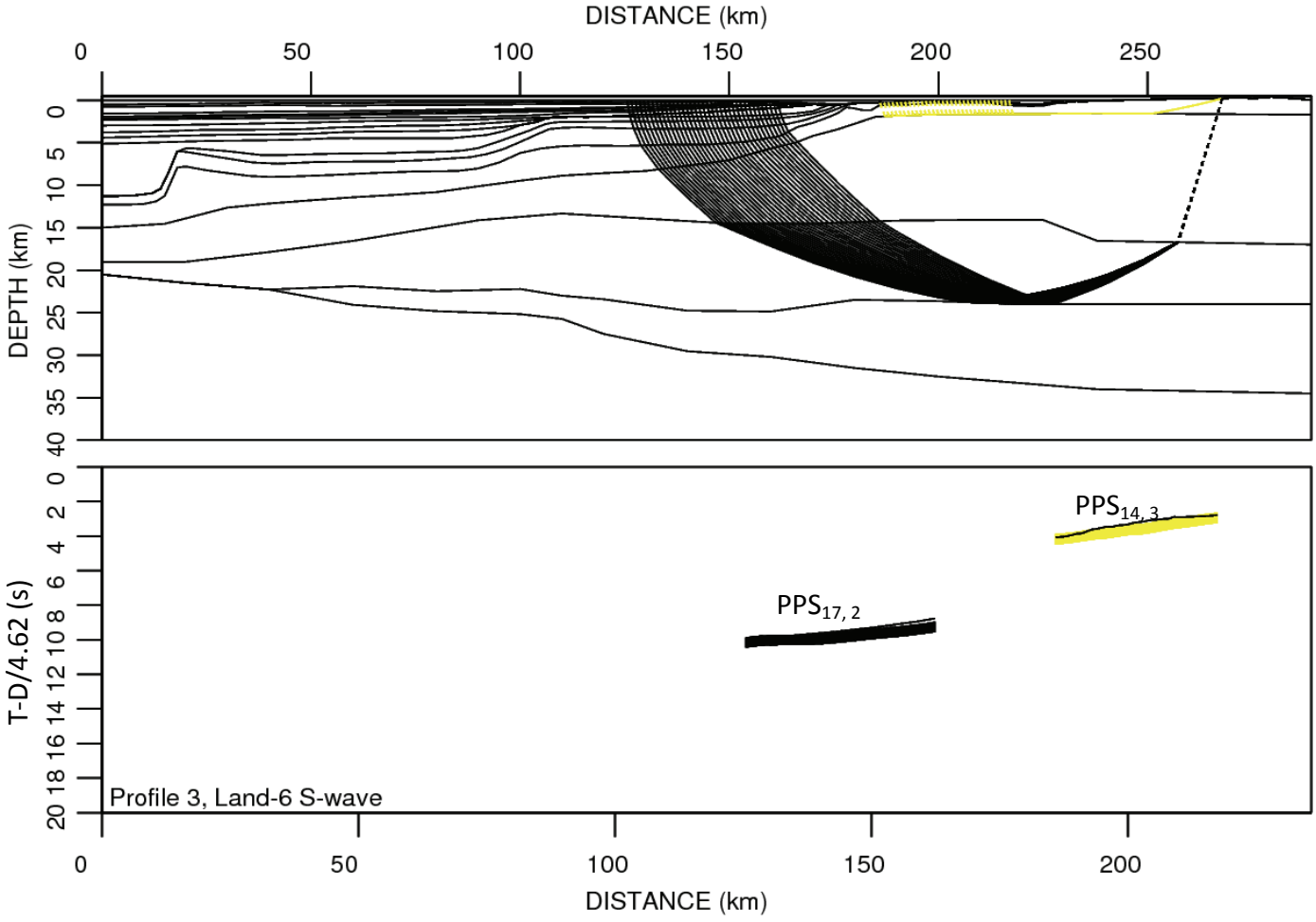

Horizontal component of Land-6 with data plotted in SU and the rays, interpreted and calculated arrivals from Rayinvr.

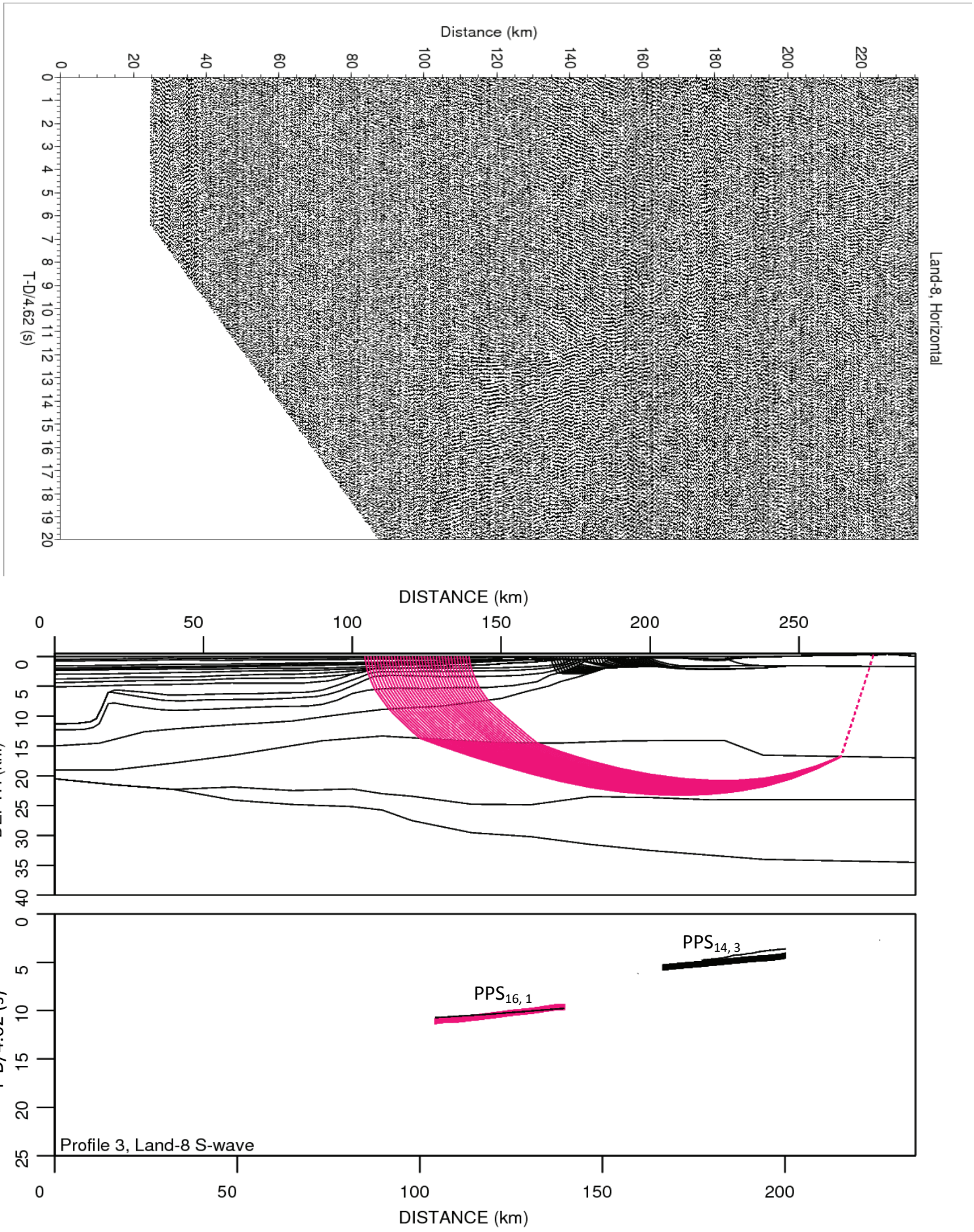

Horizontal component of Land-8 with data plotted in SU and the rays, interpreted and calculated arrivals from Rayinvr.

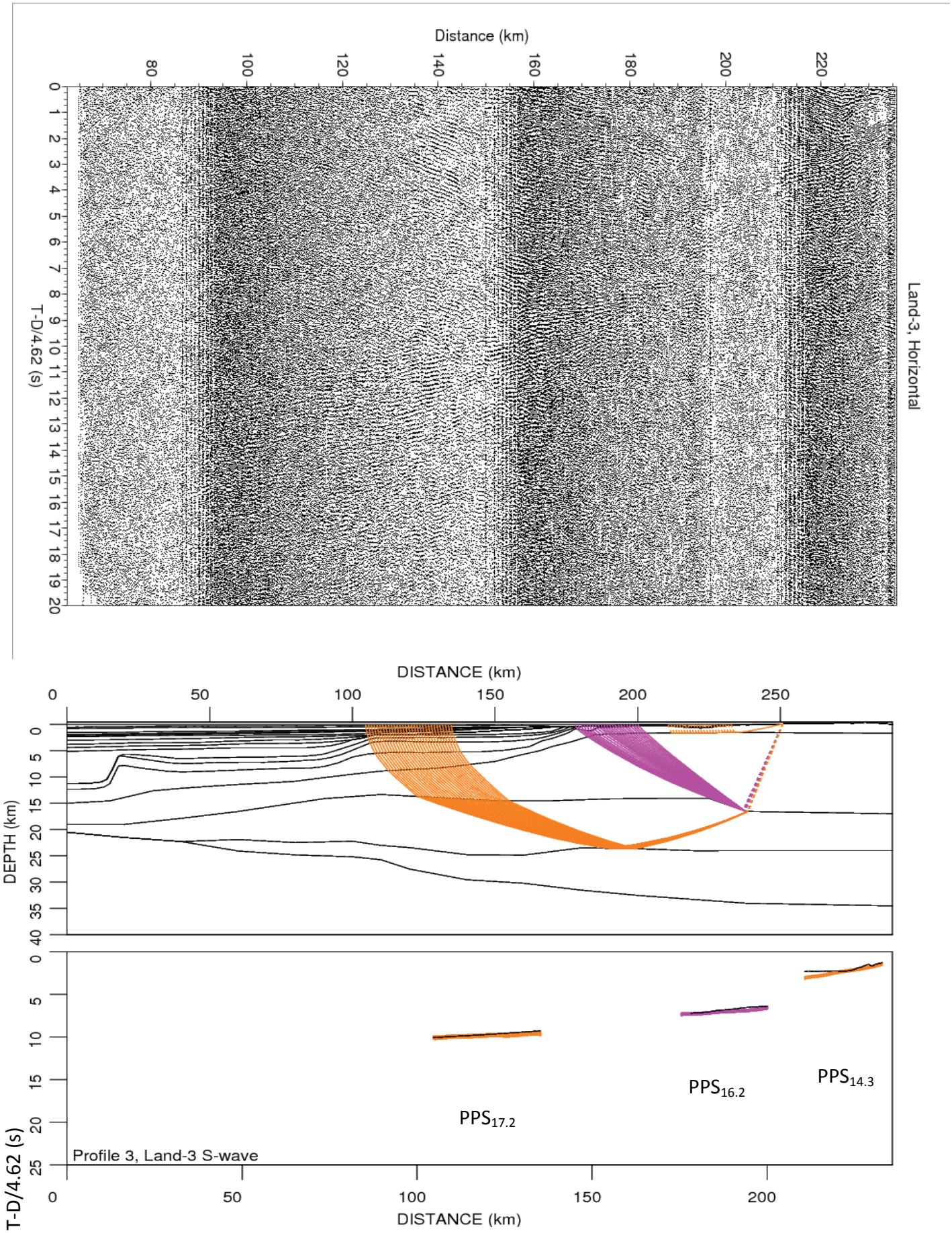

Horizontal component of Land-3 with data plotted in SU and the rays, interpreted and calculated arrivals from Rayinvr.

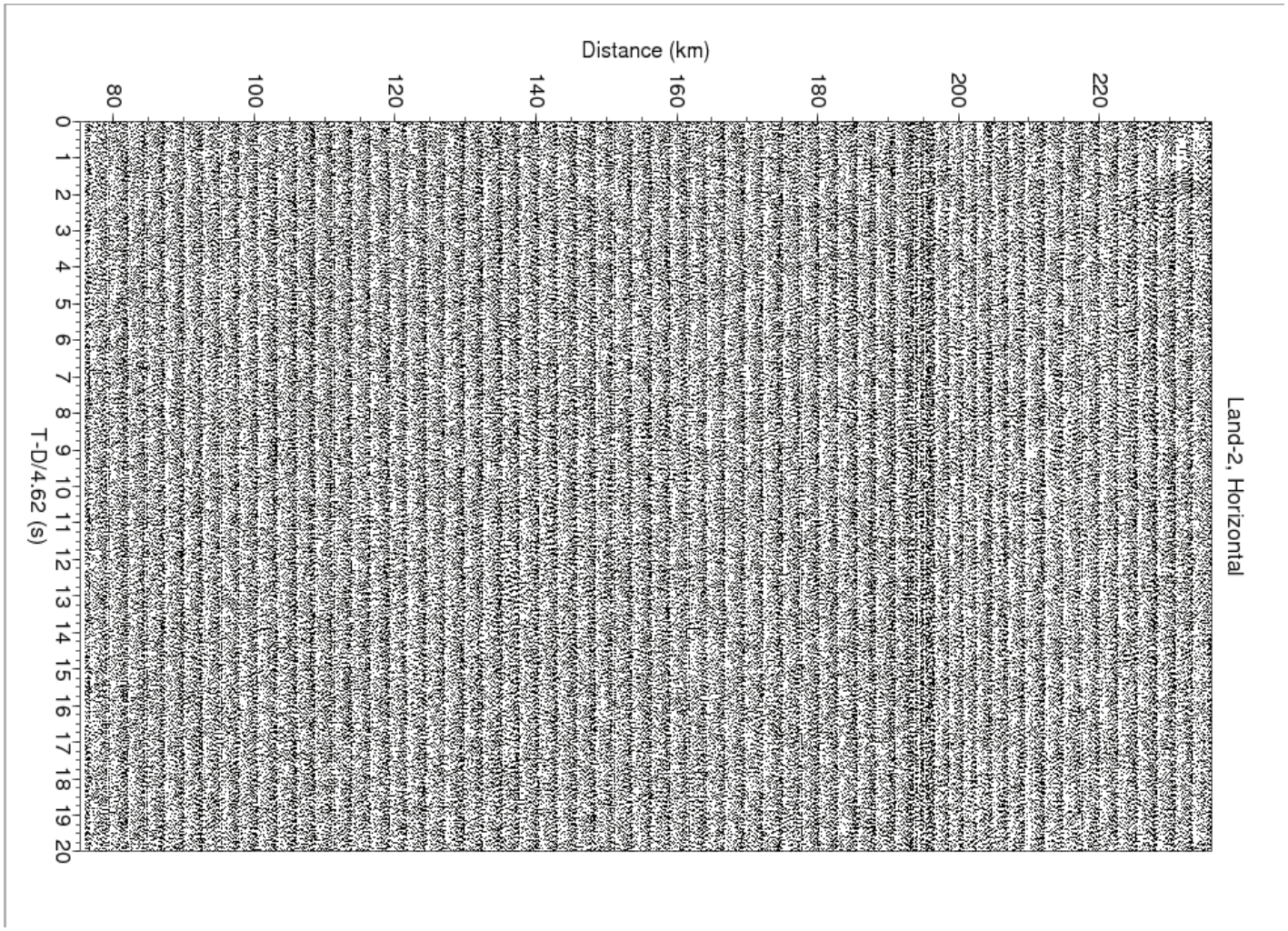

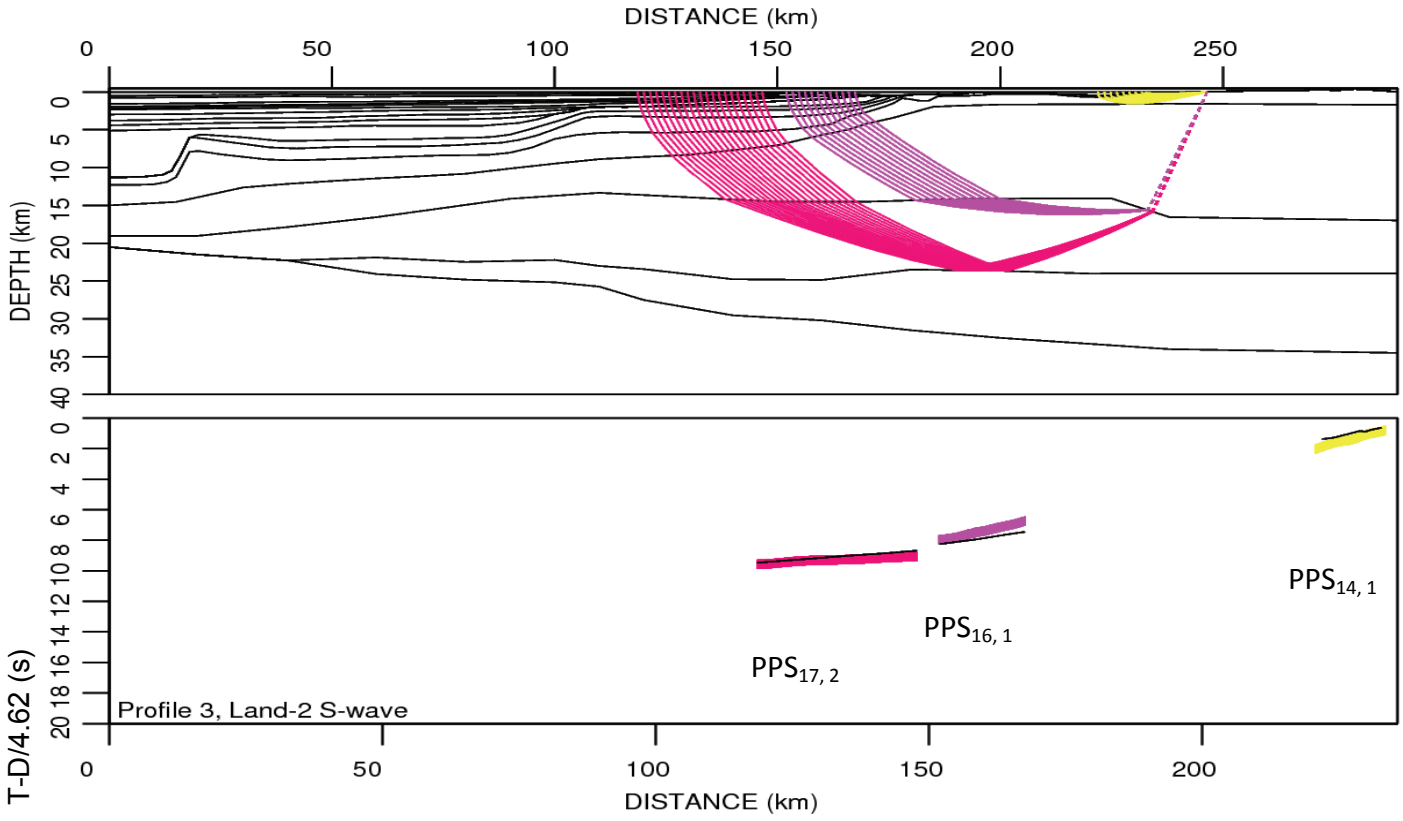

Horizontal component of Land-2 with data plotted in SU and the rays, interpreted and calculated arrivals from Rayinvr.

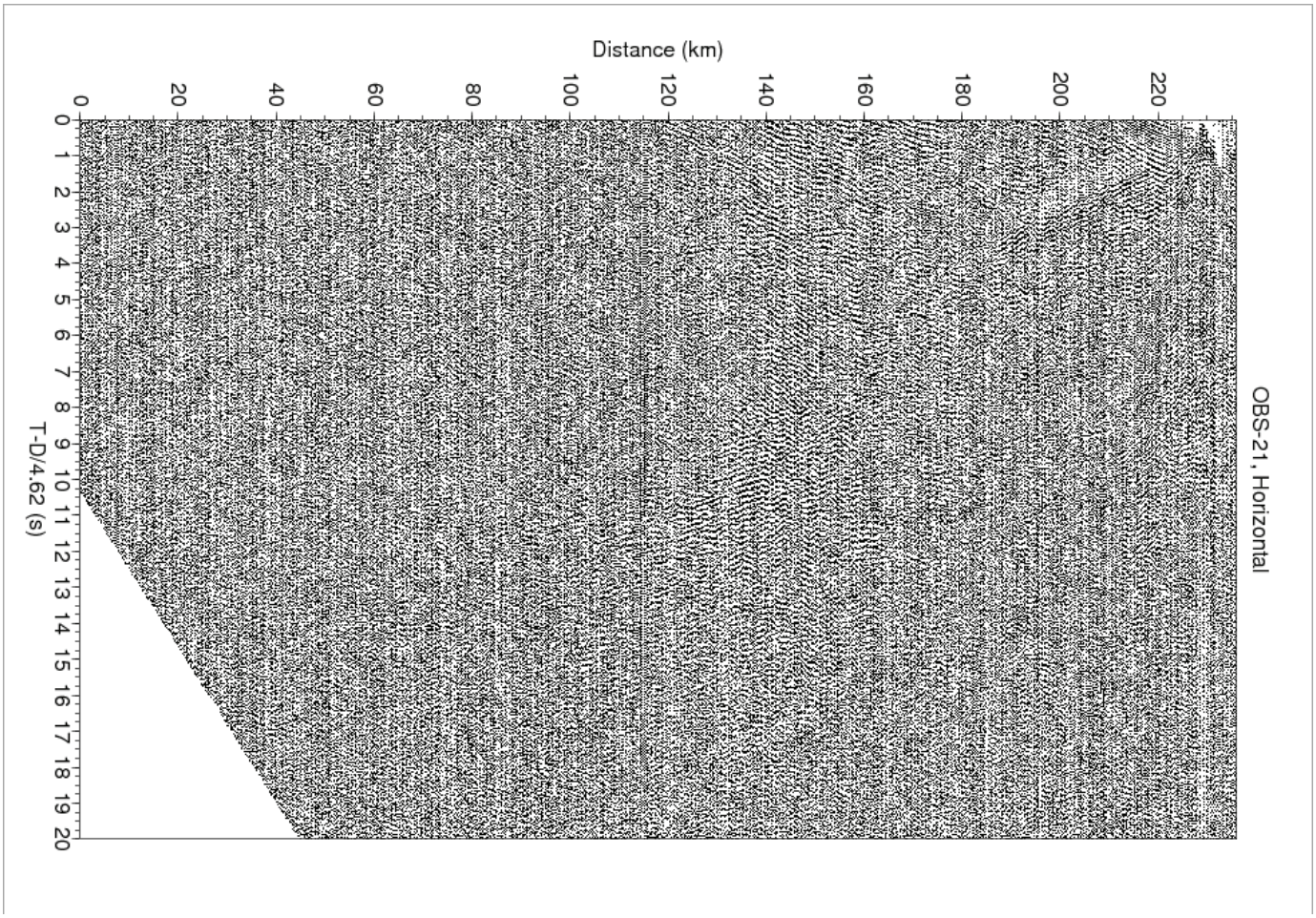

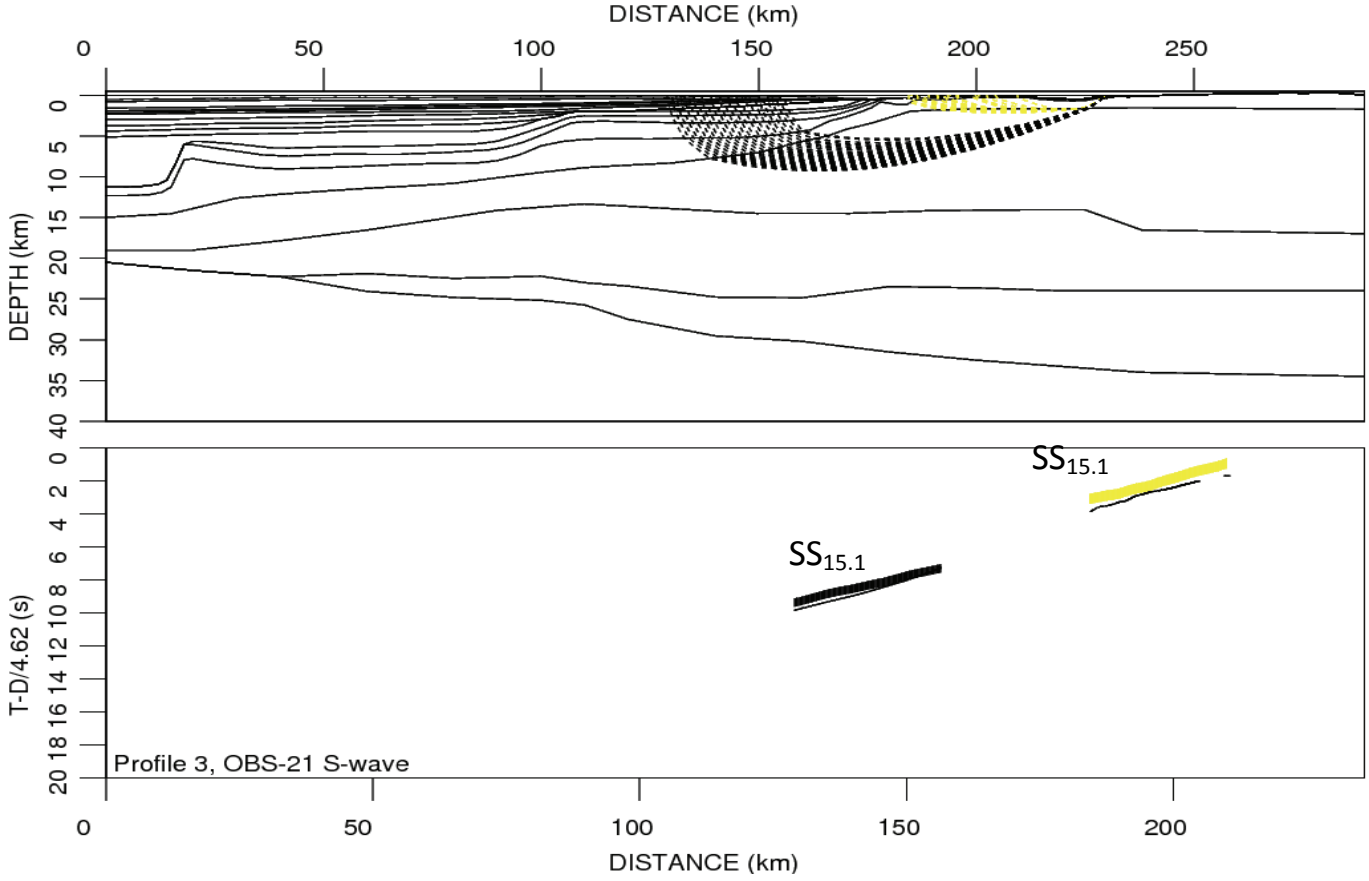

Horizontal component of OBS-21 with data plotted in SU and the rays, interpreted and calculated arrivals from Rayinvr.

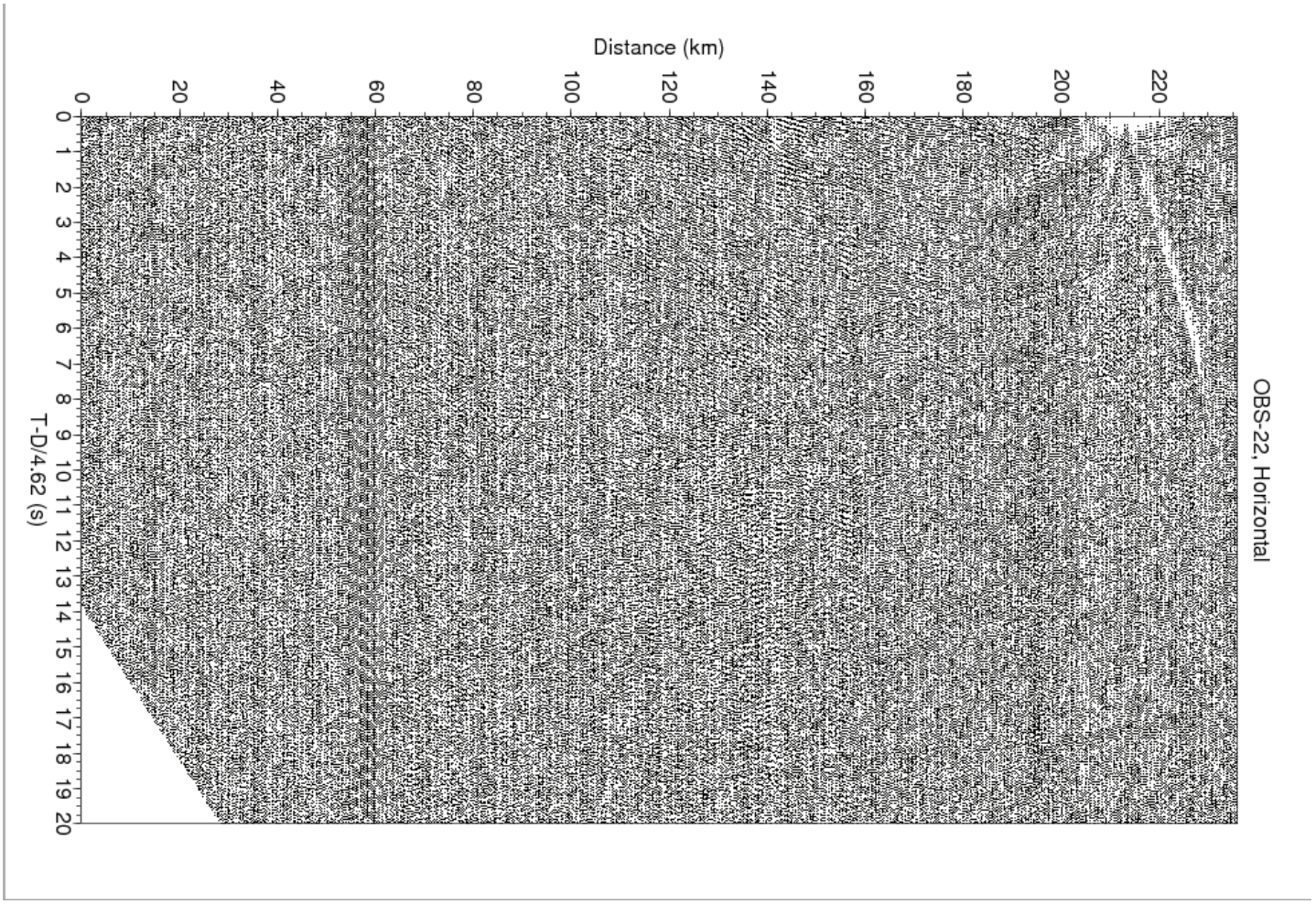

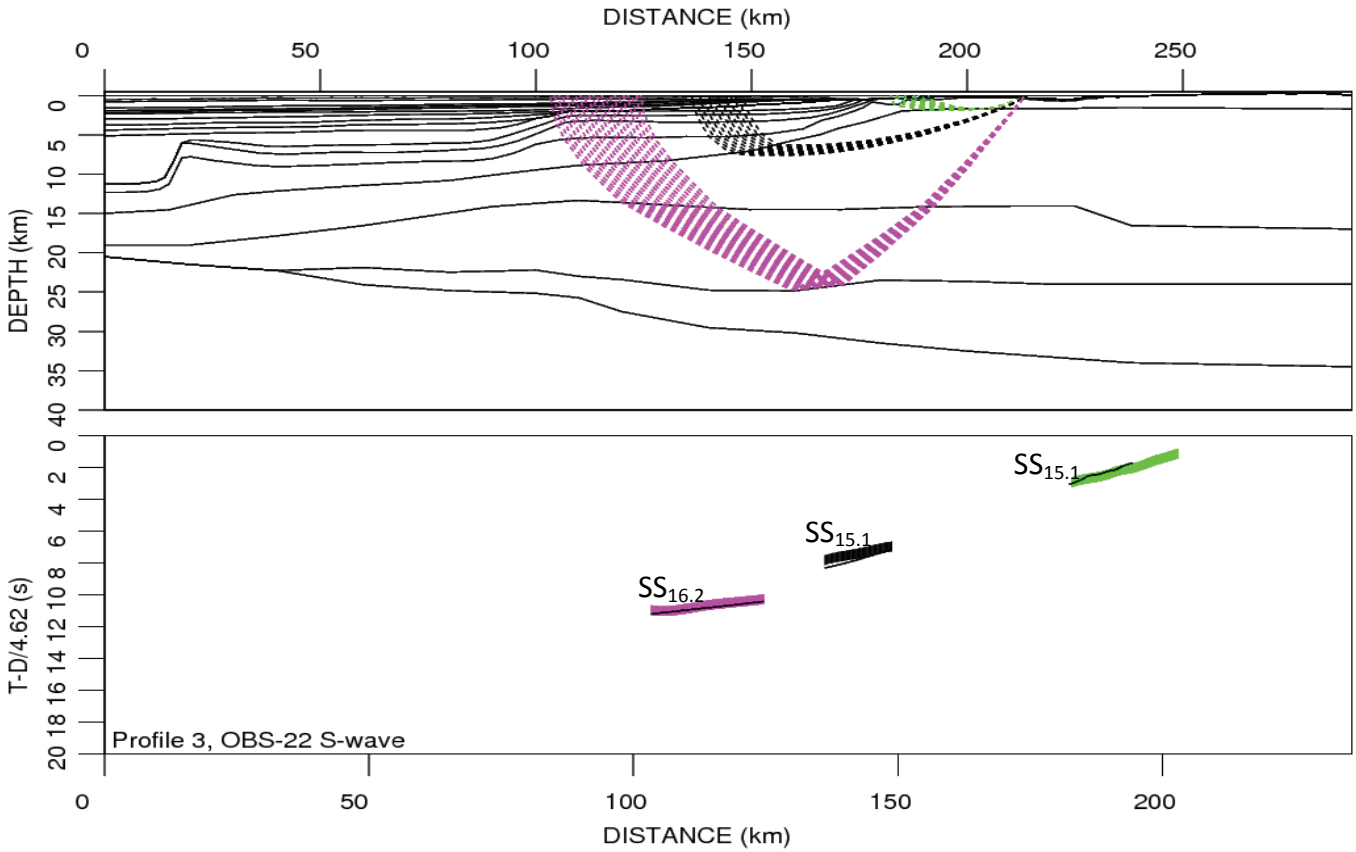

Horizontal component of OBS-22 with data plotted in SU and the rays, interpreted and calculated arrivals from Rayinvr.

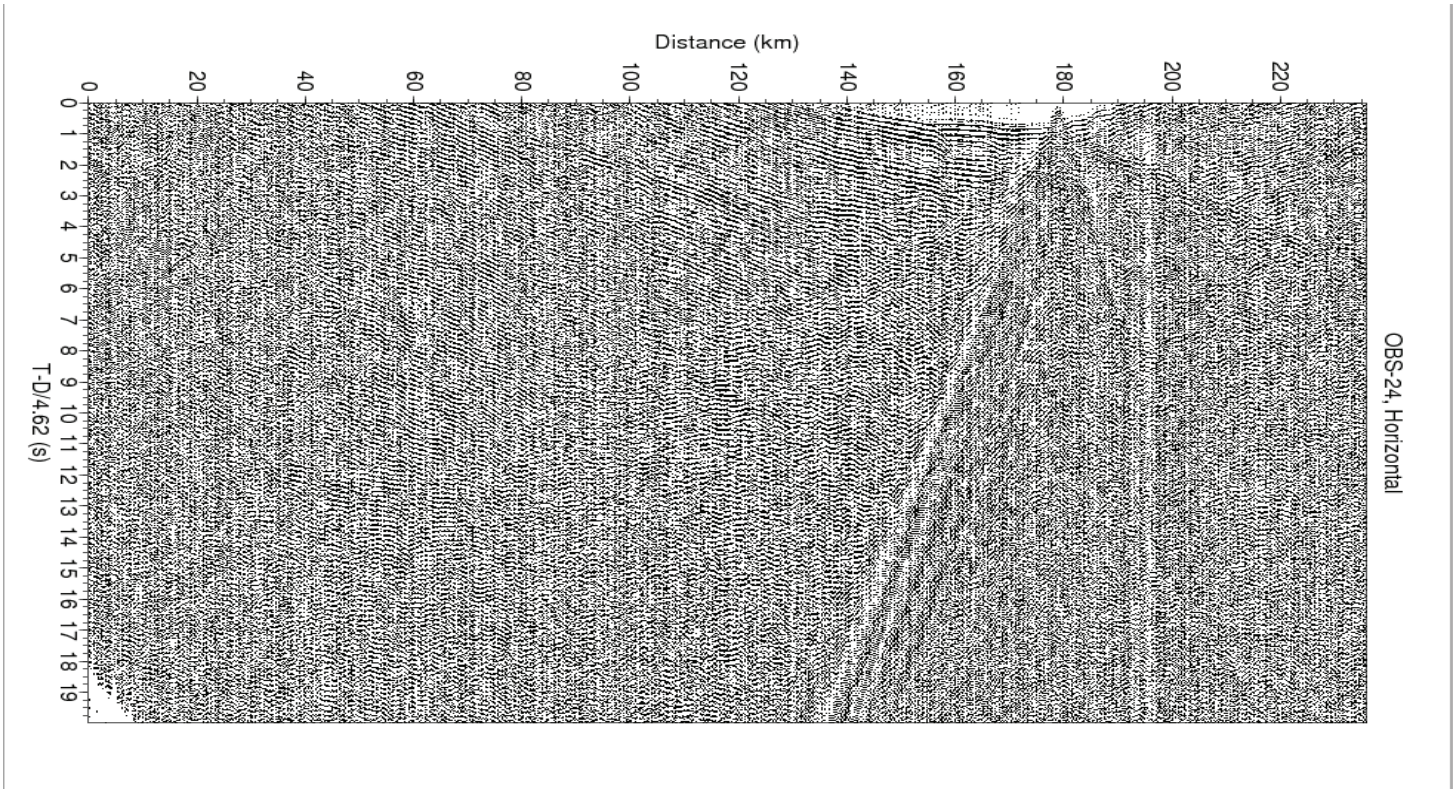

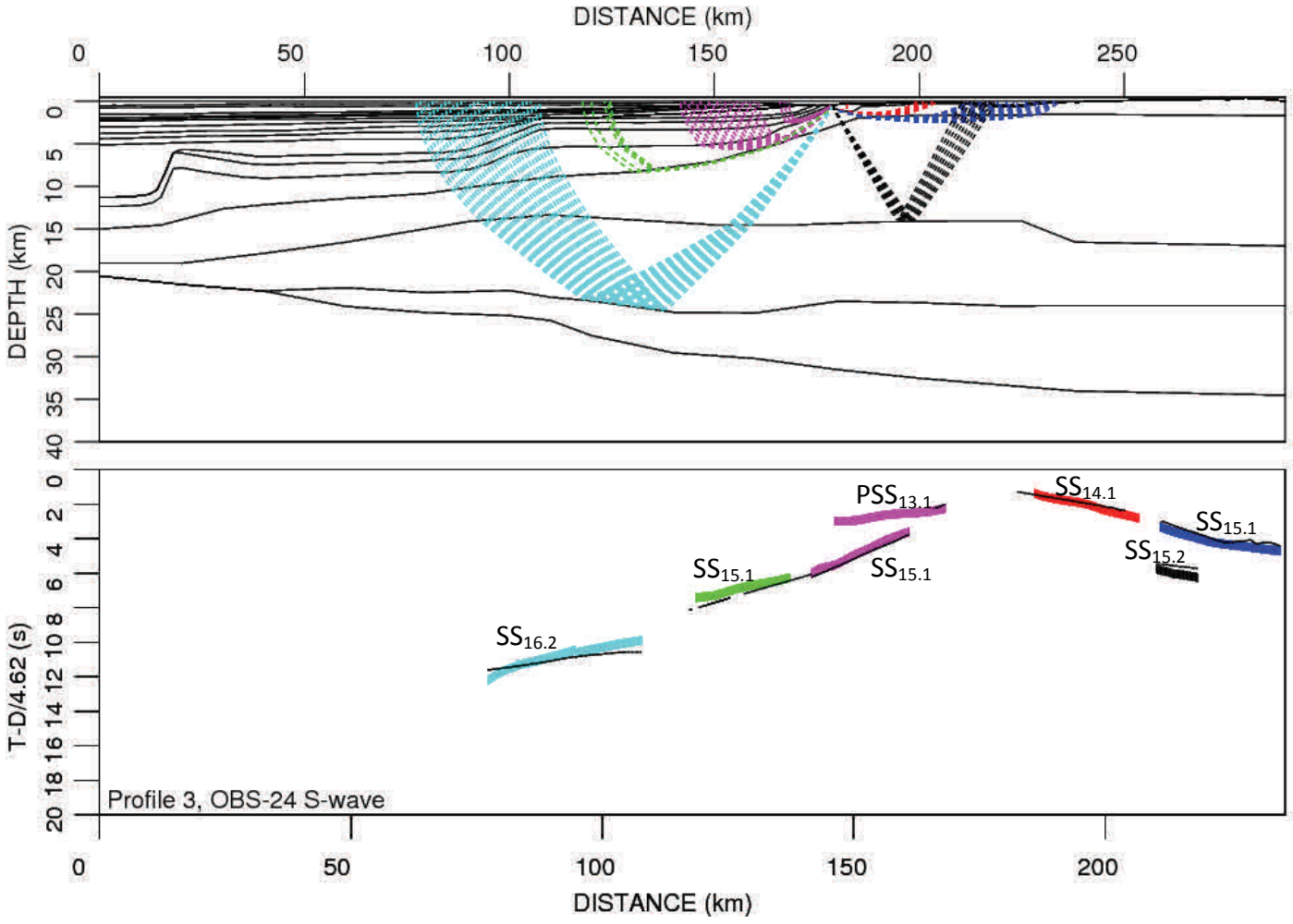

Horizontal component of OBS-24 with data plotted in SU and the rays, interpreted and calculated arrivals from Rayinvr.

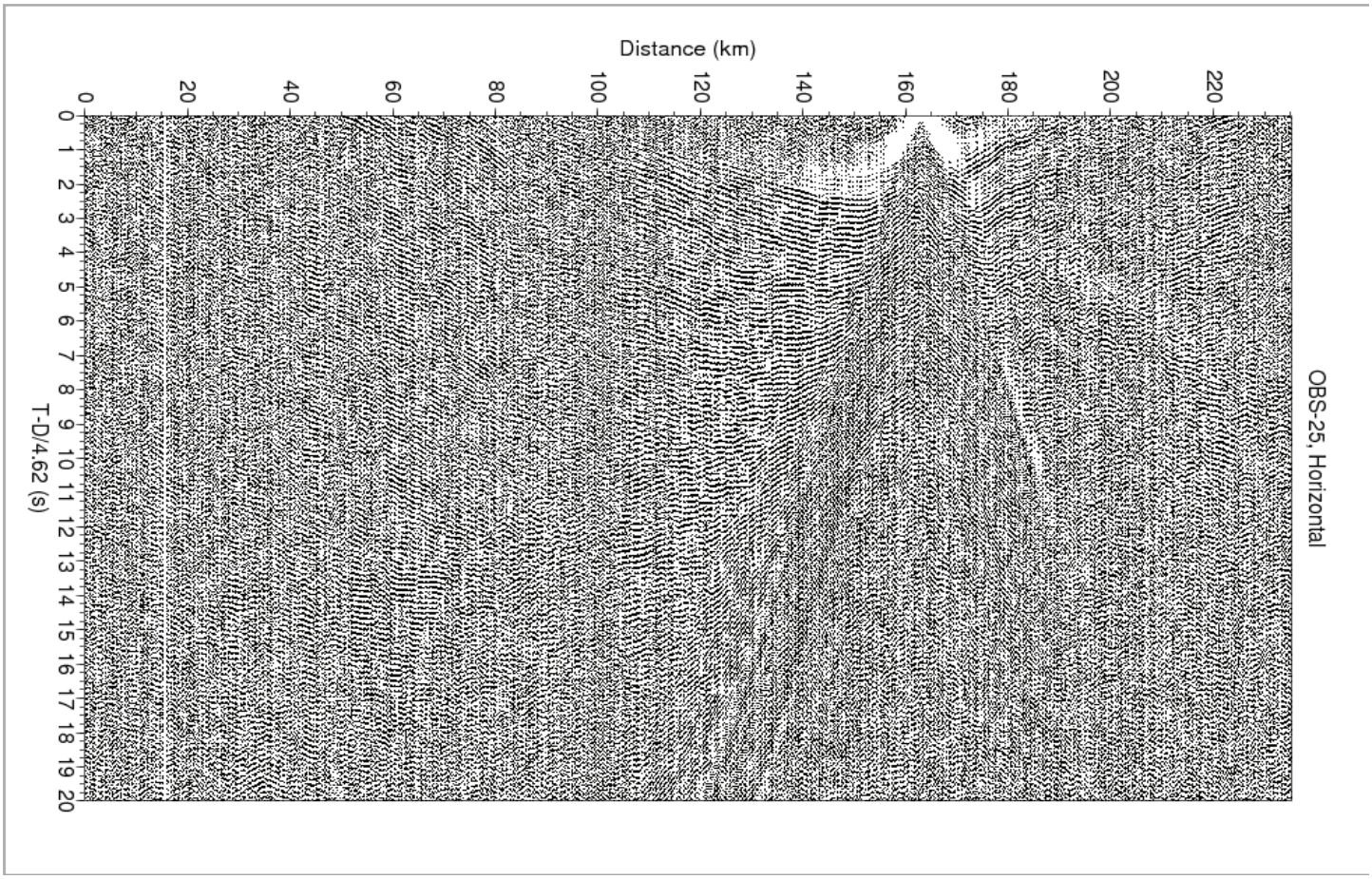

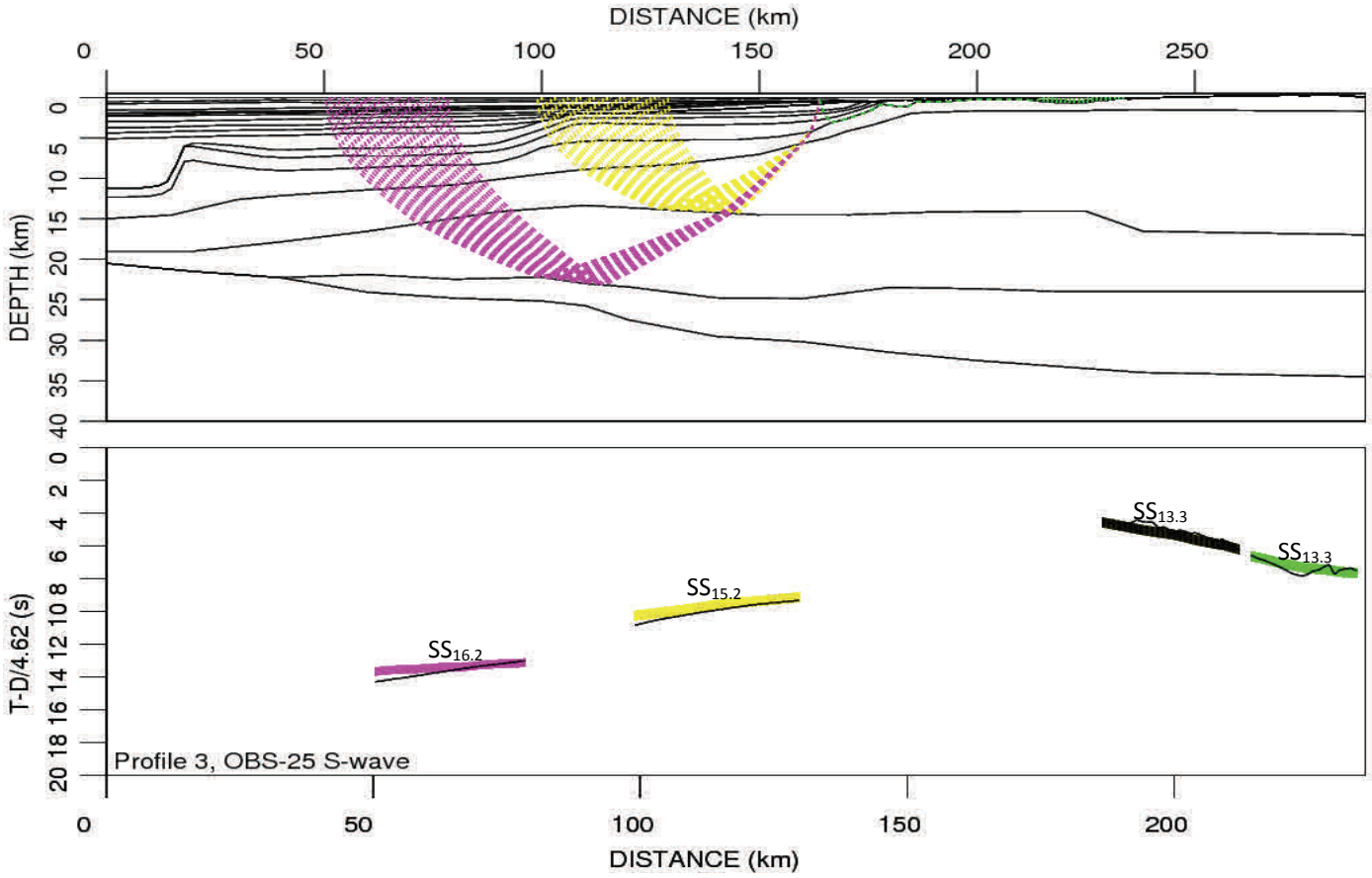

Horizontal component of OBS-25 with data plotted in SU and the rays, interpreted and calculated arrivals from Rayinvr.

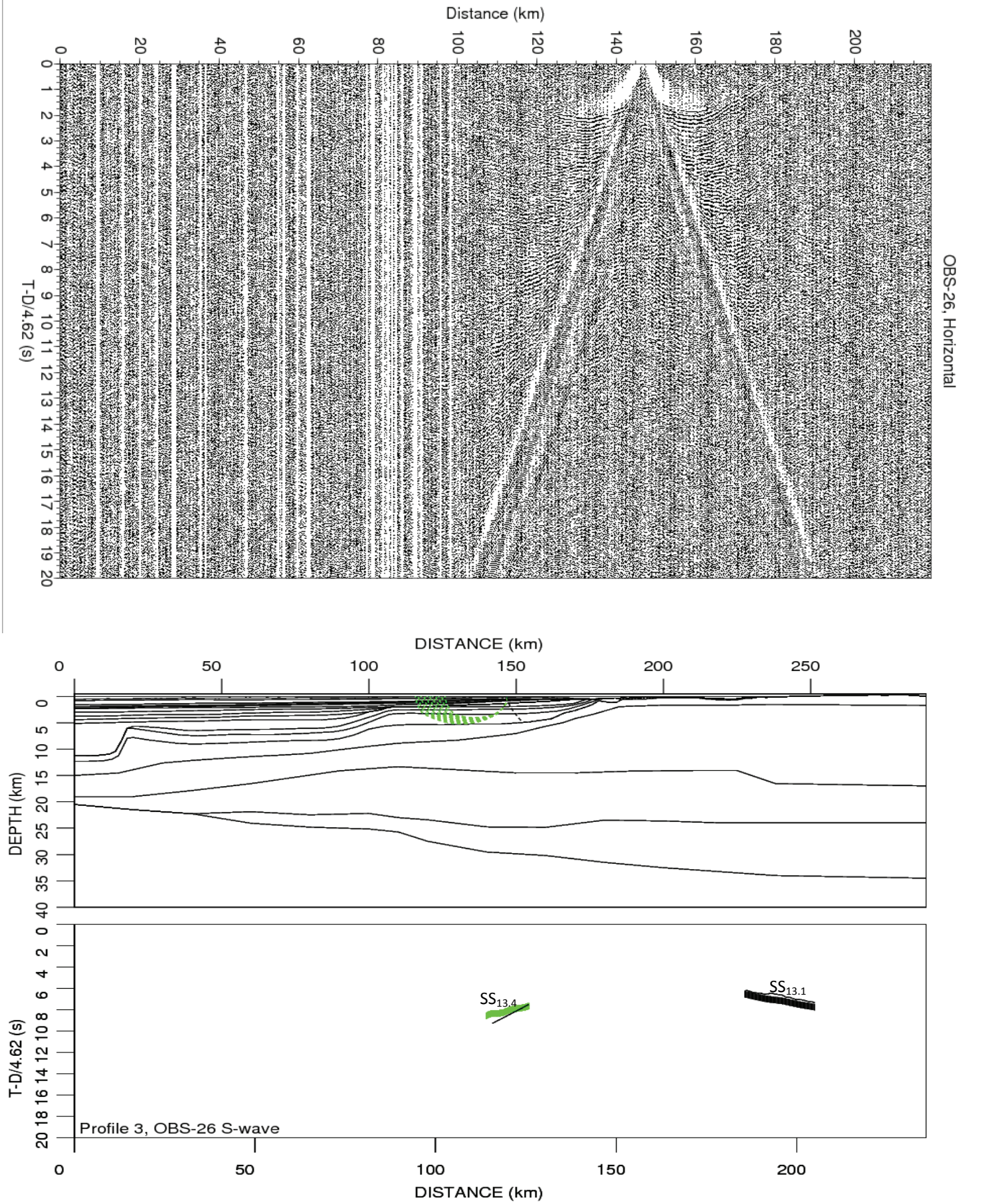

Horizontal component of OBS-26 with data plotted in SU and the rays, interpreted and calculated arrivals from Rayinvr.

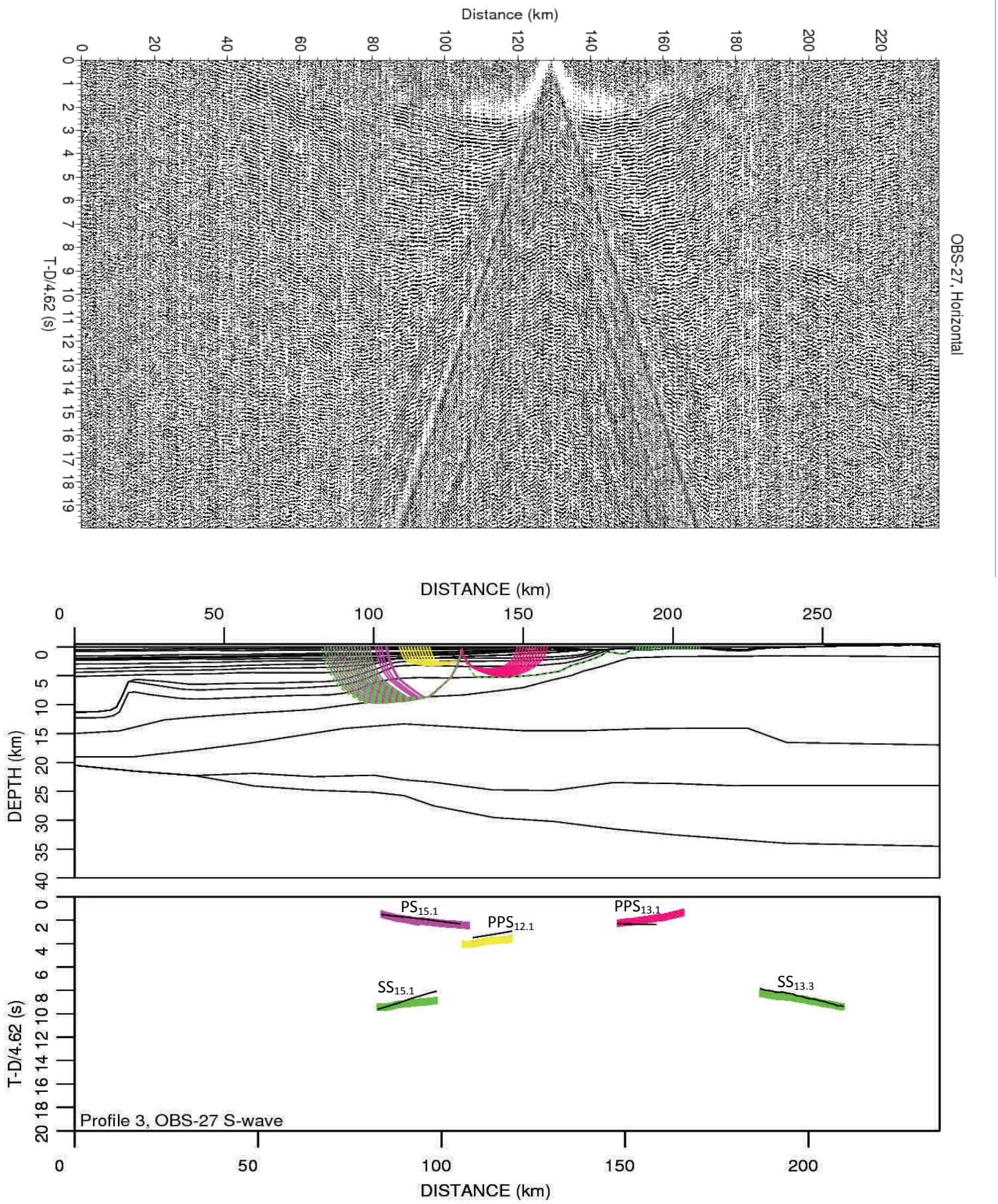

Horizontal component of OBS-27 with data plotted in SU and the rays, interpreted and calculated arrivals from Rayinvr.

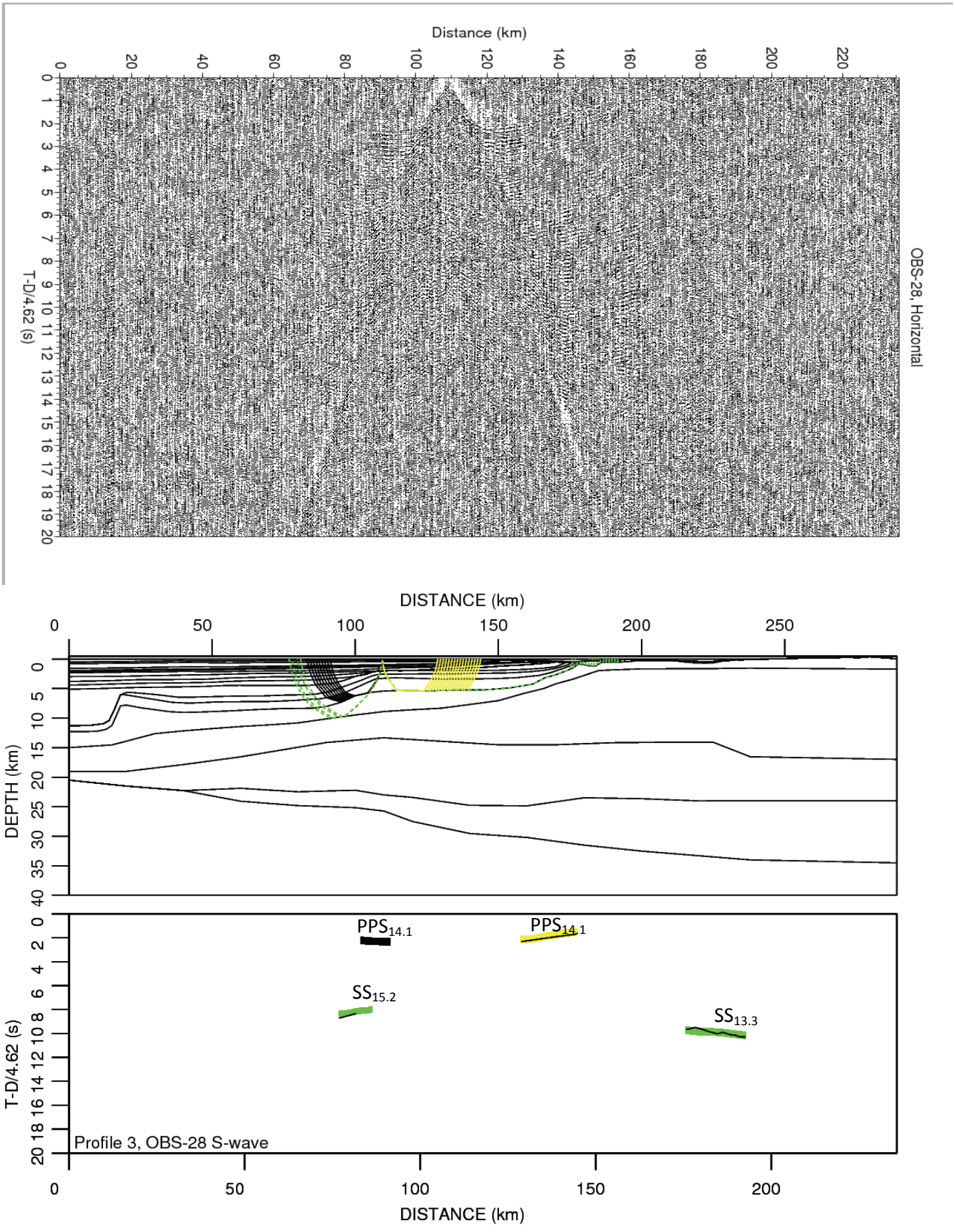

Horizontal component of OBS-28 with data plotted in SU and the rays, interpreted and calculated arrivals from Rayinvr.

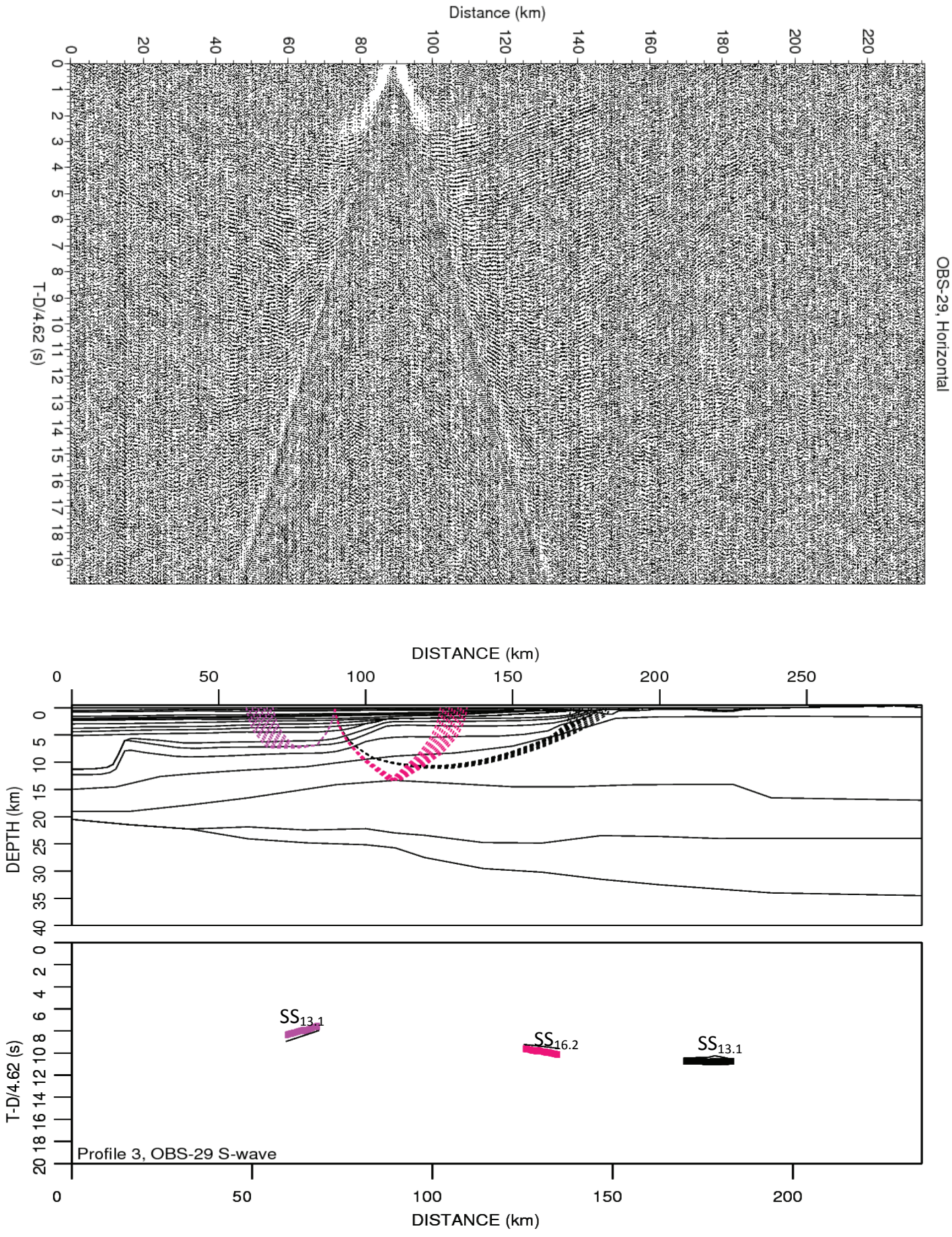

Horizontal component of OBS-29 with data plotted in SU and the rays, interpreted and calculated arrivals from Rayinvr.

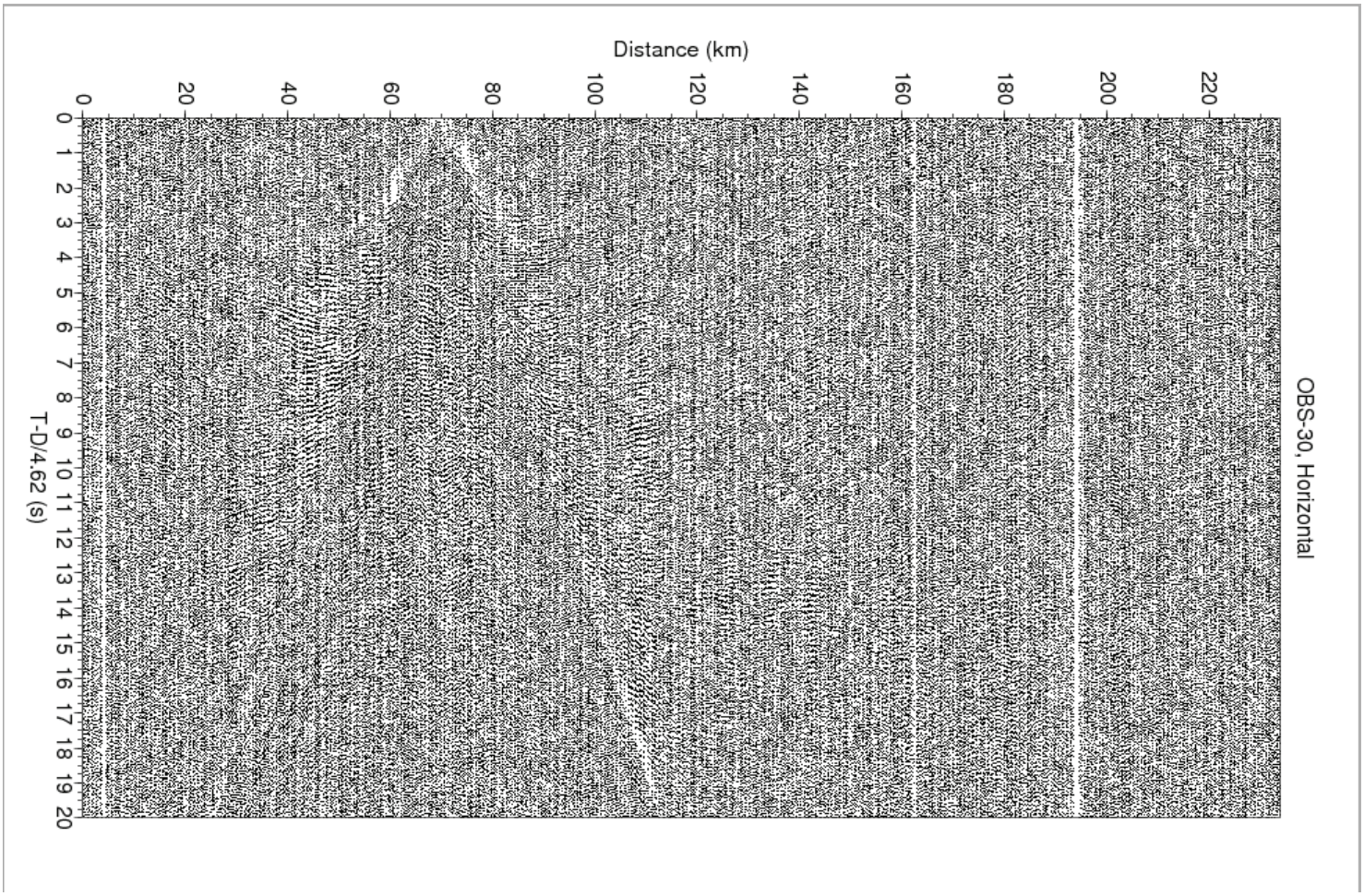

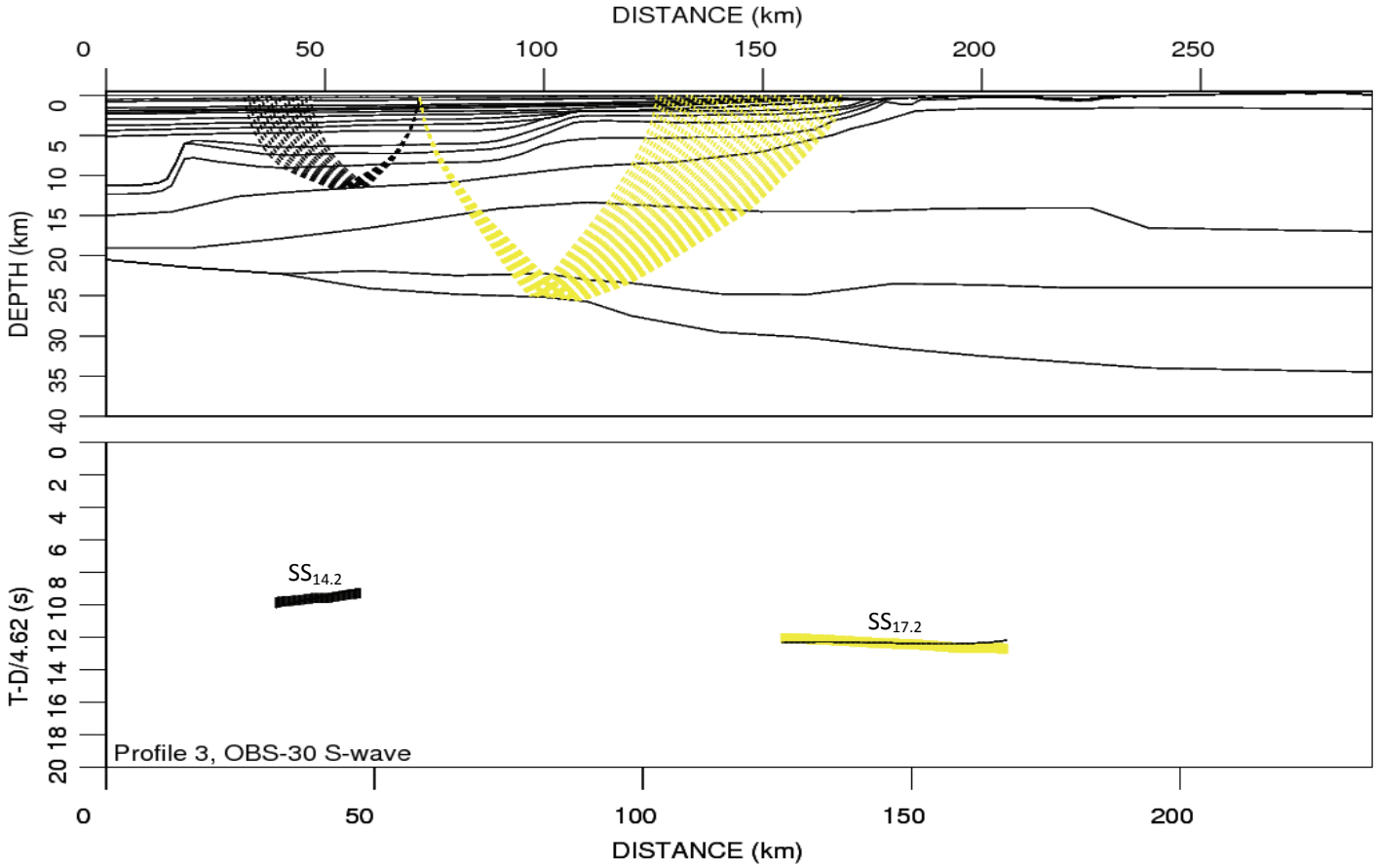

Horizontal component of OBS-30 with data plotted in SU and the rays, interpreted and calculated arrivals from Rayinvr.

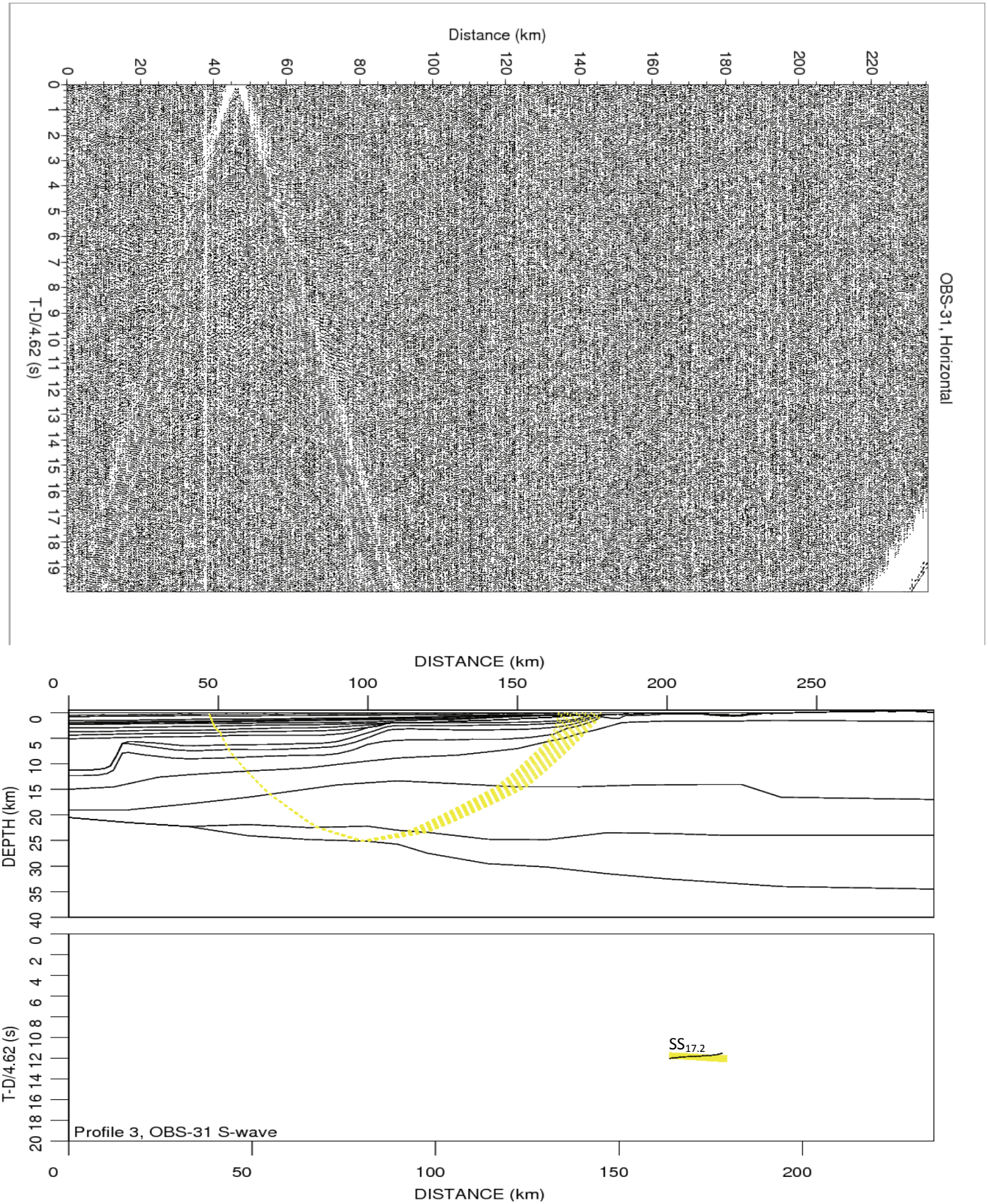

Horizontal component of OBS-31 with data plotted in SU and the rays, interpreted and calculated arrivals from Rayinvr.

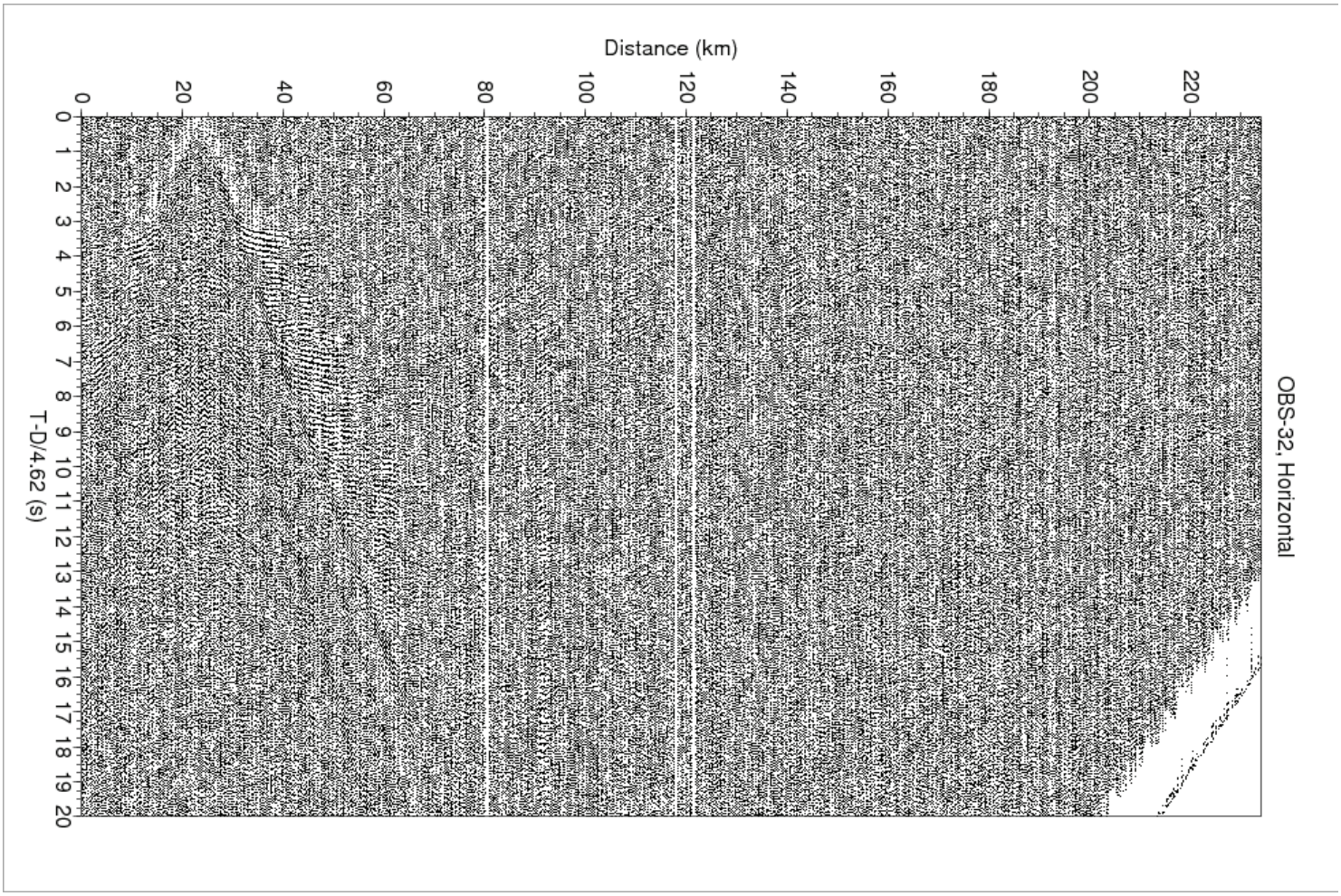

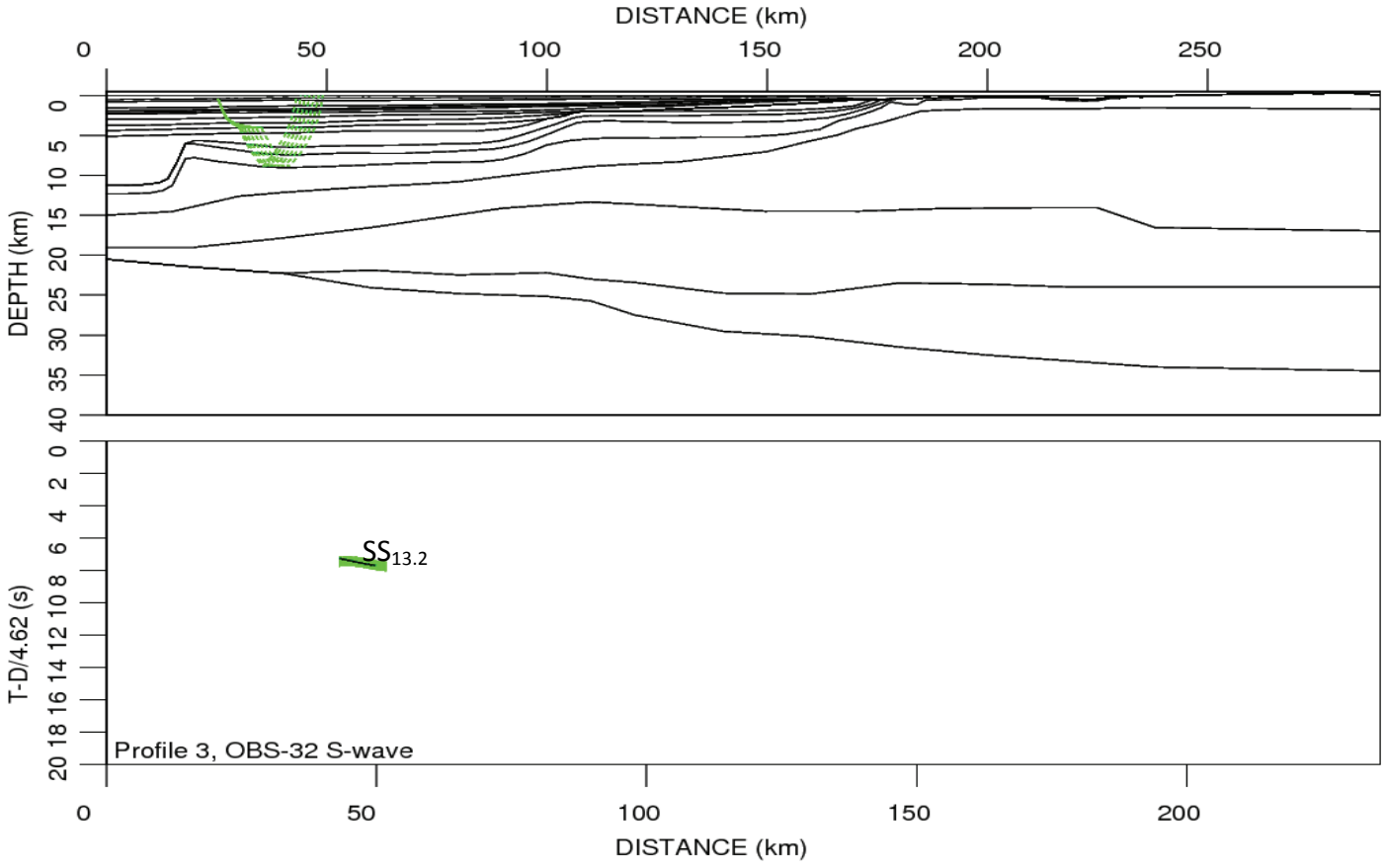

Horizontal component of OBS-32 with data plotted in SU and the rays, interpreted and calculated arrivals from Rayinvr.

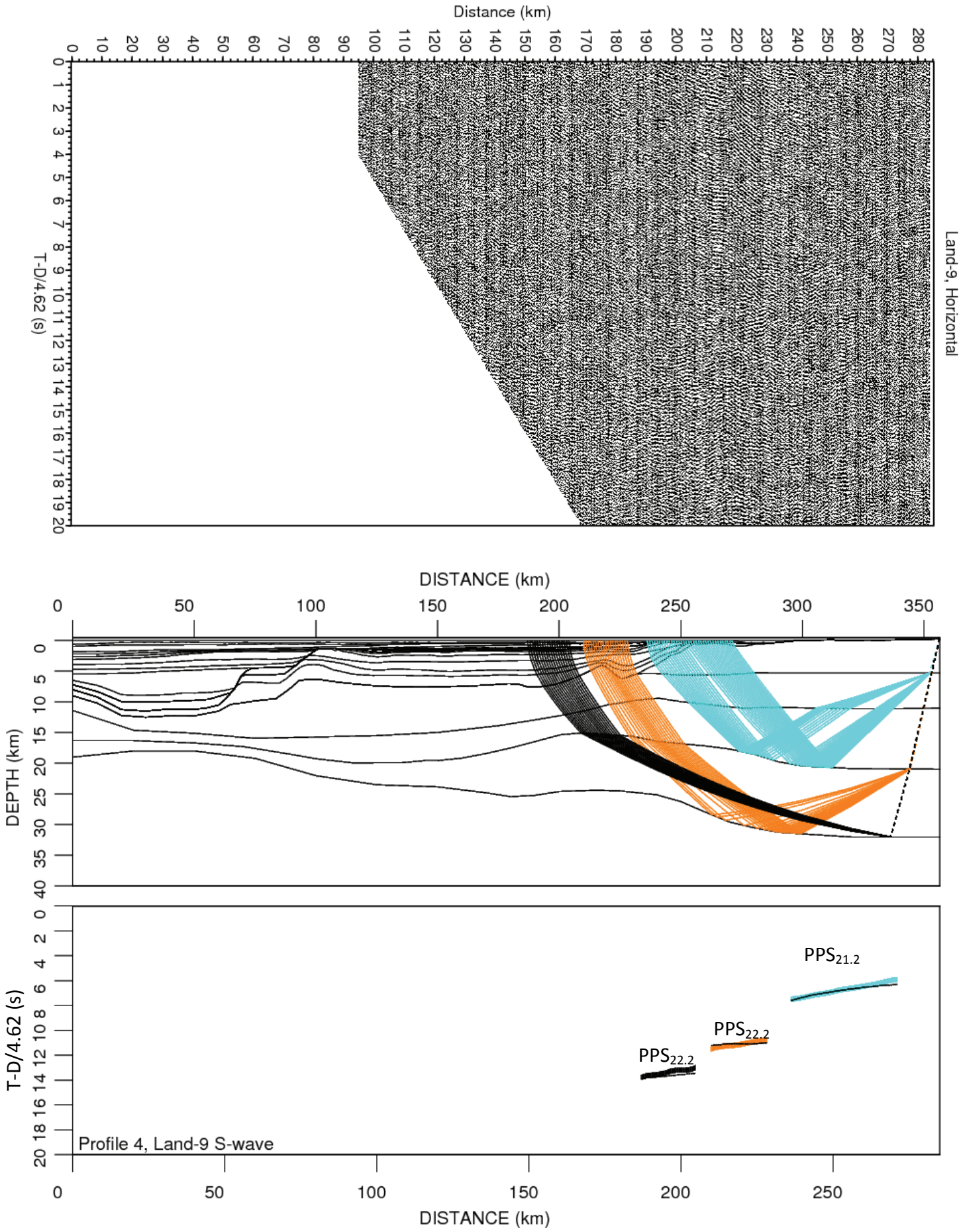

Horizontal component of Land-9 with data plotted in SU and the rays, interpreted and calculated arrivals from Rayinvr.

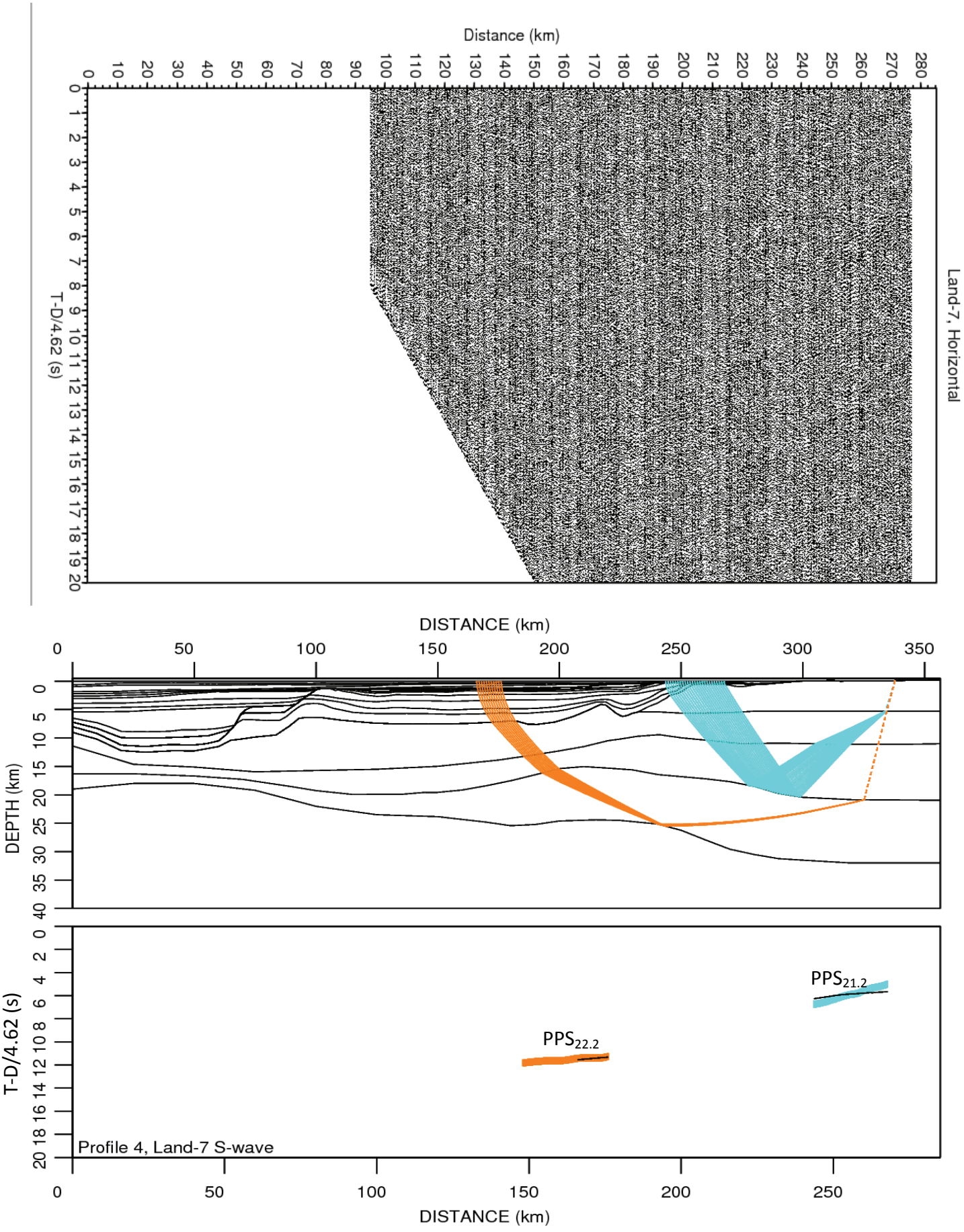

Horizontal component of Land-7 with data plotted in SU and the rays, interpreted and calculated arrivals from Rayinvr.

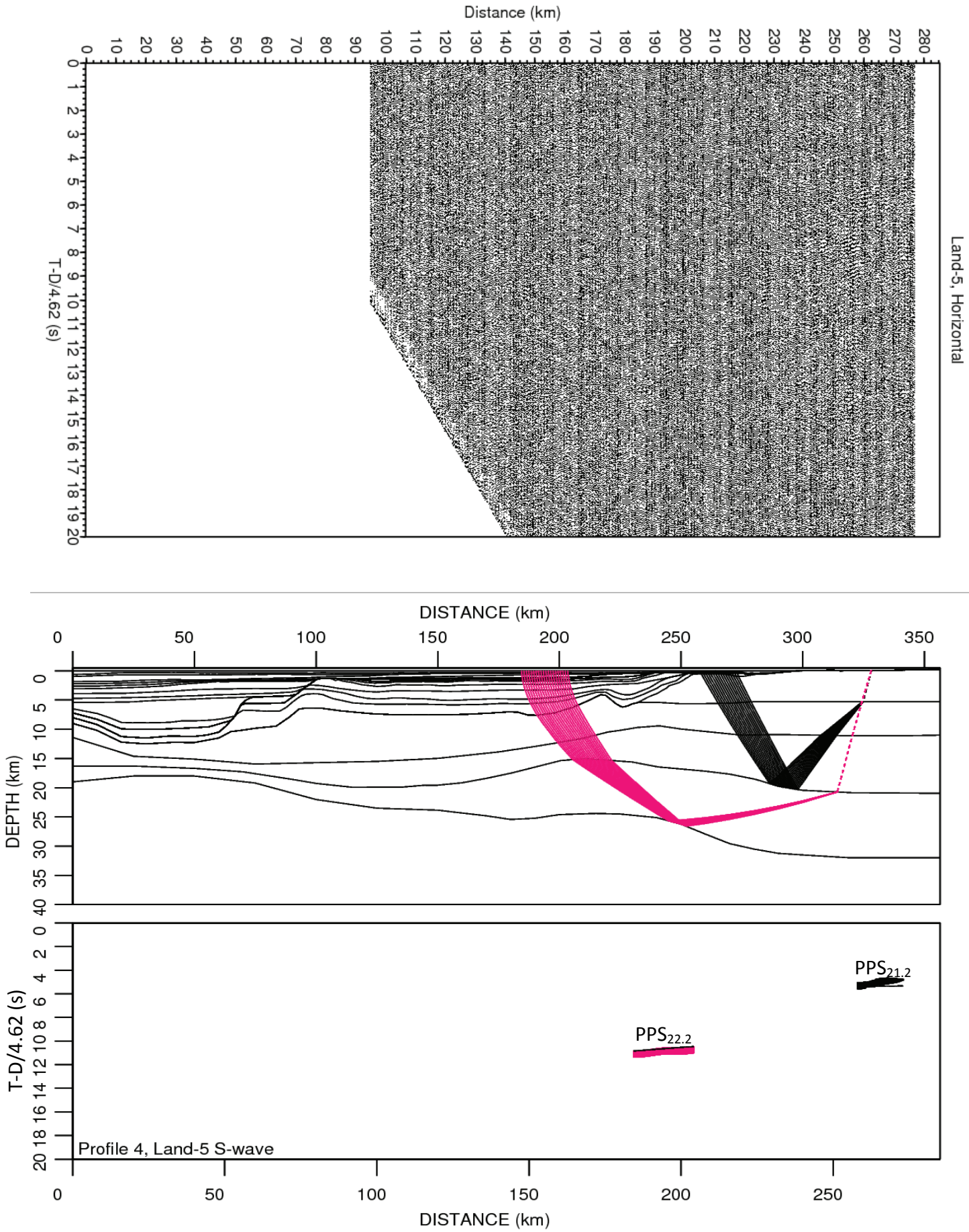

Horizontal component of Land-5 with data plotted in SU and the rays, interpreted and calculated arrivals from Rayinvr.

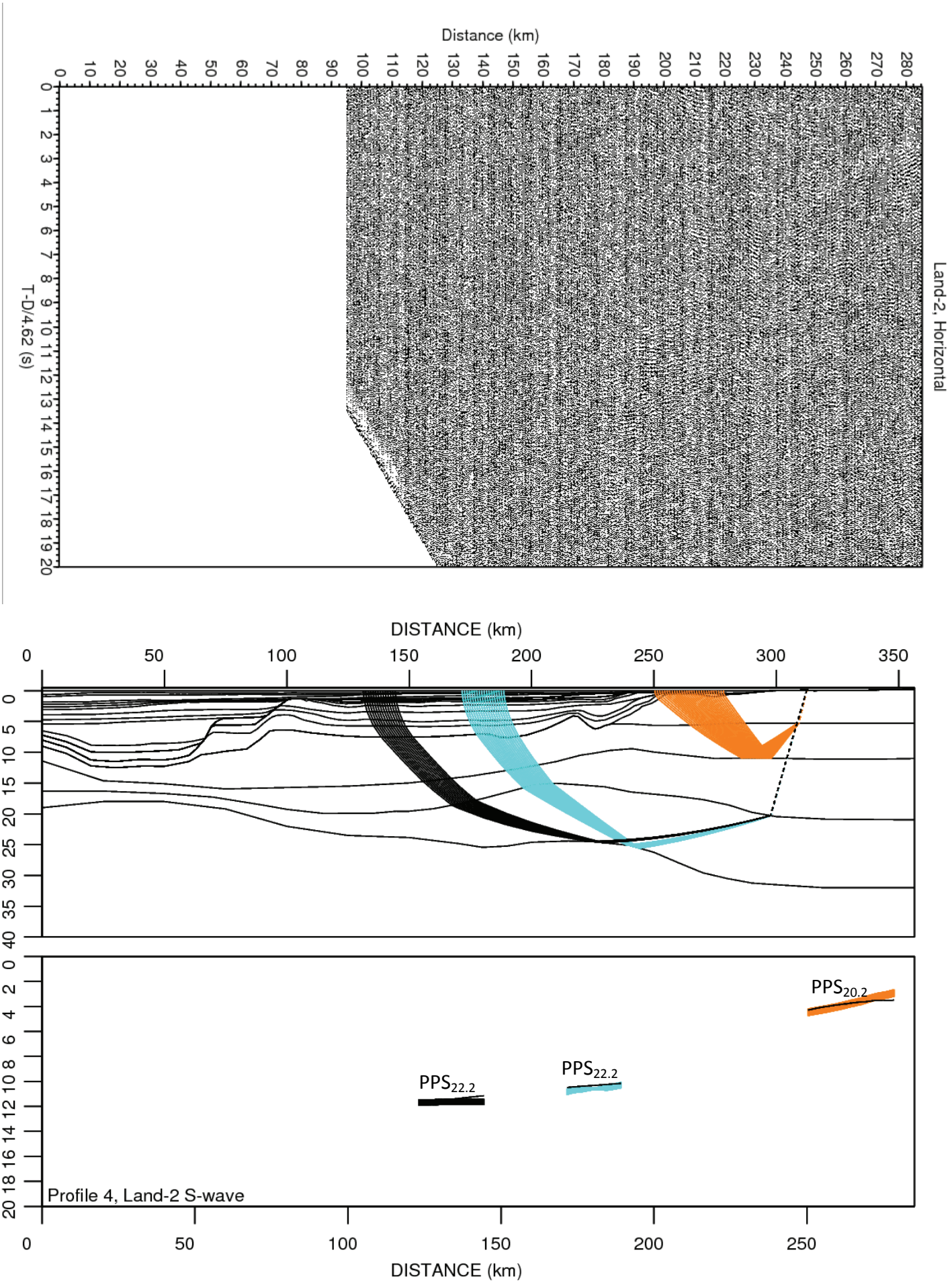

Horizontal component of Land-2 with data plotted in SU and the rays, interpreted and calculated arrivals from Rayinvr.

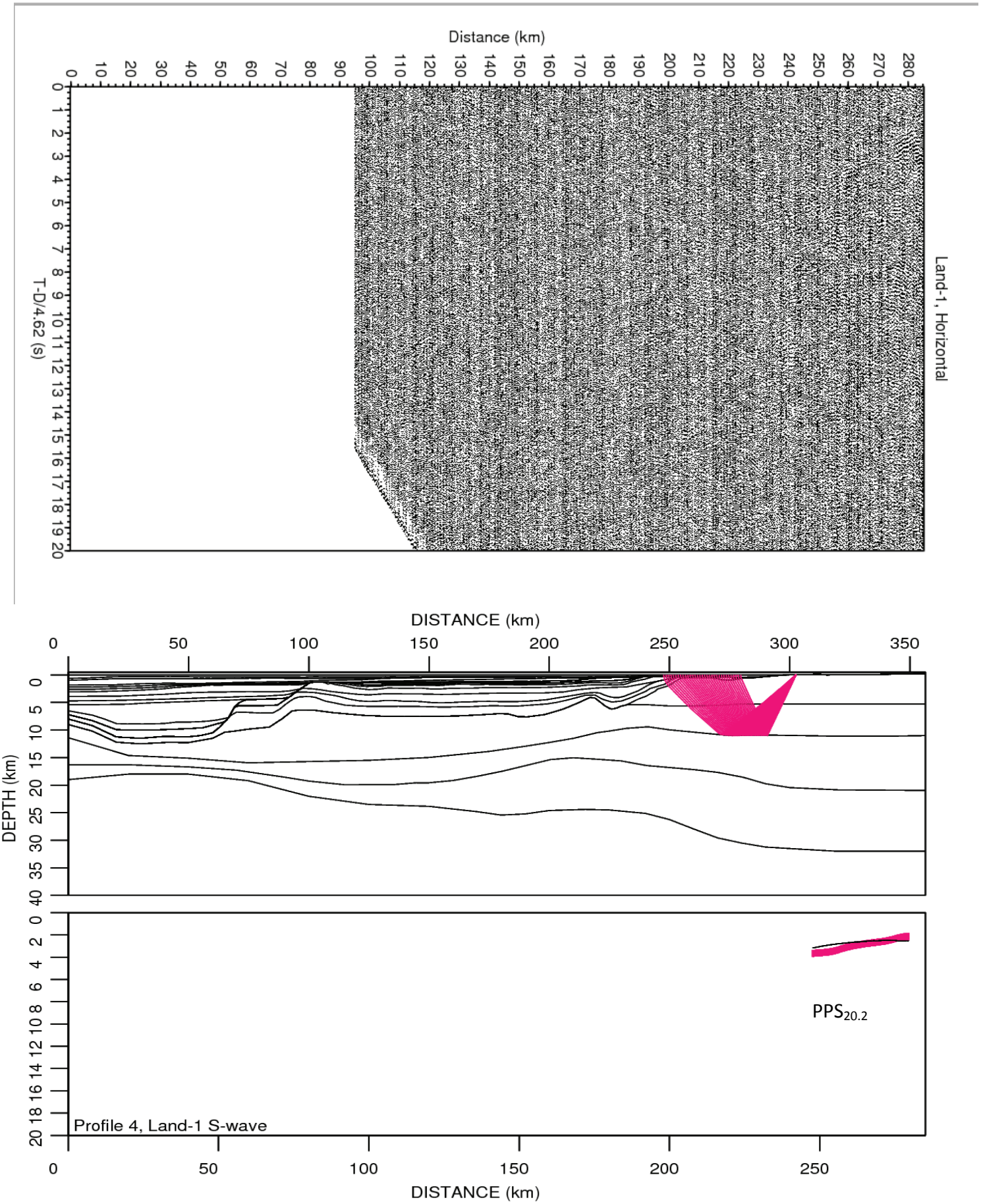

Horizontal component of Land-1 with data plotted in SU and the rays, interpreted and calculated arrivals from Rayinvr.

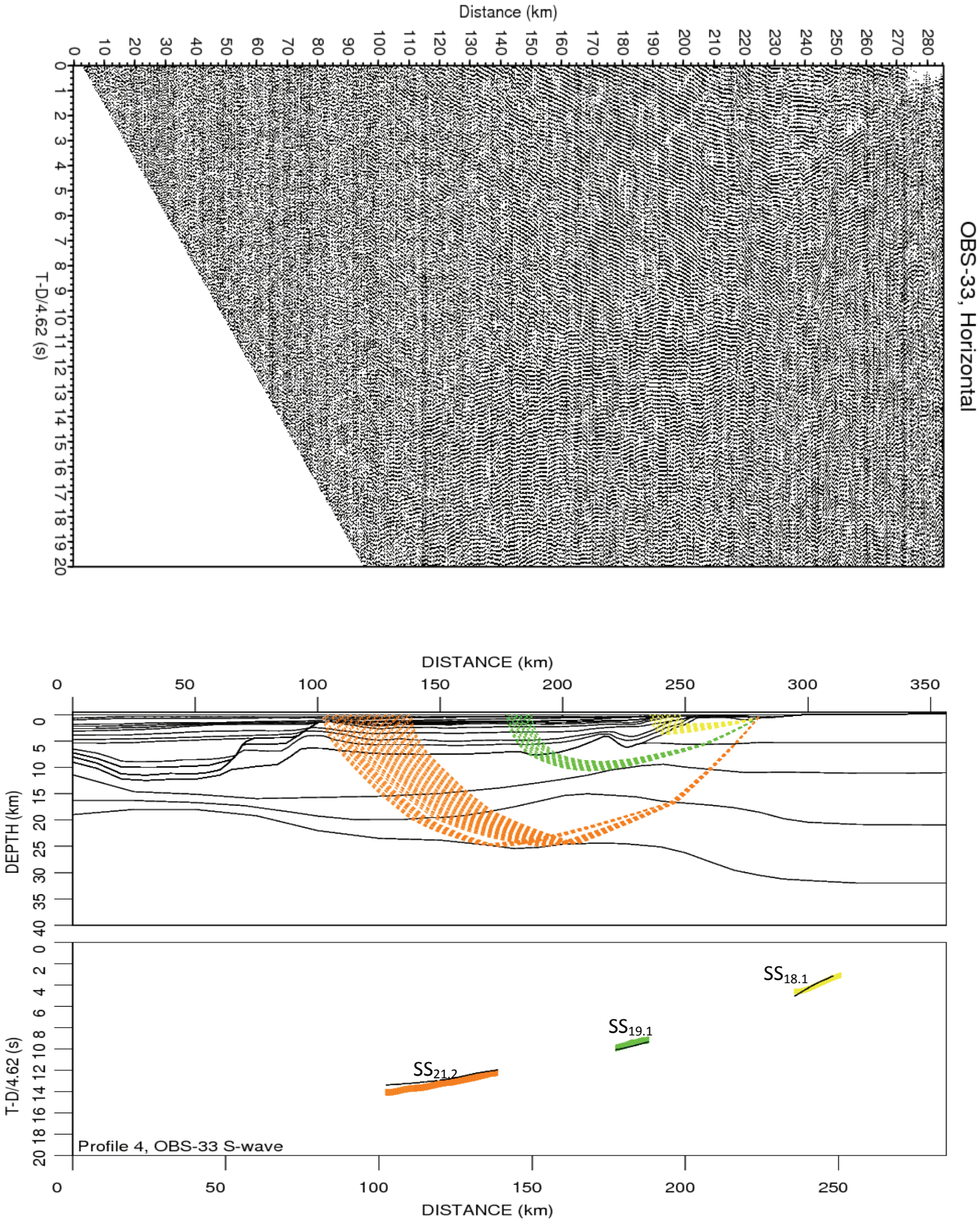

Horizontal component of OBS-33 with data plotted in SU and the rays, interpreted and calculated arrivals from Rayinvr.

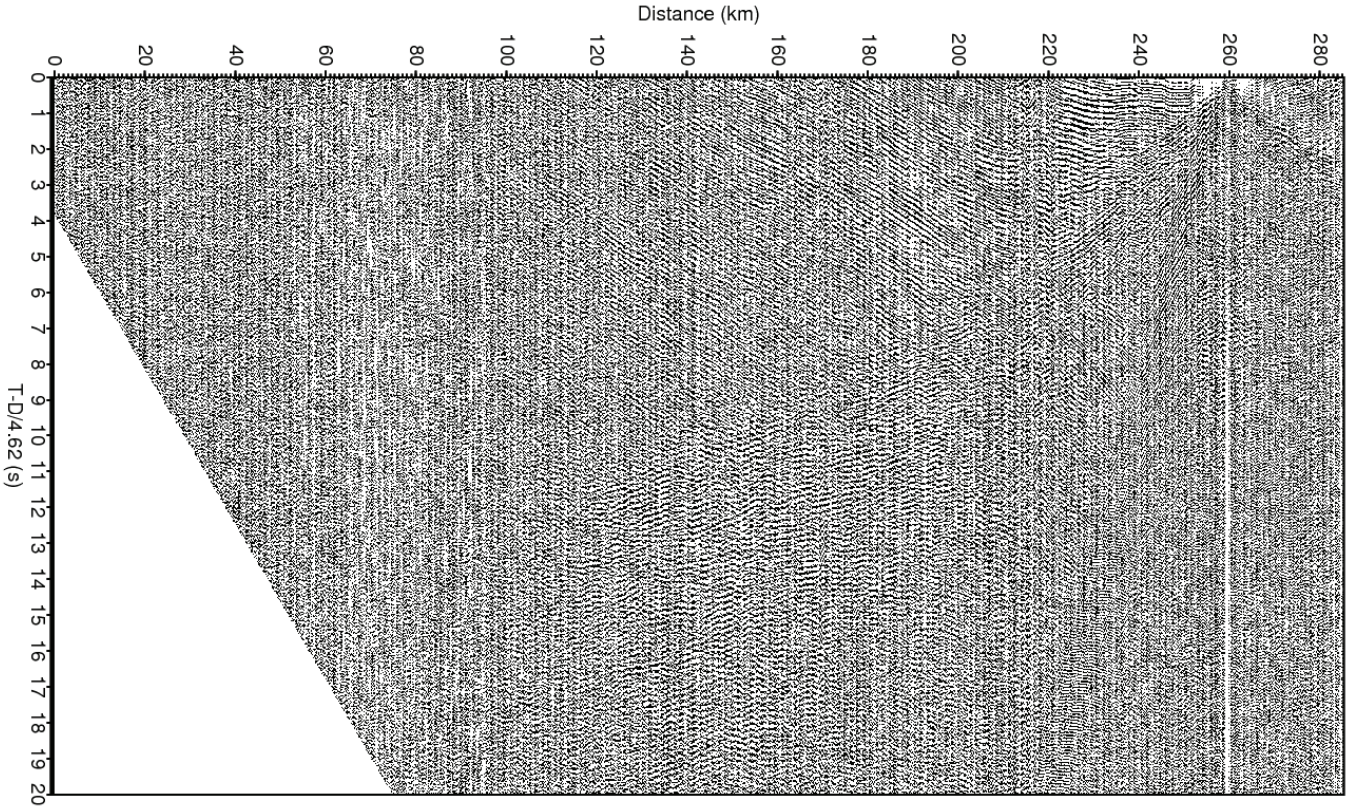

OBS-34, Horizontal

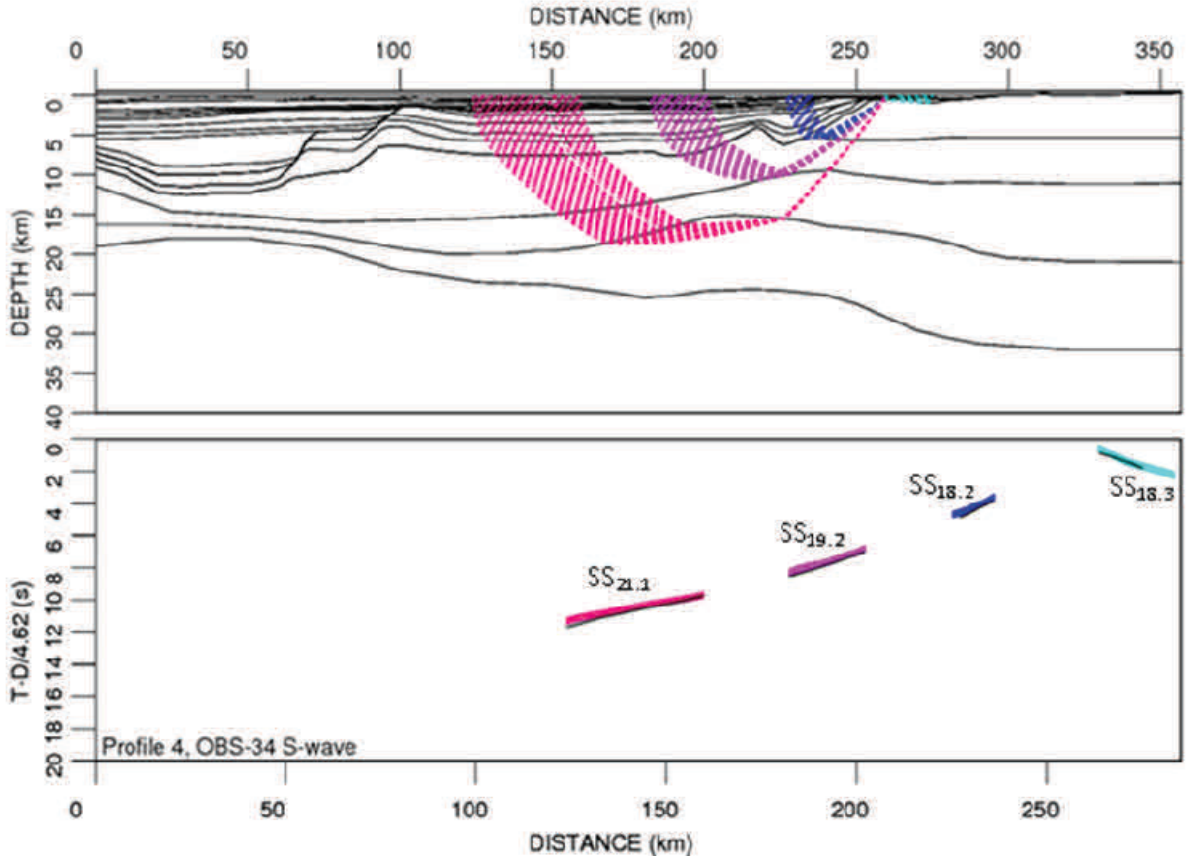

Horizontal component of OBS-34 with data plotted in SU and the rays, interpreted and calculated arrivals from Rayinvr.

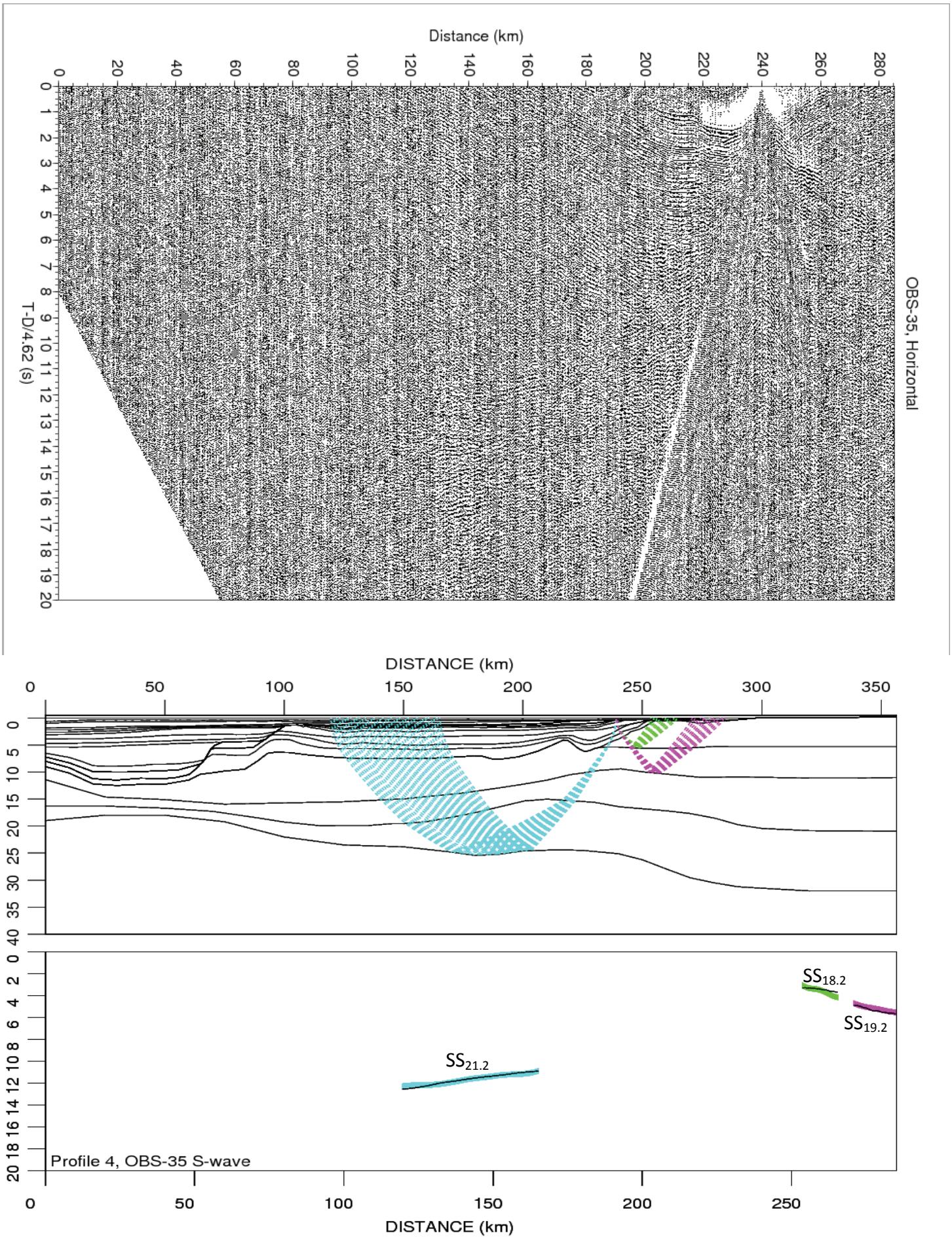

Horizontal component of OBS-35 with data plotted in SU and the rays, interpreted and calculated arrivals from Rayinvr.

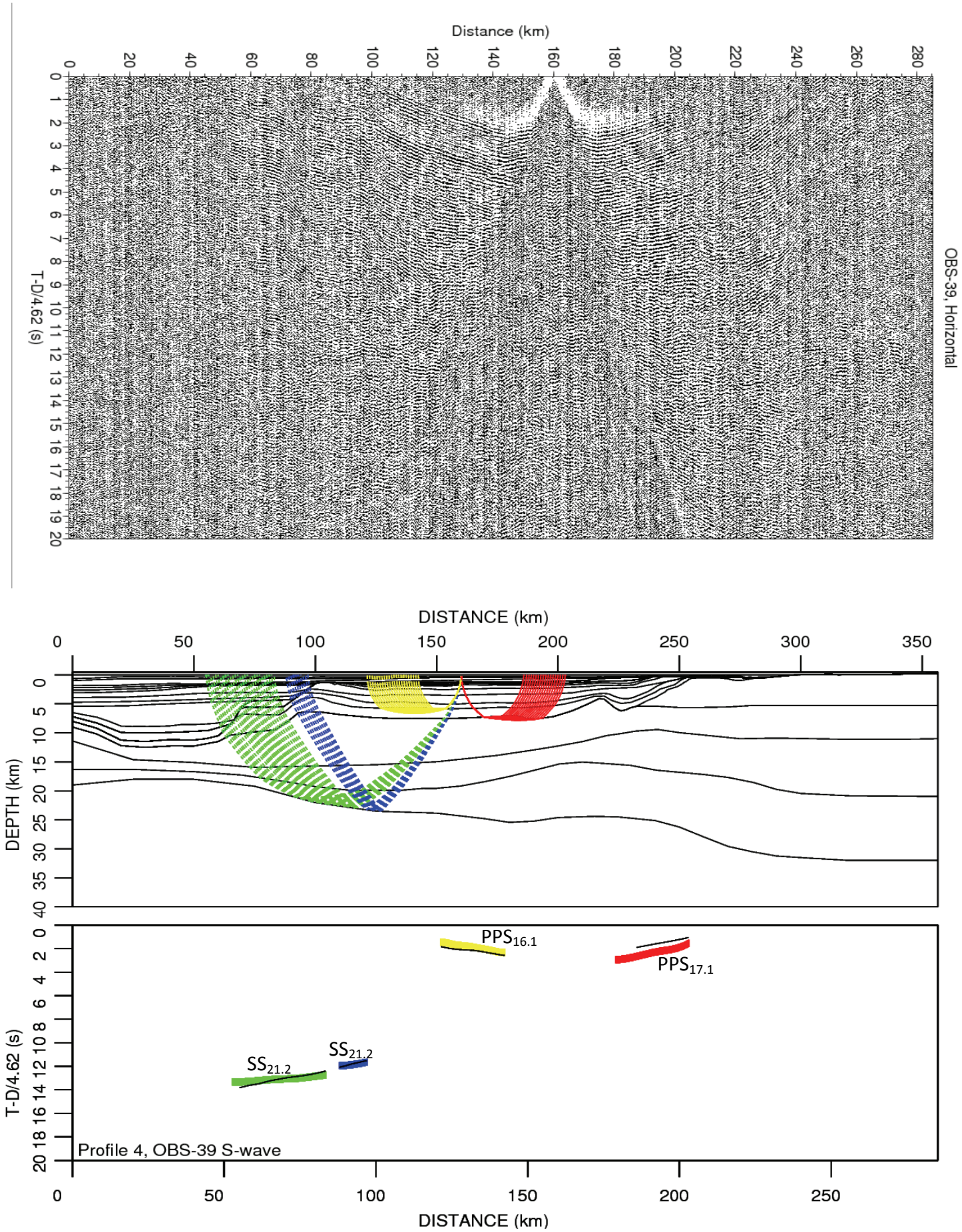

Horizontal component of OBS-39 with data plotted in SU and the rays, interpreted and calculated arrivals from Rayinvr.

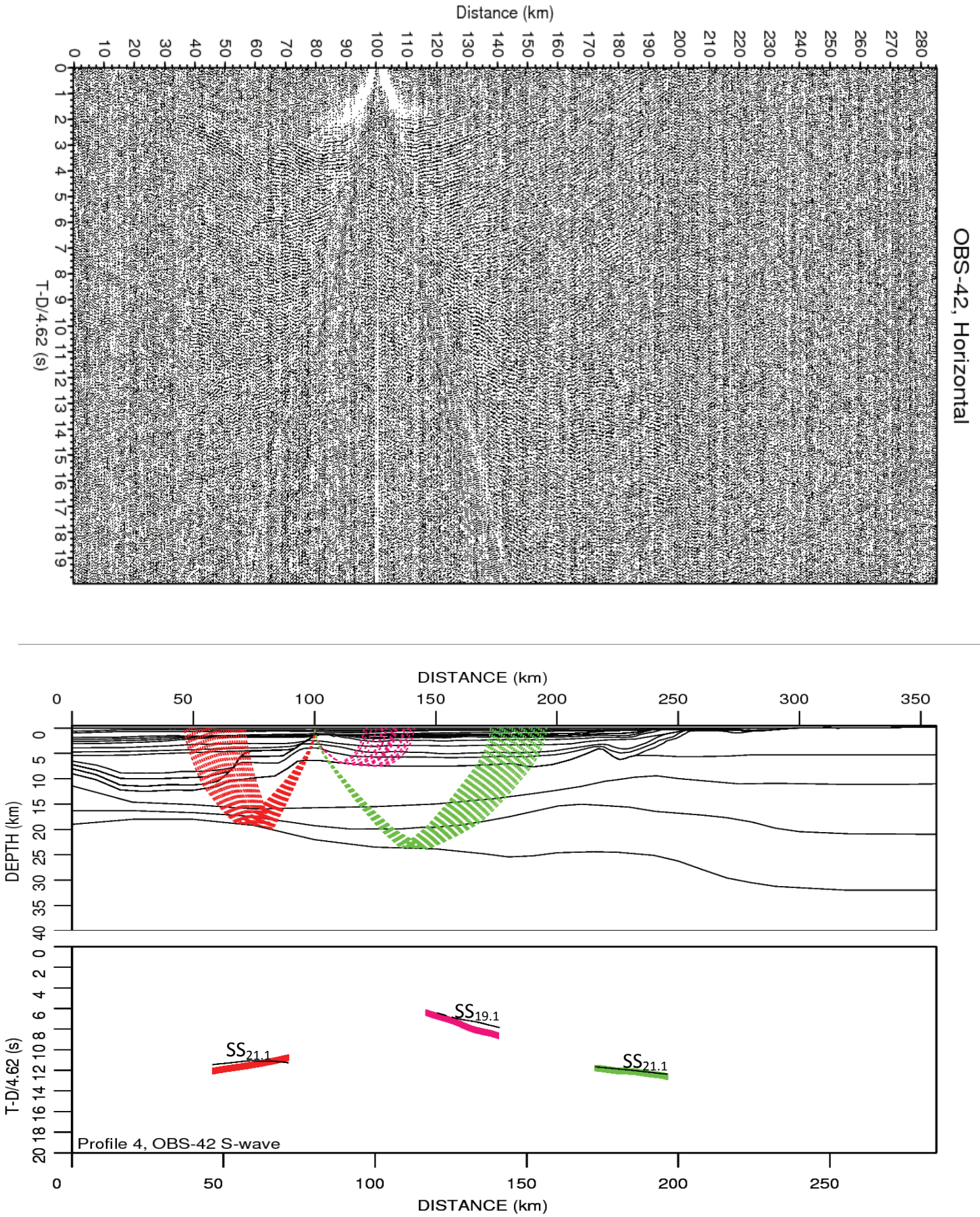

Horizontal component of OBS-42 with data plotted in SU and the rays, interpreted and calculated arrivals from Rayinvr.

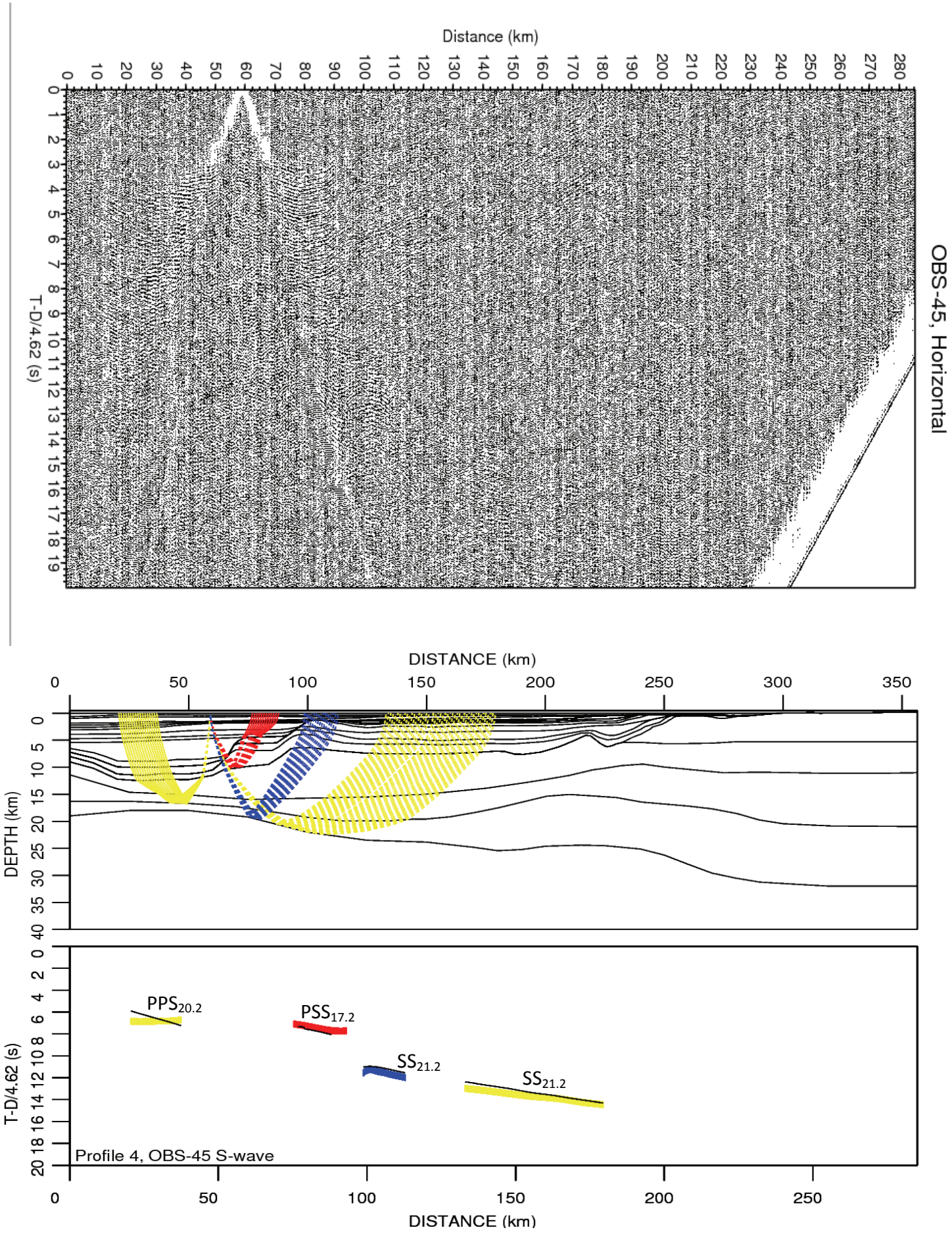

Horizontal component of OBS-45 with data plotted in SU and the rays, interpreted and calculated arrivals from Rayinvr.

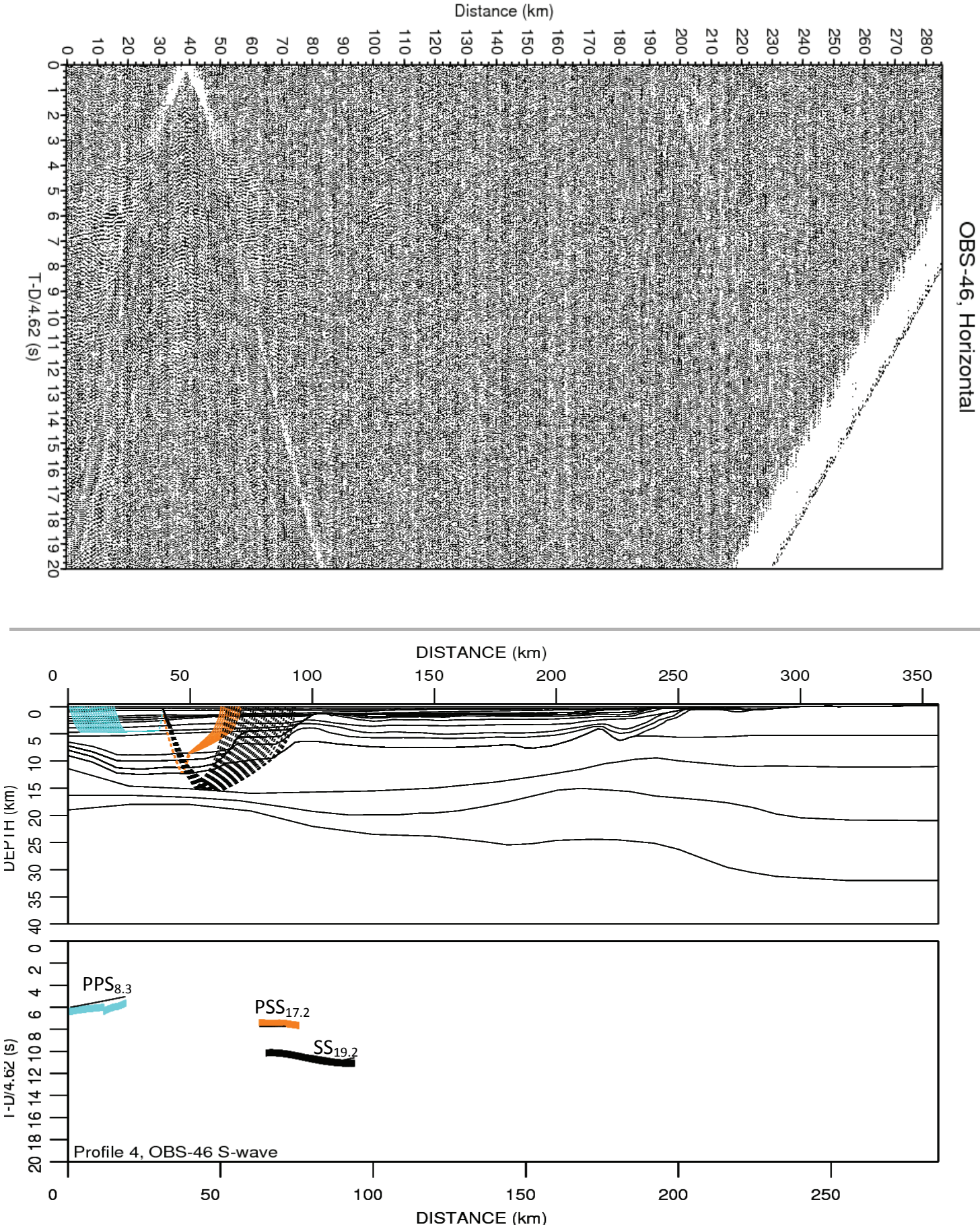

Horizontal component of OBS-46 with data plotted in SU and the rays, interpreted and calculated arrivals from Rayinvr.